Static and Dynamic Investigation of Magnonic Systems: Materials, Applications and Modeling

Von der Fakultät Mathematik und Physik der Universität Stuttgart
zur Erlangung der Würde eines Doktors der
Naturwissenschaften (Dr. rer. nat.) genehmigte Abhandlung

Vorgelegt von
Frank Martin Ernst Schulz
aus Stuttgart

Hauptberichterin:	Prof. Dr. Gisela Schütz
Mitberichter:	Prof. Dr. Peter Michler

Tag der mündlichen Prüfung: 03.04.2023

Max-Planck-Institut für Intelligente Systeme, Stuttgart
2023

Contents

List of Figures

List of Abbreviations

2D:	two dimensional
AC:	alternating current
AFM:	atomic force microscopy
ALD:	atomic layer deposition
APD:	avalanche photodiode
AWG:	arbitrary waveform generator
BLS:	Brillouin light scattering
BV:	backward volume
CMOS:	complementary metal oxide semiconductor
DC:	direct current
DE:	Damon-Eshbach
EELS:	electron energy loss spectroscopy
EDX:	energy-dispersive x-ray spectroscopy
FIB:	focused ion beam
FMR:	ferromagnetic resonance
FV:	forward volume
FZP:	Fresnel zone plate
GGG:	gadolinium gallium garnet
GIS:	gas injection system

hBN:	hexagonal boron nitride
HR-TEM:	high resolution transmission electron microscopy
IP:	in-plane
LLG:	Landau-Lifshitz-Gilbert
LPE:	liquid phase epitaxy
MBE:	molecular beam epitaxy
MOKE:	magneto-optical Kerr effect
NMP:	*N*-Methyl-2-pyrrolidone
OOP:	out-of-plane
OSA:	order-selecting aperture
PDMS:	polydimethylsiloxane
PSSW:	perpendicular standing spin wave
PVD:	physical vapor deposition
Py:	permalloy
RF:	radio frequency
SEM:	scanning electron microscopy
SI:	Système international d'unités
SQUID:	superconducting quantum interference device
TEM:	transmission electron microscopy
TEY:	total electron yield
TR-STXM:	time-resolved scanning transmission x-ray microscopy
UV:	ultra-violet
vdW:	van der Waals
VNA:	vector network analyzer
VSM:	vibrating sample magnetometer
XAS:	x-ray absorption spectroscopy
XMCD:	x-ray magnetic circular dichroism
YIG:	yttrium iron garnet

Abstract

The interaction of magnetic moments in solids can lead to complex dynamic behaviors that have inspired a wide range of scientific endeavors in both fundamental research and for potential applications. The study of magnetization dynamics is at the heart of the relatively young research field of magnonics, which seeks to utilize magnons, bosonic quasiparticles associated with the collective precession of magnetic moments, for applications such as novel computing concepts or high-frequency applications. Magnons can appear in the form of coherent spin waves, which could be used for wave-based, analog, and neuromorphic computing concepts. The lack of charge transport in spin waves could in principle allow for devices that are free of losses due to Joule heating. However, the high energy impact associated with the generation of spin waves is currently a major obstacle. One of the characteristic properties of spin waves is their submicron wavelengths and frequencies in the giga- and terahertz range, which could enable applications with much higher clock frequencies compared to conventional semiconductor technology.

Successful implementation of magnonic concepts requires materials with suitable magnetic properties, especially low Gilbert damping. This is necessary to enable the propagation of spin waves on length scales from

micro to millimeters, corresponding to the relevant device sizes. The most commonly used materials in this context are the metals NiFe, CoFeB, and the insulator yttrium iron garnet (YIG). In addition, two-dimensional (2D) magnetic van der Waals (vdW) materials have recently attracted much attention in magnetism research. This class of materials offers the unique opportunity to study magnetic phenomena in reduced dimensionality, with the prospect of potential applications in so-called vdW heterostructures. A better understanding regarding the propagation of spin waves in these materials could pave the way for their application in magnonic devices.

The dynamic study of magnonic systems generally relies on sophisticated measurement techniques to determine their magnetic properties and magnetization dynamics, such as magneto-optical Kerr microscopy (MOKE) and Brillouin light scattering (BLS). The most powerful method is time-resolved scanning transmission X-ray microscopy (TR-STXM), which offers a unique combination of high spatial and temporal resolution of up to 20 nm and less than 50 ps, as well as large element-specific magnetic contrast. Although experiments can only be performed at synchrotron sources with x-ray transparent thin films, this method has been applied with great success to make direct measurements of magnetization dynamics, allowing imaging of spin waves in both space and time.

This thesis consists of three parts covering different aspects of magnonic research: Materials, applications, and more fundamental physical principles.

First, the influence of high temperatures on $Ni_{80}Fe_{20}$, a common material system used throughout magnonic research, is investigated. Transmission electron microscopy (TEM) combined with energy dispersive X-ray spectroscopy (EDX) and ferromagnetic resonance (FMR) measurements are employed to study the effects of vacuum annealing at different temperatures on 36 nm thick $Ni_{80}Fe_{20}$ films grown on Si. This is particularly important

for applications with spin-polarized currents, where high current densities are often applied and the material is thus exposed to high temperatures. Structural analysis and magnetometry were used to establish a link between the change in magnetic properties, mainly Gilbert damping and saturation magnetization, and the formation of nickel silicides at $Ni_{80}Fe_{20}$/Si interface. Depending on the annealing temperature, this resulted in a reduced $Ni_{80}Fe_{20}$ layer thickness with altered composition, even well below the eutectic temperature of the system. This seemingly negative effect could however in principle be used to locally change the magnetic properties of a device in order to create magnetization landscapes in a controlled manner.

The second part deals with the practical implementation of magnonic concepts and presents the experimental realization of a magnonic analog adder that uses the amplitude of interfering spin waves for addition operations. Using TR-STXM, the functionality of analog adder devices based on $Ni_{80}Fe_{20}$ and YIG is demonstrated by direct observation of spin-wave interference with precise control of the relative phase between the interacting spin waves. The adders were studied in terms of phase and amplitude variation, and the results were compared with theoretical predictions, demonstrating their functionality in the linear regime. Simultaneous excitation of spin waves at different frequencies and subsequent decomposition of the spin-wave signal into its frequency components also demonstrates magnonic multiplexing.

Finally, the direct observation of propagating spin waves and the study of their properties in the 2D vdW material Fe_5GeTe_2 are presented. Coherent spin waves in a wide frequency range from 2.5 GHz to 4 GHz were excited at different external fields and observed with TR-STXM, where the spin-wave attenuation was found to be still too high for applications. By evaluating the spin-wave wavelength as a function of frequency, the dispersion relation of the system could be determined and compared to

a theoretical model based on a dynamic matrix approach. The employed multilayer model provided insight into the dynamics of the system as a function of both the saturation magnetization and the interlayer coupling strength, and highlighted the differences with respect to conventional three dimensional materials.

While the results presented here focus on the fundamental properties and physical principles of magnonic devices, they also highlight some of the challenges that magnonic research faces and that need to be addressed before these fundamental principles can be applied to real-world technological applications.

Kurzzusammenfassung

Die Wechselwirkung magnetischer Momente in Festkörpern kann zu komplexen dynamischen Verhaltensweisen führen, die sowohl verschiedenste wissenschaftliche Arbeiten in der Grundlagenforschung als auch technologische Anwendungen inspiriert haben. Die Untersuchung der Magnetisierungsdynamik steht im Mittelpunkt des relativ jungen Forschungsgebiets der Magnonik. Diese befasst sich mit der Erforschung und technologischen Nutzung von Magnonen, bosonischen Quasiteilchen, die mit der kollektiven Präzession magnetischer Momente verknüpft sind. Diese eignen sich potentiell für Anwendungen in der Hochfrequenztechnik und in neuartigen Computerkonzepten. Magnonen können in Form von kohärenten Spinwellen auftreten, die für wellenbasierte, analoge, sowie für neuromorphische Rechnenkonzepte genutzt werden könnten. Spinwellen sind nicht zwangsläufig mit dem Transport von Ladungen verbunden, und könnten im Prinzip Bauelemente, die frei von Verlusten durch Joulesche Wärme sind, ermöglichen. Aktuell stellen jedoch hohe Verluste bei der Erzeugung von Spinwellen eine große Hürde dar. Eine der charakteristischen Eigenschaften von Spinwellen ist ihre Wellenlänge im Submikrometerbereich, mit Frequenzen im Giga- und Terahertzbereich, was Anwendungen mit stark erhöhten Taktfrequenzen im Vergleich zur herkömmlichen Halbleitertechnologie ermöglichen könnte.

Für die erfolgreiche Umsetzung magnonischer Konzepte sind Materialien mit geeigneten magnetischen Eigenschaften erforderlich, allen voran einer geringen Gilbert-Dämpfung. Dies ist erforderlich, um die Ausbreitung von Spinwellen auf Längenskalen von Mikro- bis Millimetern zu ermöglichen, die den relevanten Größenordnungen der Bauteile entsprechen. Die gängigsten Materialien sind dabei die Metalle NiFe, CoFeB und der Isolator Yttrium-Eisen-Granat (YIG). Zusätzlich haben zweidimensionale (2D) magnetische van der Waals (vdW)-Materialien in letzter Zeit viel Aufmerksamkeit in der Magnetismusforschung auf sich gezogen. Diese Klasse von Materialien bietet die einzigartige Möglichkeit magnetische Phänomene in reduzierter Dimensionalität zu untersuchen, mit der Aussicht auf potentielle Anwendungen in sogenannten vdW-Heterostrukturen. Ein besseres Verständnis bezüglich der Ausbreitung von Spinwellen in diesen Materialien könnte den Weg für ihre Anwendung in magnonischen Bauteilen ebnen.

Die dynamische Untersuchung magnonischer Systeme stützt sich im Allgemeinen auf hochentwickelte Messmethoden zur Bestimmung magnetischer Eigenschaften und Magnetisierungsdynamik, wie zum Beispiel magnetooptische Kerr Mikroskopie (MOKE) und Brillouin-Lichtstreuung (BLS). Die leistungsfähigste Methode ist die zeitaufgelöste Raster-Transmissions-Röntgenmikroskopie (engl. *time-resolved scanning transmission x-ray microscopy*, TR-STXM), die eine einzigartige Kombination aus hoher räumlicher und zeitlicher Auflösung von bis zu 20 nm und weniger als 50 ps bietet. Obwohl Experimente nur an Synchrotronquellen mit röntgentransparenten Dünnschichten durchgeführt werden können, wird diese Methode äußerst erfolgreich genutzt um direkte Messungen der Magnetisierungsdynamik durchzuführen und damit die räumliche und zeitliche Abbildung von Spinwellen zu ermöglichen.

Diese Dissertationsschrift ist in drei Teile gegliedert, die sich mit verschiedenen Aspekten der Magnonik-Forschung befassen: Materialien, Anwendungen, und physikalische Grundlagen.

Zunächst wird der Einfluss hoher Temperaturen auf ein typisches in der Magnonik verwendetes Schichtsystem untersucht. Mithilfe von Transmissionselektronenmikroskopie (TEM) in Kombination mit energiedispersiver Röntgenspektroskopie (EDX) und ferromagnetischen Resonanzmessungen (FMR) werden die Auswirkungen des Vakuumglühens bei verschiedenen Temperaturen auf eine auf Si gewachsene $Ni_{80}Fe_{20}$-Dünnschicht untersucht. Dies ist insbesondere in der Spintronik bei Anwendungen mit spinpolarisierten Strömen von Bedeutung, da hier häufig hohe Stromdichten verwendet werden und die Materialien somit hohen Temperaturen ausgesetzt sind. Durch Strukturanalyse und Magnetometrie konnte ein Zusammenhang zwischen der Änderung der magnetischen Eigenschaften, vor allem Gilbert-Dämpfung und Sättigungsmagnetisierung, und der Bildung von Nickelsiliziden an der Grenzfläche zwischen $Ni_{80}Fe_{20}$ und Si hergestellt werden. In Abhängigkeit der Glühtemperatur führte dies zu einer verringerten $Ni_{80}Fe_{20}$-Schichtdicke mit veränderter Zusammensetzung, selbst bei Temperaturen weit unterhalb der eutektischen Temperatur des Systems. Dieser vermeintlich negative Effekt ließe sich jedoch prinzipiell nutzen, um die magnetischen Eigenschaften eines Bauelements lokal zu verändern und so Magnetisierungslandschaften kontrolliert zu erzeugen.

Der zweite Teil befasst sich mit der praktischen Umsetzung magnonischer Konzepte und stellt die experimentelle Realisierung eines magnonischen Analogaddierers vor, der die Amplitude interferierender Spinwellen für Additionsoperationen nutzt. Unter Verwendung von TR-STXM wird die Funktionalität von Analogaddierern auf Basis von $Ni_{80}Fe_{20}$ und YIG durch direkte Beobachtung der Interferenz von Spinwellen mit präziser Kontrolle der relativen Phase demonstriert. Die Addierer wurden in Hinblick auf Phasen- und Amplitudenvariation untersucht, und die Ergebnisse mit theo-

retischen Vorhersagen verglichen, wodurch ihre Funktionalität im linearen Bereich gezeigt werden konnte. Durch gleichzeitige Anregung von Spinwellen bei verschiedenen Frequenzen und der anschließenden Zerlegung des Spinwellensignals in seine Frequenzkomponenten wird zudem magnonisches Multiplexing demonstriert.

Abschließend werden erste Beobachtungen von sich ausbreitenden Spinwellen in dem 2D vdW Material Fe_5GeTe_2 vorgestellt. Dazu wurden kohärente Spinwellen in einem breiten Frequenzbereich von 2.5 GHz bis 4 GHz bei verschiedenen externen Feldern angeregt und mittels TR-STXM beobachtet, wobei eine für Anwendungen noch zu hohe Dämpfung festgestellt wurde. Durch die Auswertung der Spinwellen-Wellenlänge als Funktion der Frequenz konnte die Dispersionsrelation des Systems bestimmt werden und mit einem theoretischen Modell basierend auf einem Matrixansatz verglichen werden. Das verwendete Mehrschichtmodell ermöglichte Einblicke in die Dynamik des Systems sowohl in Abhängigkeit der Sättigungsmagnetisierung als auch der Kopplungsstärke zwischen den Schichten. Die Ergebnisse wurden auch in Hinblick auf potentielle Unterschiede zu konventionellen Materialien ausgewertet.

Während die hier gezeigten Ergebnisse sich auf die grundlegenden Eigenschaften und physikalischen Prinzipien magnonischer Bauteile konzentrieren, zeigen sie auch einige Herausforderungen auf, mit denen die Forschung im Bereich der Magnonik konfrontiert ist und die bewältigt werden müssen, bevor diese grundlegenden Prinzipien auf reale technologische Anwendungen angewendet werden können.

Part I

Introduction

Introduction

Even after several years of studying magnetism, the attractive and repulsive forces felt when bringing two permanent magnets into close proximity never cease to cause delight. The history of humans being fascinated by magnets dates back several thousand years, with the first written record by Thales of Miletus around 600 BC, who reported on the attraction of iron and lodestone[1]. In ancient China, this interaction was used to create the first compass, in which a small iron plate would align itself with the Earth's magnetic field[2]. The underlying physical mechanisms remained mysterious for a long time, and it was only with the advent of the scientific method that it became possible to understand the phenomenon at a fundamental level, with the first complete classical theory published by James Clerk Maxwell in 1865[3]. Today, magnetism is best understood within a quantum mechanical framework in terms of the interaction between magnetic moments arising from the spin and orbital momentum of elementary particles.

For most of human history, the technological applications involving magnets have been very limited, however, modern technology crucially depends on magnetic components and devices. An important part of this is the usage of electromagnets, where a magnetic field is induced by electric currents. This is used for example in electromotors, pumps, crane magnets,

electronic components, and many more, with the advantage of being able to switch the magnetic interaction on and off by means of controlling the electric current. Permanent magnets on the other hand cannot be easily turned on or off, however, they are indispensable components of electromotors, and can also be found in bearings, hard disk drives, and various other electronic components.

A relatively new area of research in magnetism, *spintronics*, is concerned with using the electrons spin degree of freedom, e.g. for information processing applications [4–7]. Spin-polarized currents, or even pure spin currents, can be used to manipulate and control the magnetization of a device at the microscopic level. The manifold underlying physical phenomena, such as the spin Hall effect, Rashba-Edelstein effect and the spin Seebeck effect, are also the subject of many scientific efforts in the field of spintronics.
Closely related to this is the field of *magnonics*, which studies spin waves as a potential information carrier in information processing applications [8–11]. In conventional complementary metal-oxide-semiconductor (CMOS) technology, electronic charges and currents represent the basic units used for information processing. The movement of electrons in a semiconductor is necessarily linked to heat production by means of Joule heating and other dissipation mechanisms. In contrast to this, magnonic devices seek to utilize propagating spin waves, where no charge transport is needed, since information is transmitted by magnons, the bosonic quasi-particles associated with the collective precession of magnetic moments in a material. The length and time scales involved in this approach are comparable to those in contemporary CMOS technologies, with spin-wave wavelengths in the micro- and nanometer range and frequencies in the giga- and terahertz regime.

Several devices based on the interaction of spin waves have been pro-

posed and experimentally realized, such as interferometry-based Boolean logic devices[12,13], majority gates[14], or magnon transistors[15]. In the context of radio frequency (RF) engineering, spin-wave based directional couplers[16], frequency filters[17,18] and phase shifters[11] have been studied. Another aspect of magnonic research is concerned with reproducing phenomena from other areas of physics in magnonic systems, such as Bose-Einstein condensates[19,20], space-time crystals[21], tunneling of spin-waves[22], and magnonic crystals[23–25]. Some researchers have also looked into spintronic or magnonic systems for neuromorphic computing[26–28], which tries to mimic the architecture of a human brain to perform certain computational tasks, such as pattern recognition[29]. While neuromorphic computing can in principle be realized using binary approaches based on CMOS technology[30], researchers have been looking into more specialized hardware in order to save resources and energy[31,32]. One of these avenues is analog computing, where the continuous nature of certain physical quantities is used to perform calculations. Early electronic devices, which were used for example to calculate ballistic trajectories, were exclusively based on this analog approach, and even after the introduction of Turing complete binary computers, they coexist until today. Recently, analog computing has seen a resurgence in the context of machine learning, with engineers and scientists looking for tailored hardware solutions with lower power consumption and higher speed[33].

The fabrication of this kind of magnon-based hardware requires sophisticated thin film deposition and lithography techniques. The methods used are largely similar to those used in the modern semiconductor industry. Both optical methods, as well as electron beam lithography can be used to pattern structures with feature sizes ranging from several mm down to the nm scale[34,35]. Thin film deposition techniques, such as thermal evaporation, molecular beam epitaxy, ion beam- or magnetron sputtering allow various materials to be deposited onto a substrate with precise control

of the film thickness and structure. The choice of thin film deposition and lithography technique depends on many factors, most importantly the substrate used, the material deposited, the fabrication quantity, the speed, and of course the structure size.

One particular type of material that has recently attracted much interest are two dimensional (2D) van der Waals (vdW) crystals, which consist of individual layers only bonded together by the weak vdW interaction. In such systems, it is possible to mechanically exfoliate individual layers to study physical phenomena down to the monolayer limit, and even stack different layers in so-called vdW heterostructures [36,37]. Graphene is by far the best studied 2D material at present and has given important insights into the physics of 2D systems [38,39]. With the discovery and synthesis of magnetic vdW materials, such as $Cr_2Ge_2Te_6$ [40] and $FePS_3$ [41,42], new opportunities for fundamental research and applications have opened up [43,44]. Most vdW magnets exhibit very low Curie temperatures, although some materials with ferromagnetic properties close to room temperature have been studied, such as Fe_5GeTe_2 [45].

To determine certain material parameters such as crystal structure or elemental composition, or in the case of magnetic thin films magnetic properties such as saturation magnetization and magnetic anisotropy, dedicated experimental techniques have been developed over time. The most common method for determining the crystal structure of a material is x-ray diffraction. Depending on the involved length scales and materials, either optical, x-ray or electron microscopy methods can be employed to investigate the morphology of a device on a microscopic scale. Elemental composition can be determined by means of spectroscopic methods, such as electron energy loss spectroscopy (EELS) or energy-dispersive x-ray (EDX) spectroscopy.

The study of macroscopic magnetic properties is sometimes referred to as magnetometry, with a wide range of different methods available.

A vibrating sample magnetometer (VSM) can be used to determine the magnetic moment and therefore the saturation magnetization of a sample, as well as anisotropies. Using temperature dependent measurements, it is even possible to obtain information about microscopic magnetic properties such as exchange stiffness, however, this requires an accurate model of the system at hand [46,47].

In ferromagnetic resonance (FMR) experiments, the resonant excitation of spin waves with wavevector $k = 0$ is used to determine a samples effective saturation magnetization, gyromagnetic ratio, anisotropies, as well as magnetic damping [48]. An optical method of magnetometry, which is also capable of detecting spin waves, exploits the magneto-optical Kerr effect (MOKE), where the polarization of light reflected by some magnetic material is changed depending on the local magnetization of the sample [49]. When a pulsed laser is used as a light source, it can be synchronized with the spin-wave excitation to allow for time-resolved measurement using a pump-probe detection scheme [50]. Brillouin light scattering (BLS) uses the direct interaction of light with magnons to determine relative amplitude, frequency, and k-vector of spin waves in a material. Using this method, it is therefore in principle possible to obtain information with both spatial and temporal resolution, however, to achieve a high spatial resolution, the k-vector sensitivity has to be sacrificed [51]. Both MOKE and BLS are wavelength-limited, and the signal cannot be easily converted to absolute magnetization.

The spatial resolution can be improved by using circularly polarized x-rays. The x-ray magnetic circular dichroism (XMCD) effect, which yields different absorption coefficients for circularly polarized x-rays depending on the relative orientation of photon angular momentum and local magnetization, can be exploited to obtain magnetic contrast [52]. With this method, it is possible to obtain quantitative information about the magnetic moments of individual elements in a spatially resolved manner [53]. Again, by employing a pump-probe scheme, it is possible to perform time-resolved

measurements, for example in time-resolved scanning transmission x-ray microscopy (TR-STXM) [54]. Overall, this method allows for extremely high magnetic contrast in the GHz regime with a spatial resolution below 20 nm.

This work represents a compilation of studies regarding the conceptualization and characterization of different magnetic systems for applications in magnonics.

The first part of this work is concerned with the effects of vacuum annealing on $Ni_{80}Fe_{20}$ thin films grown on Si substrates with regards to its structural and magnetic properties. It is found that prolonged exposure to high temperatures results in the formation of nickel silicides, which coincides with a strong increase of Gilbert damping and a reduction of the saturation magnetization. The observed effects have to be taken into account when designing spintronic devices, where Joule heating could potentially lead to deterioration and even complete breakdown of functionality.

In the second part, the experimental realization of a magnonic analog adder based on controlled spin-wave interference is treated. Two prototypes, one based on metallic $Ni_{80}Fe_{20}$ and the other on insulating yttrium iron garnet (YIG), are used to perform addition operations by interference of Damon-Eshbach type spin waves in the linear regime. By employing TR-STXM as a measurement technique, it was possible to directly observe the interference of spin waves at different conditions, from complete destructive to constructive interference. The multiplexing capabilities of the devices are demonstrated by excitation with multiple frequencies and subsequent decomposition of the resulting spin-wave signal into its frequency components.

The last part covers the experimental observation of propagating spin waves in a magnetic vdW material, where Damon-Eshbach and backward volume type spin waves were observed in Fe_5GeTe_2. The resulting dispersion relation was modeled using a multilayer approach based on a dynamic

matrix method[55], which yielded information on the material and gave insight into the peculiar shape of the dispersion relation.

Part II

Scientific Background

1 | Theoretical Background

In this chapter, the physical concepts that are most relevant for this work will be briefly introduced. Its content is inspired by different textbooks on the topic of solid state magnetism, to which the reader is referred for a more thorough treatment of the subjects [1,56–58]. Units will be given in terms of the *Système international d'unités* (SI).

1.1 Magnetostatics

The physical interactions within a magnetic material in thermal equilibrium can be described by Magnetostatics. In the following, the basic concepts and applications which are of relevance to this thesis will be discussed. First, a brief description of magnetic moments and their basic properties will be given. Next their different interactions and resulting physical effects will be introduced.

1.1.1 Magnetic Moments

Moving charges generate magnetic fields, which in turn can affect other moving charges[3]. This causes a current loop in an external magnetic field $\mathbf{B}$ to experience a torque

$$\boldsymbol{\tau} = \mathbf{m} \times \mathbf{B}, \tag{1.1}$$

where $\mathbf{m}$ denotes the current loops magnetic moment. This torque will try to align the magnetic moment with the external field, and it is zero when they are parallel. Another consequence of this is that in a homogeneous external field, a magnetic moment will not experience any force pushing it along the field lines. This can also be expressed in terms of magnetic potential energy[1]

$$E_{\text{pot}} = -\mathbf{m} \cdot \mathbf{B}. \tag{1.2}$$

The physical origin of a magnetic moment can be varying, either classically originating from moving charges in a current loop, as was used introducing the concept, or quantum mechanically from a particles spin and orbital angular momentum. In the context of solid state magnetism, the magnetic moments arise from the electron spin and orbital angular momenta of the constituent atoms in a solid[56]. Both of these contributions can be understood in terms of the electronic structure of the solid, either in terms of discrete states or electronic bands, depending on the specifics of the system at hand.

From the magnetic moment, which scales with the system size, one can calculate the magnetization $\mathbf{M} = \mathbf{m}/V$, so the magnetic moment per unit volume, given in A/m. Oftentimes it is more useful to provide the magnetization, especially in the case of saturation magnetization, since it is not dependent on sample size and can be considered a material parameter[56].

Equation (1.2) describes the case of a single magnetic moment, for many purposes it's more useful to change to a continuous description, in which

the energy of an extended body with magnetization $\mathbf{M}$ in an external magnetic field $\mathbf{H}_{\text{ext}}$ is given by [58]

$$E_{\text{Zeeman}} = -\mu_0 \int_V \mathbf{M} \cdot \mathbf{H}_{\text{ext}} \, \mathrm{d}V, \tag{1.3}$$

where $\mu_0 \approx 4\pi \times 10^{-7} \, \mathrm{kg\,m/(s^2\,A^2)}$ is the vacuum permeability, and the integral is calculated over the volume V of the body.
Many magnetometers, such as the superconducting quantum interference device (SQUID) magnetometer used for parts of this work, measure the magnetic moment of a sample.
The magnetic induction inside a material with magnetization $\mathbf{M}$ in an externally applied magnetic field $\mathbf{H}$ is given by [56]

$$\mathbf{B} = \mu_0 \left(\mathbf{H} + \mathbf{M} \right), \tag{1.4}$$

in units of T. This can also be written in terms of the magnetic susceptibility χ, using the relation $\mathbf{M} = \chi \mathbf{H}$, as

$$\mathbf{B} = \mu_0 \left(1 + \chi \right) \mathbf{H}. \tag{1.5}$$

The magnetic susceptibility gives a rough but straightforward way of characterizing the magnetic properties of a material, with purely diamagnetic materials possessing $\chi^{\text{dia}} < 0$, and para- and ferromagnetic materials $\chi^{\text{para,ferro}} > 0$. Whether a material is dia- para- or (anti-)ferromagnetic depends on the interaction between its constituent individual magnetic moments [56].

1.1.2 Magnetic Interactions and Anisotropy

In the following, different magnetic interactions will be introduced, together with the corresponding anisotropy terms. Magnetic anisotropy manifests

in a preferred magnetization direction in zero field. It can also become evident when the measurement of magnetic properties yields different results depending on the orientation of a sample with regards to an externally applied magnetic field. While there's different mechanisms that can cause anisotropic magnetic behavior, only the two most important ones will be discussed here, namely magnetocrystalline and shape anisotropy.

Dipolar Interaction

A magnetic dipole $\mathbf{m}_1$ is surrounded by a magnetic field $\mathbf{B}$, given by

$$\mathbf{B}(\mathbf{r}) = \frac{\mu_0}{4\pi} \frac{3\mathbf{r}(\mathbf{m}_1 \cdot \mathbf{r}) - \mathbf{m}_1 r^2}{r^5}, \tag{1.6}$$

where $\mathbf{r}$ is the position in space relative to the position of the magnetic moment. Using equation (1.2), the energy of another magnetic dipole $\mathbf{m}_2$ in this field can be written as [58]

$$E_{\text{dipole}} = -\mathbf{m}_2 \cdot \mathbf{B}(\mathbf{r}) = -\frac{\mu_0}{4\pi r^3} \left(\mathbf{m}_1 \mathbf{m}_1 - \frac{3}{r^2} (\mathbf{m}_1 \mathbf{r})(\mathbf{m}_2 \mathbf{r}) \right), \tag{1.7}$$

where $\mathbf{r}$ denotes the vector between $\mathbf{m}_1$ and $\mathbf{m}_2$ and $r = |\mathbf{r}|$ its magnitude. It can be seen that both the magnetic field and the energy scale with $1/r^3$, resulting in long-range interactions compared to e.g. exchange interaction, which will be discussed later on.

Depending on the relative orientation of the two magnetic dipoles and their relative position in space, this energy can either be positive or negative. In the case of two parallel magnetic moments of magnitude $m_1 = m_2 = 1\mu_\text{B}$, arranged in a chain ($\mathbf{r} \parallel \mathbf{m}$) at a distance of 1 Å, the energy corresponds to the thermal energy at a temperature of 1 K. This example illustrates that dipolar interaction cannot induce ferromagnetism with magnetic order at room temperature and above. This kind of interaction is, however, responsible for shape anisotropy, which will be discussed next, and also

plays an important role for spin waves when their wavelength is much larger than the materials exchange length[59].

Shape Anisotropy

The stray field in equation (1.6) that surrounds a magnetic dipole tends to demagnetize the sample and is associated with an energy

$$E_{\mathrm{S}} = \frac{1}{2} \int_V \mu_0 \mathbf{M} \cdot \mathbf{H}_{\mathrm{d}} \, \mathrm{d}V, \tag{1.8}$$

where $\mathbf{M}$ denotes the sample magnetization and $\mathbf{H}_{\mathrm{d}}$ its demagnetization field, integrating over the volume V of the sample[56]. For a non-spherical sample, this energy leads to the existence of favorable magnetization directions, and for an arbitrary shape it is only possible to approximate the shape anisotropy. However, for an ellipsoid with its semi-axes pointing along the x, y, and z direction, the demagnetization field can be written as[56]

$$\mathbf{H}_{\mathrm{d}} = -\mathcal{N}\mathbf{M}, \tag{1.9}$$

with the demagnetization tensor

$$\mathcal{N} = \begin{pmatrix} N_x & 0 & 0 \\ 0 & N_y & 0 \\ 0 & 0 & N_z \end{pmatrix}, \tag{1.10}$$

for which $N_x + N_y + N_z = 1$ holds[60]. This can be used in order to approximate the demagnetizing factors of a uniformly magnetized rectangular rod with an aspect ratio of $a : b : c$ according to

$$N_x = k/a; \quad N_y = k/b; \quad N_z = k/c, \tag{1.11}$$

with $k = (abc)/(ab + ac + bc)$ [61]. For certain special cases, simple approximations can be made, e.g. for thin films, where $N_x = N_y \approx 0$ and $N_z \approx 1$. In the absence of other sources for magnetic anisotropy, this leads to the magnetization lying in the thin film plane.

Exchange Interaction

The exchange interaction is a quantum phenomenon that has no classical analog and is a direct consequence of the Coulomb interaction and the fermionic nature of electrons. The quantum mechanical wave function of a many-body system consisting of identical particles obeys exchange symmetry. The spin-statistics theorem relates this to the particles' spin, namely half-integer spin fermions that are described by the Fermi-Dirac statistic, and integer spin bosons following the Bose-Einstein statistics. For fermions, such as electrons, the overall wave function has to been antisymmetric under exchange of particle labels. This is either achieved by an antisymmetric singlet spin state in the case of a symmetric spatial state, or a symmetric triplet state in the case of an antisymmetric spatial state. These two possible configurations are not degenerate and the energy difference is called the exchange energy. In ferromagnetic materials, this energy difference leads to parallel alignment of neighboring spins and hence to long-range magnetic order, which can be described using the Heisenberg model. In this model, the energy associated with the exchange interaction is described by the Hamiltonian [56]

$$\mathcal{H}_{\text{ex}} = -\sum_{ij} J_{ij} \mathbf{S}_i \cdot \mathbf{S}_j, \tag{1.12}$$

where J_{ij} denotes the exchange constant between the spins $\mathbf{S}_i$ and $\mathbf{S}_j$. For positive values of J, it describes ferromagnetic interaction, and for negative

J antiferromagnetic interaction. This model is mostly used in a way where J_{ij} is isotropic and only non-zero for the nearest neighbors. It can, however, be used to describe more general systems where exchange is anisotropic [62].

While the exchange constant J is given in terms of energy, there's many situations where instead the exchange stiffness A_{ex} is given, which also incorporates information about the crystal lattice. In a continuum approximation, it can be calculated as [56]

$$A_{\mathrm{ex}} = \frac{2JS^2z}{a}, \tag{1.13}$$

with the nearest neighbor distance a, the spin S, and the number of sites in the unit cell z. For a simple cubic lattice $z = 1$, for body-centered cubic $z = 2$, and for face-centered cubic $z = 4$. In real systems, A_{ex} is often empirically determined from neutron scattering or temperature dependent magnetometry measurements, and does not necessarily fulfill equation (1.13)
Typical values for A_{ex} lie in the range of 5 pJ/m to 100 pJ/m and can be determined by fitting micromagnetic models to magnetometric measurements [57].

Spin-orbit interaction

The relative movement of a charged nucleus and an electron in an atom results in a magnetic field which couples to the magnetic moment arising from the spin of the electron. This effect scales with the gradient of the nuclear potential and thus with the atomic number of the atom. For a single electron with orbital momentum $\mathbf{l}$ and spin $\mathbf{s}$, the Hamiltonian associated with the spin-orbit interaction reads [1]

$$\mathcal{H}_{\mathrm{so}} = \frac{-\mu_0 Ze^2}{8\pi m_{\mathrm{e}}^2 r^3}\mathbf{s}\cdot\mathbf{l}, \tag{1.14}$$

where Z denotes the atomic number, e the elemental charge, m_e the electron mass, and r the mean distance between electron and nucleus. Since the atomic radius r also scales with Z, the spin-orbit interaction overall scales with Z^4, making it relevant especially in heavy atoms.

While not necessarily a purely magnetic effect, spin-orbit interaction plays an important role in many magnetic phenomena, such as magnetocrystalline anisotropy, the splitting of atomic energy levels, as well as the spin Hall effect [63], some of which will be discussed in later sections in more detail. A typical value for the splitting of the $2p_{1/2}$ and $2p_{3/2}$ orbitals in Fe, Co, and Ni is on the order of $\Delta E \approx 15\,\mathrm{eV}$ [1].

Magnetocrystalline Anisotropy

A consequence of spin-orbit coupling is magnetocrystalline anisotropy. The interaction between spin and orbital momentum causes the electron spin to couple to the crystal field in a solid. Depending on the relative orientation of the crystallographic directions and an external field, this will result in magnetization curves with different features. Each crystal structure has specific directions along which it is easier or harder to magnetize, caused by the symmetry of the crystal lattice [56]. One important type of magnetocrystalline anisotropy only has a single axis of high symmetry, and is therefore called uniaxial. In this case, the anisotropy is characterized by a single parameter K_u, which can be either positive or negative. For $K_u < 0$, an easy axis exists, and for $K_u > 0$ the system will possess an easy plane perpendicular to the symmetry axis. In the case of a hexagonal lattice, this easy plane will be given by the basal plane of the crystal. Typical values [56] for K_u lie in the range of $10^2\,\mathrm{J/m^3}$ to $10^7\,\mathrm{J/m^3}$. While in principle well defined, it is more of an empirical parameter in real materials due their complicated structure with regards to inhomogeneities, impurities, defects, grain formation, or in general their polycrystalline nature.

Dzyaloshinskii–Moriya interaction

One consequence of spin-orbit coupling is the antisymmetric exchange, or Dzyaloshinskii–Moriya interaction (DMI), a magnetic interaction that favors non-collinear orientation of neighboring spins [56,64]. The corresponding energy contribution can be written as

$$\mathcal{H}_{\mathrm{DMI}} = \sum_{ij} \mathbf{D}_{ij}(\mathbf{S}_i \times \mathbf{S}_j), \tag{1.15}$$

with the sum over next neighbor spins $\mathbf{S}_i$ and $\mathbf{S}_j$, and a vector $\mathbf{D}_{ij}$ that quantifies the interaction strength and is defined to have its direction parallel to the cross product. DMI can be found in systems where inversion symmetry is broken, either at interfaces in multilayers [65], or in materials that have a crystal structure that is inversion asymmetric [66]. Depending on the magnitude and sign of $\mathbf{D}_{ij}$, this interaction can lead to the formation of chiral spin textures, such as magnetic skyrmions, and homochiral domain walls. Typically, for both bulk and interfacial DMI, the magnitude of D is on the order of a few $\mathrm{mJ/m^2}$.

1.1.3 Stoner-model of ferromagnetism

To explain the ferromagnetic properties of $3d$ transition metals, such as Fe, Ni, and Co, a description that includes the electronic band structure is needed. When many atoms interact in a periodic crystal, the overlap of the electron wave function will transform the discrete atomic states into continuous bands [1,56]. In the case of $3d$ transition metals, the $3d$ electrons will become delocalized and their wave function will spread over the crystal,

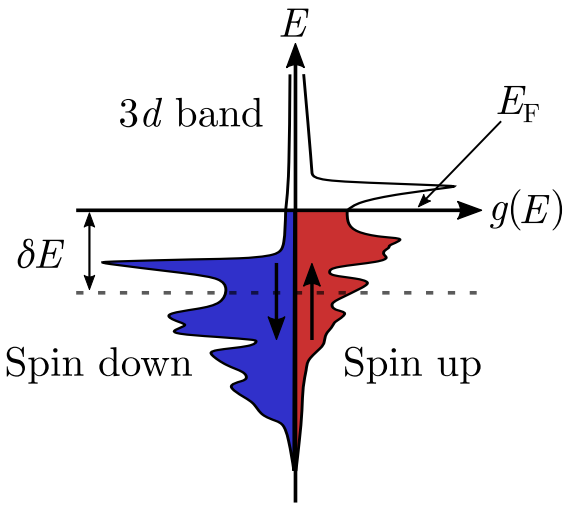

Figure 1.1: Schematic illustration of spontaneously spin-split bands in a $3d$ transition metal. The density of states $g(E)$ is shown for spin down (blue) and spin up (red) electrons, with the spontaneous energy splitting δE [67]. States are filled up to the Fermi energy E_F.

which is why it is sometimes called *itinerant ferromagnetism*. The Stoner-model of ferromagnetism explains the spontaneous magnetization of $3d$ metals in terms of spontaneously spin-split bands, where the energies of the spin-up and spin-down states are shifted, as shown in figure 1.1. This *exchange splitting*, as the name suggests, is caused by the exchange interaction, which reduces the overlap of the electronic wave functions and therefore the Coulomb repulsion.

It can be seen that this energy splitting results in a different density of states at the Fermi energy $g(E_\mathrm{F})$, which is used to define the *Stoner criterion*

$$Ug(E_\mathrm{F}) \geq 1, \tag{1.16}$$

with the Stoner parameter U, calculated from the exchange and Coulomb interaction, to assess whether or not ferromagnetism is possible in a system.

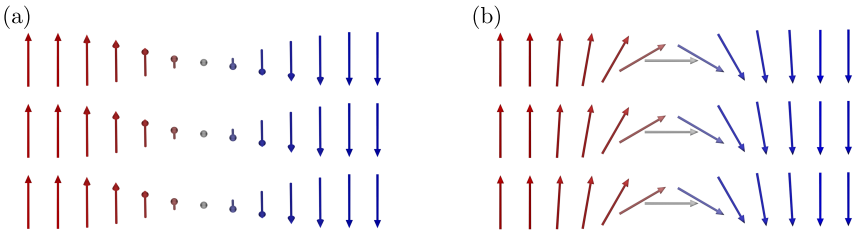

Figure 1.2: Schematic representation of a (a) Bloch type and (b) Néel type domain Wall. For Bloch type domain walls, the magnetization rotates in the plane parallel to the domain wall plane. Néel type domain walls have their magnetization rotate perpendicular to the plane of the domain wall.

Experiments on $3d$ transition metals find that their orbital momentum is extremely small, in contrast to the predictions of Hund's rules. This *orbital quenching* is caused by the interaction of the electrons with the crystal field, which is much stronger than the spin-orbit interactions, which in principle would produce a ground state with a large orbital angular momentum.

1.1.4 Domain Walls

The considerations regarding different magnetic anisotropies assumed a single domain state, meaning that all magnetic moments are aligned. This, however, comes at the cost of stray field energy, and a sample of sufficient size will therefore form domains with different orientations. The boundaries in between are called domain walls, and they can be characterized by the angle between adjacent domains, namely a 180° domain wall between domains with antiparallel magnetization and a 90° domain wall in the case of perpendicular magnetization [1].

Due to the exchange interaction, which, in a ferromagnet, tries to align neighboring spins, a domain wall also has a certain energy associated with it. A narrow domain wall will have a larger angle between the individual

moments, and hence a higher exchange energy, which would favor very broad domain walls. However, due to the magnetocrystalline anisotropy discussed in section 1.1.2, there's certain directions along which the moments are more easily aligned.
The competition between these energy contributions determine the domain wall width and orientation. The two most common variants of domain walls are called Bloch type, where the magnetization is rotated in a plane parallel to the domain wall, and Néel type, where the magnetization is rotated in a plane perpendicular to the plane of the domain wall. The two types are depicted in figure 1.2(a) and figure 1.2(b), respectively.
For a Bloch type domain wall, its width is given by [56]

$$\delta_{\mathrm{B}} = \pi\sqrt{\frac{A}{K}}, \tag{1.17}$$

where A denotes the exchange stiffness and K the anisotropy constant. For a Néel type wall, the width is given by

$$\delta_{\mathrm{N}} = \pi\sqrt{\frac{2A}{\mu_0 M_s^2}}, \tag{1.18}$$

where M_s denotes the saturation magnetization. By measuring domain wall widths, it is therefore possible to obtain information about microscopic parameters such as exchange stiffness and anisotropy constants. Typical values for $Ni_{80}Fe_{20}$ and YIG are on the order of 100 nm and 1 µm, respectively [68,69].

1.2 Magnetization Dynamics

While the previous sections have introduced the basic concepts of magnetic moments and their interactions in thermal equilibrium, this work focuses

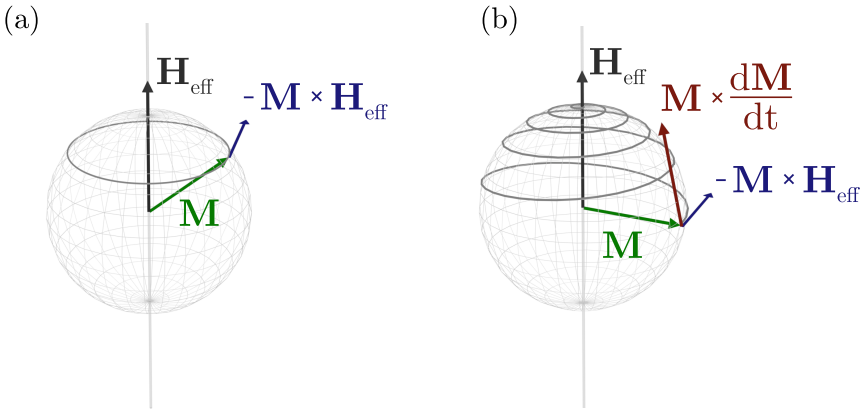

Figure 1.3: Illustration of the different terms of the Landau-Lifshitz-Gilbert equation. (a) Without damping, the magnetization $\mathbf{M}$ precesses around the effective field $\mathbf{H}_{\text{eff}}$. (b) When a small damping is introduced, the magnetization spirals towards the equilibrium position (adapted from [1]).

on the behavior of magnetic moments under the influence of an external driving force, such as an oscillating field. The following section describes the basic theories of the dynamical behavior of magnetic moments when deflected from their equilibrium position.

1.2.1 Landau-Lifshitz-Gilbert Equation

The differential equation governing the dynamics of the Magnetization $\mathbf{M}$ in a solid is the Landau-Lifshitz-Gilbert (LLG) equation [58]

$$\frac{\mathrm{d}\mathbf{M}}{\mathrm{d}t} = -\gamma\mu_0\left(\mathbf{M}\times\mathbf{H}_{\text{eff}}\right) + \frac{\alpha}{M_{\text{s}}}\left(\mathbf{M}\times\frac{\mathrm{d}\mathbf{M}}{\mathrm{d}t}\right), \tag{1.19}$$

with the gyromagnetic ratio γ, the effective field $\mathbf{H}_{\text{eff}}$, and the dimensionless phenomenological Gilbert damping parameter α.

The first term on the right hand side of the equation describes the

precession of magnetization around an effective external field, while the second term describes the damping of this precession, which eventually causes the magnetization to align with $\mathbf{H}_{\text{eff}}$. Figure 1.3 illustrates the geometrical relationship between the different terms.

A crucial feature of the LLG equation is the effective field $\mathbf{H}_{\text{eff}}$, which incorporates all the different interactions the magnetization might have with its surroundings. This includes but is not limited to contributions from Zeeman energy, stray field, anisotropies (magnetocrystalline and shape), and exchange interaction, all of which have been introduced in section 1.1. For such a system, the effective field can be calculated from the total energy density ϵ as [57]

$$\mathbf{H}_{\text{eff}} = \frac{\delta\epsilon}{\delta\mathbf{m}} = \frac{\delta\left(\epsilon_{\text{z}} + \epsilon_{\text{s}} + \epsilon_{\text{a}} + \epsilon_{\text{ex}}\right)}{\delta\mathbf{m}} \tag{1.20}$$

where ϵ_{z}, ϵ_{s}, ϵ_{a}, ϵ_{ex} are the energy densities of the Zeeman effect, stray field, anisotropy, and exchange interaction, respectively. The DMI is intentionally omitted due to its minor role in the systems studied throughout this work, but can in principle also be included. The LLG equation is used for the calculation of magnetization dynamics in micromagnetic frameworks and thus provides the basis for micromagnetic simulations and the macrospin model.

The damping parameter α as an empirical value can be experimentally determined using ferromagnetic resonance measurements (FMR), which will be discussed in more detail in section 2.4. It plays an important role for the propagation length of spin waves as magnonic devices require materials with a low damping parameter. There are only a few different common materials in use throughout magnonic research, namely a cobalt iron (CoFe) alloys with a damping on the order of $\alpha = 5 \times 10^{-4}$ [70], a nickel iron alloy (Permalloy, Py) with a damping on the order of $\alpha = 7 \times 10^{-3}$ [71], and the ferrimagnetic insulator yttrium iron garnet (YIG), with a damping on the order of $\alpha = 1 \times 10^{-4}$ [72].

1.2.2 Damping Mechanisms

The damping term of the LLG equation, while being phenomenologically motivated, reflects the fact that energy is dissipated when the magnetization precesses around the effect field. Several different mechanisms exist that can cause energy to be dissipated, and in practice it is oftentimes not possible to determine quantitatively the role of each mechanism [73]. One usually distinguishes between intrinsic and extrinsic contributions to the Gilbert damping.
Intrinsic Gilbert damping is caused by spin-orbit coupling and has been explained in terms of an *s*-*d* exchange relaxation model [74,75] as well as using a breathing Fermi surface model [76,77]. Which model is best suited depends on the system one is interested in and can not be answered in general.
Extrinsic Gilbert damping can be caused by crystallographic defects, impurities, and inhomogeneities [78]. It is influenced by a samples growth parameters and can be understood in terms of two-magnon scattering, or scattering between magnons and phonons [79]. Another extrinsic dissipation mechanism is spin-pumping, where a precessing magnetization induces a spin-current at an interface [80]. Typically, intrinsic and extrinsic are of comparable magnitude, making it even more difficult to separate their influence.

1.2.3 Spin Waves

The quanta of the collective excitation in a magnetic system are called magnons, and can described as bosonic quasi particles with spin 1. Every magnetic systems with nonzero temperature gives rise to magnons due to thermal fluctuations. Owing to their stochastic nature, they are excited at different frequencies and arbitrary phases [56].

It is however possible to excite coherent spin-wave dynamics by means of an oscillating magnetic field, which couples to the magnetic moments according to the LLG equation introduced in section 1.2.1. Using this method, it is possible to excite spin waves that can travel through the magnetic material up to lengths limited by their group velocity and lifetime. In the case of Permalloy, the decay length (the distance at which the amplitude has decreased by a factor of $1/e$) is found to be on the order of several microns[81], and it can even reach values of more than millimeter[82,83] in the case of YIG.

Most research has focused on spin waves in magnetic thin films, mostly due to their technological significance. In the case of a thin film, one differentiates between three main spin-wave modes, with different relative orientation of the thin film normal, the wave-vector $\mathbf{k}$, and the equilibrium magnetization direction $\mathbf{M}$. On the left side of figure 1.4, these three modes are depicted, with the thin film stretching across the x-y-plane and the waves traveling along the x-direction towards the left.

The top panel shows the Damon-Eshbach type spin wave, where the equilibrium magnetization is orthogonal to the direction of wave propagation. The counter-clockwise sense of rotation of the individual magnetic moments is determined by the LLG equation. Damon-Eshbach type spin waves are sometimes labeled *magnetostatic surface spin waves* since they occur on the thin film surface and their amplitude decays exponentially the further you go into the material[84].

The middle panel shows the *forward volume* type spin waves. In this case, the magnetization points out-of-plane, and again the wave propagation is orthogonal to it. As the name suggests, this type of spin wave does not only occur on the surface, but occupies the entire volume of a thin film[84]. The same is true for *backward volume* type spin waves, which are also not confined to the film surface. They owe their name to the fact that in a certain regime, where dipolar interactions dominate, their group velocity is negative[84].

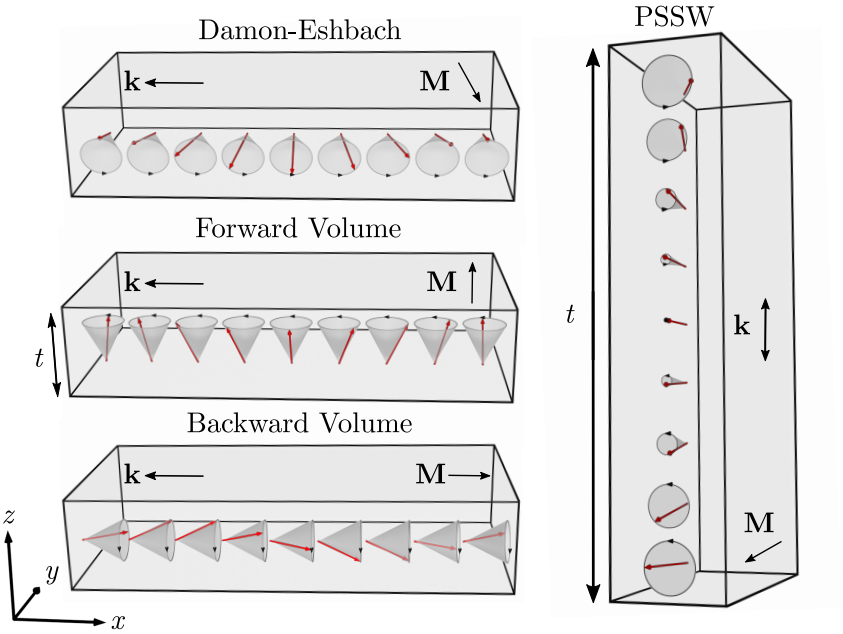

Figure 1.4: Illustration of the different spin-wave modes that can occur in a uniformly magnetized thin film with equilibrium magnetization **M** and wave-vector **k**. The thin film lies in the x-y-plane, with its thickness t along the z-direction.

The spin-wave mode depicted on the right side of figure 1.4 can be understood as higher order modes, where standing waves across the thin film thickness form. They are characterized by the number of anti-nodes present.

In the case of figure 1.4, a perpendicular standing spin-wave (PSSW) with $n = 1$ is depicted. For an isotropic, homogeneously in-plane magnetized thin film, it is possible to obtain an analytical solution for the spin-wave dispersion relation[59]. Figure 1.5 shows the dispersion relation of the aforementioned Damon-Eshbach and Backward volume modes,

calculated according to [85]

$$\omega(\mathbf{k}) = \Bigg[(\omega_\mathrm{H} + \omega_\mathrm{M}\lambda_\mathrm{ex}k^2)\Bigg(\omega_\mathrm{H} + \omega_\mathrm{M}\lambda_\mathrm{ex}k^2 + \omega_\mathrm{M}\Bigg(1+ g_k(\sin^2(\theta_k) - 1) + \frac{\omega_\mathrm{M} g_k(1-g_k)\sin^2(\theta_k)}{\omega_\mathrm{H} + \omega_\mathrm{M}\lambda_\mathrm{ex}k^2}\Bigg)\Bigg)\Bigg]^{1/2}. \tag{1.21}$$

To bring it into this relatively compact form, the abbreviations $\omega_\mathrm{H} = \gamma\mu_0 H_\mathrm{eff}$, $\omega_\mathrm{M} = \gamma\mu_0 M_\mathrm{s}$, $\lambda_\mathrm{ex} = 2A_\mathrm{ex}/(\mu_0 M_\mathrm{s}^2)$, and $g_k = 1-(1-\exp(-kt))/(kt)$ are used, with k being the magnitude of the wavevector $\mathbf{k}$, γ the gyromagnetic ratio, A_ex the exchange constant, H_eff the effective field, M_s the saturation magnetization, t the film thickness and θ_k the angle between the spin-wave wavevector and magnetization direction [85]. Using equation (1.21), it is not only possible to calculate the two special cases of parallel or orthogonal orientation of wavevector and magnetization, corresponding to the BV and DE mode, respectively. It is also possible to obtain the dispersion relation for arbitrary angles between $\mathbf{k}$ and $\mathbf{M}$. For out-of-plane magnetized thin films, the dispersion relation of the forward volume mode can be obtained using [85]

$$\omega(\mathbf{k}) = \Bigg[(\omega_\mathrm{H} + \omega_\mathrm{M}\lambda_\mathrm{ex}k^2)\Bigg(\omega_\mathrm{H} + \omega_\mathrm{M}\lambda_\mathrm{ex}k^2 + \omega_\mathrm{M}\Bigg(1 - \frac{1-e^{-kd}}{kd}\Bigg)\Bigg)\Bigg]^{1/2}, \tag{1.22}$$

and the resulting curve is also shown in green in figure 1.5.

To obtain these dispersion relations, both dipolar and exchange interaction have to be taken into account. For long wavelengths, and therefore small $\mathbf{k}$, the dipolar interaction dominates, whereas for short wavelengths and large $\mathbf{k}$, exchange dominates [84].

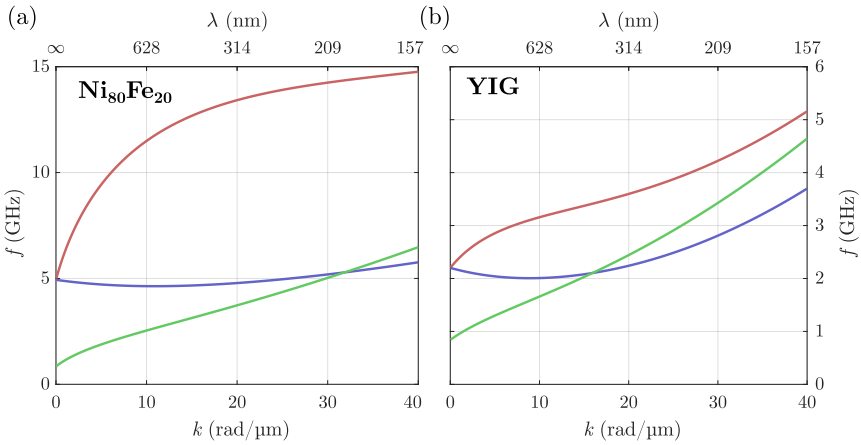

Figure 1.5: Dispersion relation for Damon-Eshbach (red), Backward Volume (blue), and Forward Volume (green) type spin waves for (a) a 50 nm thick $Ni_{80}Fe_{20}$ film with $A_{ex} = 1.3 \times 10^{-11}$ J/m, $M_s = 800$ kA/m, $H_{ext} = 30$ mT and (b) a 50 nm thick YIG film with $A_{ex} = 0.36 \times 10^{-11}$ J/m, $M_s = 140$ kA/m, $H_{ext} = 30$ mT.

Wavelength range

When a microstrip is used for the excitation of spin-waves, the accessible range of wavelengths is limited by the underlying excitation mechanism [86]. The minimum wavelength stems from the fact that a microstrip cannot excite spin waves far below their own width, because underneath the microstrip, the Oersted field is roughly uniform, so all magnetic moments in that area will be in phase. The maximum is found to be where the magnetic field is such that one would in principle excite the ferromagnetic resonance (FMR) mode, however, it is not possible excite this mode since the excitation is confined to the area surrounding the microstrip. In between these two extremes, the wavelength increases for increasing magnetic field strength. From equation (1.21) it can be seen that for a fixed frequency, increasing the external field will result in lower **k**, and

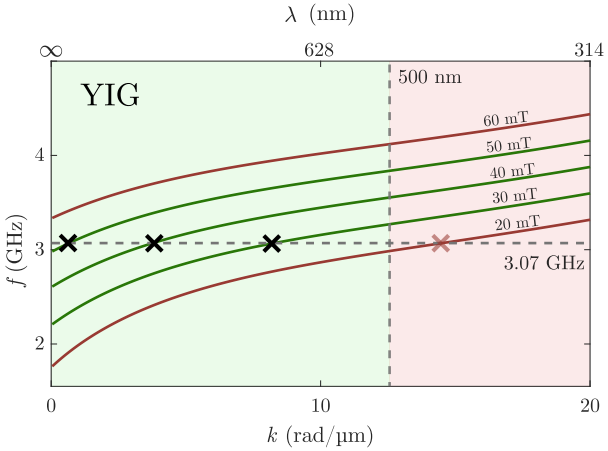

Figure 1.6: Calculated dispersion relation for different applied magnetic field strengths of a 100 nm YIG film. The dashed line parallel to the y-axis indicates the width of the microstrip, the one parallel to the x-axis indicates a fixed excitation frequency of 3.07 GHz, with black crosses marking the intersection with the dispersion relation.

therefore longer wavelengths. Another way of illustrating this is by looking at the dispersion relation for Damon-Eshbach type spin waves at different field strengths, shown in figure 1.6. When increasing the external field, the shape of the dispersion relation is left more or less unchanged, but is shifted towards higher frequencies, meaning that for a fixed frequency, the wavelength will become longer. Increasing the magnetic field above a certain threshold will shift the curve so far up that the FMR mode ($k = 0$) will be above the excitation frequency, so no spin waves are excited. Going the other way, decreasing the magnetic field, will result in a downward shift of the dispersion, meaning that the wavelengths become shorter. When this wavelength drops below the width threshold of the microstrip, no spin waves will be excited. This is indicated by the red area in figure 1.6.

1.3 X-ray Magnetic Circular Dichroism

The interaction between x-rays and condensed matter can be used to study chemical and structural properties. It is usually distinguished between *soft* (up to 3 keV) and *hard* x-rays (everything above 5 keV). One major advantage of using x-rays compared to optical techniques is that their wavelength is much shorter (10 nm and below) than that of visible light, and therefore higher spatial resolution can be reached [1]. In the soft x-ray regime, photoabsorption is the dominant light-matter interaction, with a cross section that lies more than three orders of magnitude above other interactions [87].

Fermi's Golden Rule

When a photon with energy $E_{\mathrm{ph}} = \hbar\omega$ interacts with the electron of a core shell, it can result in the excitation of the electron from its initial state $|i\rangle$ to an excited final state $|f\rangle$ with energy $E_f = E_i + E_{\mathrm{ph}}$. The transition probabilities are given by *Fermi's golden rule*,

$$P_{if} = \frac{2\pi}{\hbar} \left|\langle f|\mathcal{H}|i\rangle\right|^2 \delta(E_i - E_f)\rho(E_f), \tag{1.23}$$

where $\mathcal{H}$ denotes the Hamiltonian, δ the Dirac delta function, and $\rho(E_f)$ the density of states at the energy of the final state. When the initial state is sufficiently localized, it is valid to use a dipole approximation, which results in the three well known selection rules $\Delta l = \pm 1$, $\Delta m = 0, \pm 1$ and $\Delta j = 0, \pm 1$. So in principle, both $p \to s$ and the $p \to d$ transitions are allowed, but the corresponding transition matrix element $\left|\langle f|\mathcal{H}|i\rangle\right|^2$ is two orders of magnitude smaller for the $p \to s$ than that for the $p \to d$ transition, rendering it irrelevant in experiments.

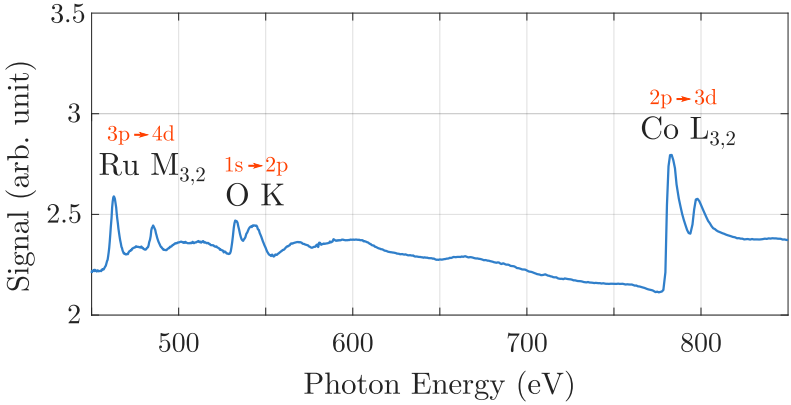

Figure 1.7: Exemplary XAS measurement of a sample containing Ru, Co, and O. The absorption edges are labeled, together with the corresponding electronic transitions.

Equation (1.23) relates the transition probabilities between different states, and therefore the absorption coefficient, to the final state density. Looking at it the other way round, the measured absorption coefficient contains information about the elemental composition and the chemical environment of a sample, which is used in x-ray absorption spectroscopy (XAS)

XAS

The basic idea of XAS is to measure the absorption coefficient μ as a function of photon energy E[87]. When the photon energy matches an electronic transition in the material, μ will increase significantly, resulting in the enhancement of absorption by one order of magnitude or more. The sharp increase of μ is called an *absorption edge* with typical energies of the atomic species. They are named after the corresponding electronic transition, more precisely after the principal quantum number of the excited

electron. For a $1s$ electron, it is called a K-edge, for $2s$ and $2p$ electrons it is called an L-edge, and so forth [87]. The edges are then indexed according to their energy, starting with the highest value, and they are dominated by electronic transitions fulfilling the dipole selection rules.

Figure 1.7 shows an exemplary XAS measurement ranging from 450 eV to 850 eV with the different edges labeled. From the data, one can infer that the sample contains Ru, Co, as well as oxygen by comparing the position of the absorption edges to literature values [88,89]. One can see that there is some resonant behavior at the absorption edges. Following Fermi's golden rule, the shape of the main peak reflects the density of the unoccupied states and therefore contains information about the chemical environment, for example the oxidation state. In general, the absorption decreases as a function of energy by $E^{-7/2}$ due to non-resonant absorption.
In the context of this work, XAS is mainly used to determine the oxidation state of a material by comparing the spectrum to reference data.

XMCD

In magnetic materials, the absorption cross section of x-rays is also dependent on the relative alignment of the photon angular momentum $\mathbf{L}_{\mathrm{ph}}$ and the samples magnetization $\mathbf{M}$, according to [1]

$$\Delta\mu \propto \mathbf{L}_{\mathrm{ph}} \cdot \mathbf{M}. \tag{1.24}$$

This effect lies at the heart of this work and will be exploited in order to obtain magnetic contrast for detecting spin waves and imaging spin textures. This can be done by either changing the x-ray polarization, or reversing the magnetization direction, as is illustrated in figure 1.8(b). The change in absorption is caused by the *x-ray magnetic circular dichroism* (XMCD) effect [52], which can be understood in terms of a two step process.

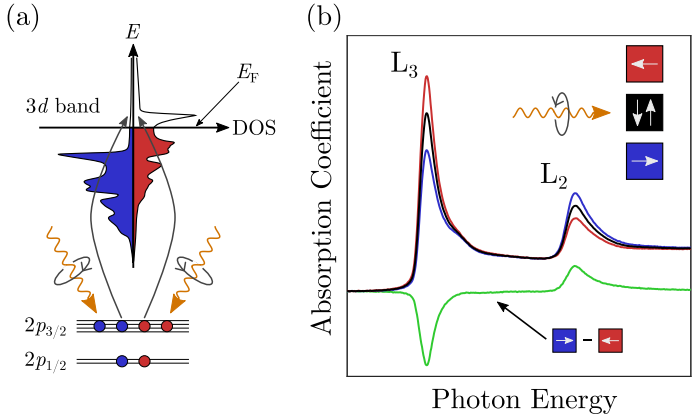

Figure 1.8: Schematic illustration of the XMCD effect in Co. (a) Two step model for the excitation of electrons from $2p$ to $3d$ states by circularly polarized photons. In the Stoner model, the spin-up and spin-down states are shifted in energy by the exchange interaction. (b) Exemplary XAS spectra for the different alignments of photon angular momentum and sample magnetization (red, blue, black), and corresponding XMCD spectrum (green). (adapted from [1])

First, by absorption of a circularly polarized x-ray photon, an electron is excited from a core shell state to the continuum or unoccupied state with a fixed spin polarization $\langle\sigma_z\rangle$ along the photon k-direction z. The electrons spin is related to the photon polarization, meaning that left and right hand circularly polarized light will excite electrons with opposite spins, and so the spin polarization reflects the spin orbit coupling of the initial state. For the initial $2p_{1/2}$ (L-S) and $2p_{3/2}$ (L+S) states, $\langle\sigma_z\rangle$ is -1/2 and +1/2, respectively. Thus, the spin polarized photoelectron is an internal probe of the spin polarization of the empty $3d$ states, which in the case of the Stoner model is split by the exchange interaction, as was discussed in section 1.1.3 and can be seen in figure 1.8(a). Since no spin-flip can occur ($\Delta m_s = 0$), this means that for one polarization, there are more available states for the electrons, which results in a higher absorption coefficient μ. The spin-orbit

interaction has opposite signs for the $2p_{3/2}$- and $2p_{1/2}$-electrons, which results in opposite signs for the XMCD effect at the L_3- and L_2-edges. The initial state spin-orbit interaction will not only result in a spin polarization of the excited electrons, but also in a polarization with regards to the electrons orbital momentum. This effect, however, has the same sign for the L_2 and L_3 edge, and so it is possible to disentangle these two effects using so-called *sum rules*, which can be used to determine both the spin- as well as orbital momentum of the electrons in an element specific manner.

2 | Experimental Methods

In this chapter, the experimental aspects relevant for this work are discussed. This includes both measurement and sample preparation methods.

2.1 Synchrotron Radiation

Time-resolved magnetic soft x-ray microscopy relies on the availability of synchrotron radiation. A schematic illustration of a synchrotron is shown in figure 2.1(a). If the electrons are deflected by an external field, for example by the bending magnets that force the electrons into their circular orbit by means of Lorentz force, bremsstrahlung radiation is emitted [91]. The wavelength of the emitted radiation depends on both the electron energy and the curvature of the trajectory. For bending magnets, the characteristic wavelength λ_c can be approximated as

$$\lambda_c = \frac{4\pi m_e c}{3eB\gamma^2}, \tag{2.1}$$

where c denotes the speed of light in vacuum, m_e the rest mass of the electron, e the elemental charge, B the magnetic flux density of the bending

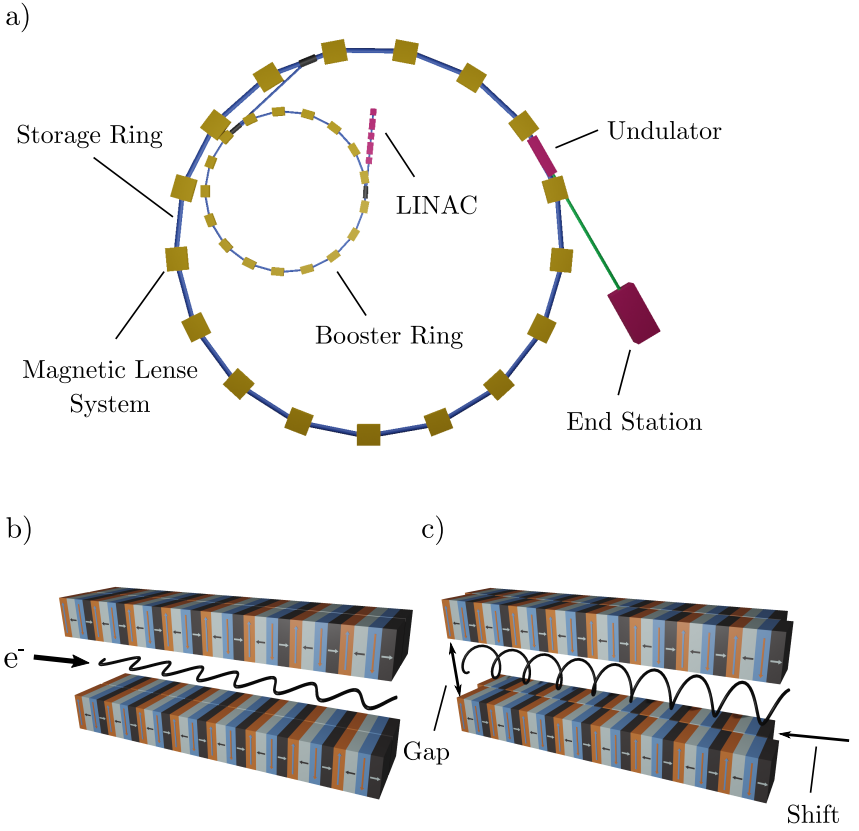

Figure 2.1: (a) Schematic illustration of a synchrotron with three stages: linear accelerator (LINAC), booster ring and storage ring. (b,c) Operation principle of an APPLE type undulator producing (b) linearly and (c) circularly polarized light using four differently oriented permanent magnets. Both gap size and displacement (shift) can be controlled, determining photon energy and polarization, respectively [90].

magnet, and

$$\gamma = \frac{1}{\sqrt{1 - \frac{v^2}{c^2}}} \tag{2.2}$$

the Lorentz factor of the electron moving at velocity v [90]. For an electron with an energy of 1.7 GeV, $\gamma \approx 3328$, which means it moves at 99.999 995 % of the speed of light. The first experiments with synchrotron radiation were performed at electron accelerators where the bremsstrahlung was only an unintentional by-product of the bending magnets. Nowadays, there are many large facilities worldwide that are specialized in providing synchrotron radiation for scientific experiments. Some of the experiments listed in this thesis were performed at the electron storage ring BESSY II at the Helmholtz-Zentrum Berlin (HZB), at the MAXYMUS beamline, which is located behind an undulator [92]. An aerial view of the facility, as well as a view into the microscope, can be seen in figure 2.2. The following explanations therefore refer to the techniques used at this particular beamline, but most statements apply to synchrotron facilities in general. A measure of the quality of the emitted radiation is the brilliance B, which can be calculated according to

$$B = \frac{N_{\mathrm{ph}}}{\Delta\Omega \cdot \frac{\Delta\lambda}{\lambda} \cdot t} \tag{2.3}$$

from the photon count N_{ph} per time interval t of a light source that emits in the wavelength interval $\frac{\Delta\lambda}{\lambda}$ in a solid angle $\Delta\Omega$ [95]. Due to the relativistic speed of the electrons, the solid angle in which the electrons radiate is very narrow, which increases the brilliance of synchrotron light sources. BESSY II provides radiation with an opening angle of only 3.0×10^{-4} rad [96].

As the electrons emit radiation during operation, they gradually lose energy. In the so-called *top-up* mode, high-energy electrons are continuously injected into the storage ring with the aid of a fast-switching magnet. Thus, an average beam current of about 300 mA can be maintained, with individual electrons having kinetic energies of up to 1.7 GeV, making it

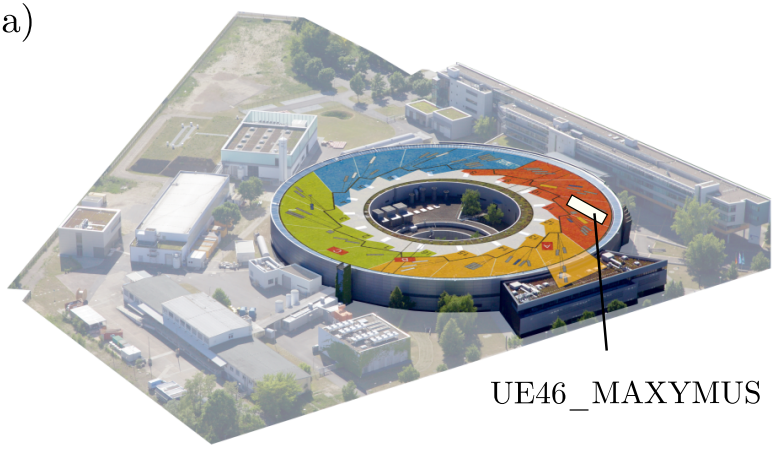

Figure 2.2: (a) Aerial view of the BESSY II synchrotron facility at the Conrad-Wilhelm-Röntgen Campus of the HZB, with the UE46 beamline highlighted. ©HZB/Dirk Laubner (adapted from [93]) (b) View inside the MAXYMUS microscope[94].

possible to reach x-ray photon energies of up to 1.8 keV [93].

Undulators - while early experiments were limited to bending magnets, there are now so-called *undulators* in which the electron beam is deflected by two parallel rows of periodically arranged magnets, causing them to emit intense, coherent bremsstrahlung in a small wavelength range in the direction of the electron beam. The spacing of the magnets in the undulator and the displacement of the two rows relative to each other determine the wavelength and polarization, respectively, of the emitted radiation [91]. The schematic structure of such an undulator is shown in figure 2.1(b) and (c) for linearly and circularly polarized light, respectively.

The resulting radiation is not monochromatic enough for XAS and XMCD measurements, so the light is directed to a monochromator consisting of a grating, a rotating mirror, and a slit aperture. The grating scatters the light depending on the wavelength, and the mirror is adjusted so that the desired wavelength hits the slit aperture.

Energy resolution - the width of the aperture determines the wavelength selectivity, but at the expense of light intensity. Thus, when very high energy resolution is required, for example when x-ray absorption spectra are acquired, the aperture can be chosen to be very small. When high light intensity is needed, for example in the case of thicker samples with low transmission, the aperture can be opened to let more light through.

Time structure - as the electrons move through the undulator in bunches, the emitted radiation is also emitted in short flashes of light. The length of these light flashes determines the highest possible temporal resolution of the dynamic measurements and varies depending on the operating mode. In the so-called *low-alpha* mode, the half-width of the pulses is about 12 ps, in the normal *multibunch* mode about 45 ps [90].

Coherence - highly coherent light is needed in order to perform certain

static and dynamic x-ray imaging techniques that rely on the interference of different parts of the beam. Examples for these techniques are x-ray ptychography and holography. One distinguishes between temporal and spatial coherence, quantifiable with coherence lengths L_T and L_S, respectively. The temporal coherence length measures the longitudinal distance after which the phase of a point source has shifted by 180° and therefore is a measure for the phase stability. It determines whether or not interference patterns can be observed from a light source. Spatial coherence measures the correlation between different parts of the wave emitted by a spatially extended source. The spatial coherence length is determined by the transverse distance of two points on the source, from which emitted waves can still interfere, so again the distance where the phase shift is smaller than 180°. Spatial coherence can be achieved by introducing a pin hole or slit apertures, since it reduces the size of the source, although at the cost of reduced photon flux.

2.2 Scanning Transmission X-ray Microscopy

The absorption of x-rays interacting with matter was introduced in section 1.3, and it serves as a basis for the imaging technique of scanning transmission x-ray microscopy (STXM). Figure 2.3 shows a sketch of the basic experimental setup, similar to the one used at the MAXYMUS endstation [90].

Monochromatic x-rays from the synchrotron source are being focused onto the sample using a Fresnel zone plate (FZP), which consists of concentric rings of alternating refractive indices with their width decreasing outward [97]. The size of the outermost ring determines the spatial resolution of this kind of x-ray lens. The rings are arranged in a way where incident

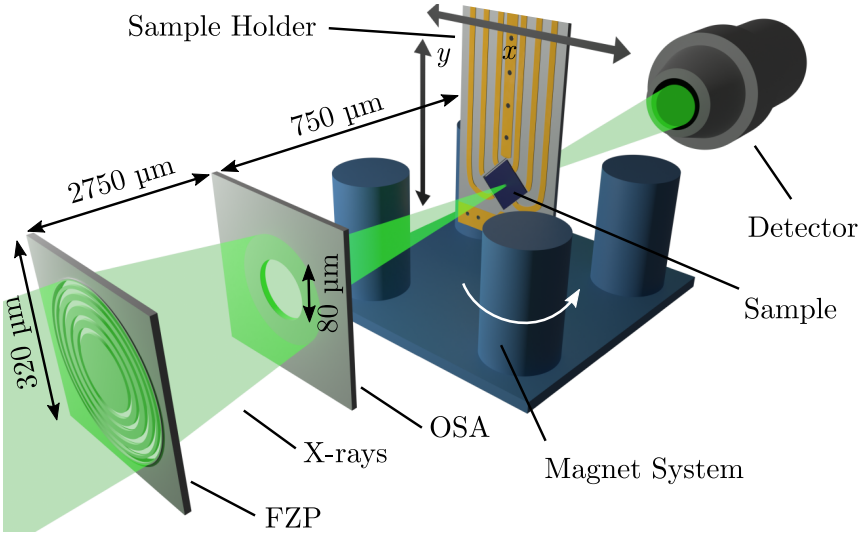

Figure 2.3: Sketch of the scanning transmission x-ray microscopy setup. The x-rays from the synchrotron (green) are focused by a Fresnel zone plate (FZP) onto the sample, and higher orders are blocked by an order sorting aperture (OSA). The sample can be moved along the x- and y-axis. The magnet system consists of four permanent magnets that are rotatable around the z-axis. Typical distances for a measurement at 710 eV are given.

collinear light interferes constructively at the focal point, and interferes destructively around it. This approach based on diffraction is necessary since the refractive index of x-rays in materials is close to unity, which renders ordinary lenses ineffective. There are also rings of higher order constructive interference, which need to be blocked by an order-selecting aperture (OSA). Using a FZP, it is possible to reach beam diameters at the focal point of less than 20 nm, which ultimately limits the spatial resolution of this imaging technique [98].

Scanning over the sample is achieved by piezoelectric actuators, which are used to control the sample position down to the nanometer scale.

For transmission experiments, the penetration depth of light has to be

larger than the sample thickness. The number of photons transmitted can then be measured using an avalanche photo diode. The biggest advantage of this method is that it's unaffected by external magnetic and electric fields.

The Beer-Lambert law [99]

$$I(t) = I_0 \cdot e^{-\mu(E)t} \tag{2.4}$$

describes the attenuation of light with initial intensity I_0 after traversing material of thickness t with a wavelength-dependent absorption coefficient $\mu(E)$.

As described in section 1.3, the material- and wavelength-dependence of the absorption coefficient $\mu(E)$ can be used to perform element-specific studies and give a material-dependent contrast, which is needed for imaging. Additionally, in the x-ray microscope MAXYMUS, the XMCD effect is used for determination of the local magnetization. A system of four rotatable permanent magnets allows for the control of the magnetic field at the sample position [90]. Depending on the relative orientation of magnetization and photon angular momentum, the absorption will be increased or decreased, as discussed in section 1.3. This effect can therefore be used to obtain purely magnetic contrast by taking two images, one with left- and one with right-handed circular polarization, and calculating the difference. Instead of changing the light polarization, it is also possible to reverse the magnetic field direction, as long as the sample is saturated along the field.

2.3 Dynamic Magnetization Measurement

The STXM setup described in section 2.2 can also be extended to allow for time-resolved measurement of a samples dynamic magnetization by exploiting the time structure of the synchrotron radiation [90,100]. This is

achieved by means of an asynchronous pump-probe scheme utilizing an avalanche photodiode (APD) that allows for the detection of single photons while being able to discriminate between time intervals down to 1 ns. This is necessary for matching the photon detection events to individual x-ray pulses, which at the BESSY II synchrotron facility come at a frequency of 500 MHz, as discussed in section 2.1. A customized field-programmable gate array (FPGA)-based counting board directly synchronized to the RF clock of the storage ring is used for detection and sorting of the x-ray photons[54].

Asynchronous excitation - the most straightforward way of stroboscopic probing would be to synchronize the pump pulses to the synchrotron bunch frequency. With this method, however, it is only possible to achieve a time resolution of 2 ns. To increase the temporal resolution, an asynchronous pump-probe scheme is implemented, where the pump frequency is chosen in a way so that after each synchrotron pulse, a time shift in the pump cycle is induced. The integer N determines the number of channels and therefore the number of frames in the resulting dynamic measurement. This means that after $t = N \cdot 2\,\mathrm{ns}$, the excitation signal has to repeat itself. The lowest frequency measurable with this setup is therefore $f_\mathrm{b} = 500\,\mathrm{MHz}/N$, it is however possible to measure every integer multiple of this base frequency $M \cdot f_\mathrm{b}$ with an integer M. In order for this scheme to work and to avoid phase degeneration of time channels , M and N have to be coprime.

Figure 2.4 shows this sampling scheme for continuous sinusoidal excitation with frequency

$$f = 500\,\mathrm{MHz} \cdot \frac{M}{N} \tag{2.5}$$

in the case of $N = 7$ channels. It can be seen that for certain combinations of M and N, it is necessary to rearrange the sampling points in order to retrieve the actual signal. Written in pseudocode, the sorted array S of

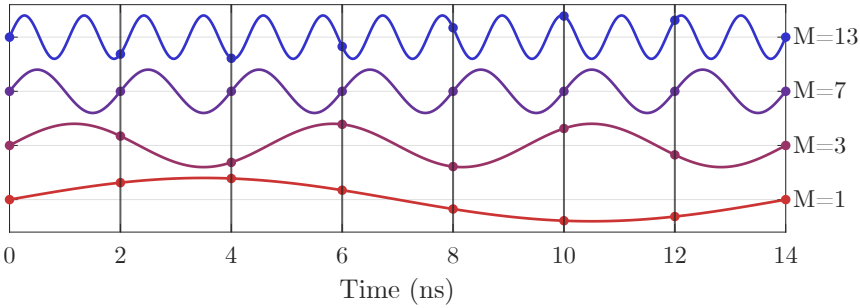

Figure 2.4: Illustration of the sampling method used in the dynamic STXM measurements for $N = 7$ channels and different M (adapted from [54]).

sampled points can be obtained from the unsorted array U according to

$$\mathrm{S}[i] = \mathrm{U}[\mathrm{modulo}(i \times M, N)]. \tag{2.6}$$

Pump signal generation - at the MAXYMUS endstation, an arbitrary waveform generator (AWG) can be used for realization of the pump signal[101]. The Keysight M8195A AWG is synchronized to the synchrotron frequency to ensure phase stability between pump and probe signal. It is able to synthesize arbitrary signals with a sampling rate of 65 GS/s (Gigasamples per second) with four individually controllable output channels.

In order to excite spin-wave dynamics, the pump signal is applied to a microstrip, which, through the induced Oersted Field, couples to the magnetic material[86]. This way, spin waves with a certain fixed frequency can be excited, as long as their wavelength is not much smaller than the microstrip size.

Fast Fourier Transform Analysis

Using the data obtained by the previously discussed method, it is possible to transform the data from the time into the frequency domain using a fast Fourier transform (FFT) algorithm[81]. While inherently only sensitive to certain frequencies, as determined by N, it is possible to detect spin waves with different M and therefore different frequencies using this method. In the normal spin-wave movies, it can be difficult to discriminate between the different spin-wave modes, however, when analyzed in the frequency domain, they are easily distinguishable.
To that end, the raw data of each pixel, comprising the data of N time steps, is analyzed by means of a temporal FFT. With the correct normalization, the absolute value of the complex FFT corresponds to the magnetization amplitude $A(x, y, f)$ and the argument to the relative phase $\varphi(x, y, f)$, both for a pixel with coordinates x, y, and frequency slice f.[81]
The normalization of the intensity I at position (x, y) and time t is done according to

$$I_{\mathrm{norm}}(x, y, t) = \ln(I(x, y, t)/I_{\mathrm{mean}}(t)) \cdot I_{\mathrm{mean,tot}}, \tag{2.7}$$

where $I_{\mathrm{mean}}(t)$ denotes the mean photon count of all pixels for one time step and $I_{\mathrm{mean,tot}}$ the average over all pixels and time steps. The natural logarithm is calculated to convert the photon count into something that is proportional to the absorption coefficient μ, according to equation (2.4).

2.4 Ferromagnetic Resonance Measurements

Section 1.2 has already covered the basics of the dynamic behavior of magnetic moments when deflected from their equilibrium position. This

behavior can be described by the Landau-Lifschitz-Gilbert equation, where the dynamics depend on various system-specific energy terms, which are summarized in the effective field H_{eff}. A system of many coupled magnetic moments aligned by an external static field can be excited to oscillate collectively by an external oscillating magnetic field, since the external field exerts a torque on the magnetic moments. If the frequency of the externally applied magnetic field matches the resonance frequency of the system, all the magnetic moments will oscillate in phase, and the system is said to be ferromagnetically resonant [48].

The resonance frequency in the case of a magnetic film with the external field in the film plane can be calculated using the Kittel formula

$$f = \frac{\gamma}{2\pi}\sqrt{B(B + \mu_0 M_{\text{eff}})}, \tag{2.8}$$

where B denotes the strength of the external static magnetic field, γ is the gyromagnetic ratio, and M_{eff} is the effective magnetization of the ferromagnet [48]. The effective magnetization can be calculated from the saturation magnetization M_{s} and the anisotropy constant K_{U} according to $M_{\text{eff}} = M_{\text{s}} - 2K_{\text{u}}/M_{\text{s}}$.

For thin films that have their magnetization lying perpendicular to the film plane, the corresponding equation is

$$f = \frac{\gamma}{2\pi}(B - \mu_0 M_{\text{eff}}). \tag{2.9}$$

Using equation (2.8) for in-plane magnetized films, or equation (2.9) for out-of-plane magnetized films, the gyromagnetic ratio and the magnetization of a sample can be inferred from measurements of the resonance frequency and linewidth at different external fields, which is often used in the characterization of ferromagnetic materials.

Gyromagnetic ratio - the gyromagnetic ratio, which relates a particles angular momentum to its magnetic moment, is also sometimes expressed

in terms of the g-factor. For an electron, it is related via

$$\gamma_e = g_e \frac{\mu_B}{\hbar} = \frac{|\mu|}{|L|}, \tag{2.10}$$

where μ_B denotes the Bohr magneton, $\hbar$ the reduced Planck's constant, μ the particles magnetic moment and L it's total angular momentum [1]. For a free electron, the value of g can be calculated to be approximately 2.002 using quantum electrodynamics. When g is deduced from FMR experiments using equation (2.8) and (2.9), values larger than 2.002 are obtained, in the case of $3d$ transition metals usually between 2.1 and 2.2 [102]. This can be understood by distinguishing between the Landé g-factor, which is defined in atomic physics within a quantum mechanical framework, and the more empirically motivated term g, sometimes called the *spectroscopic splitting factor*, which appears in equation (2.8) and (2.9) [103]. Its definition is based on the validity of an effective field approach, which is not necessarily the case in a real material.

Experimental realization - in an FMR experiment, either the frequency can be kept fixed and the external field varied, or the frequency can be swept if the external field is fixed [104]. For example, if a microwave cavity resonator is used, usually a fixed frequency is applied and the external field is varied, with a microwave detector measuring the absorption of the sample. The external field is usually generated and controlled by means of a Helmholtz coil. Near the resonance condition, the system absorbs significantly more energy, which can be seen in a sharp increase in absorption. Another method generates the field locally on the sample using a microstrip, or a coplanar waveguide. A sketch of this kind of experimental setup can be seen in figure 2.5. When an alternating current runs through the structure, an Oersted field is generated around it, which can excite nearby magnetic moments to oscillate. The increased absorption of the system, and hence resonant excitation, can then be detected by a vector network analyzer (VNA-FMR), which measures the complex scattering parameters S_{11}, S_{12},

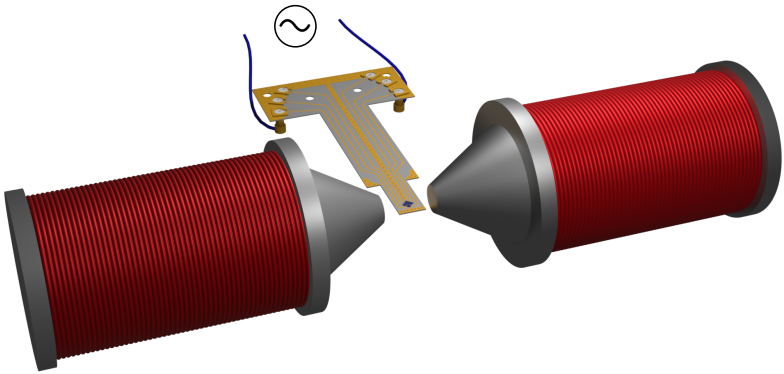

Figure 2.5: Experimental setup for measuring ferromagnetic resonance. A magnetic field is produced by two Helmholtz coils, while an alternating current is transmitted through the sample. A VNA is used to measure the complex scattering parameters in order to determine resonance frequencies and linewidths.

S_{21}, and S_{22}. These provide information about reflection (S_{11} and S_{22}) and transmission (S_{12} and S_{21}) of the signal, and thus about ferromagnetic resonance [105]. Again, at a fixed frequency, the absorption of microwaves by the sample is often measured in the presence of varying magnetic field generated by a Helmholtz coil.

Lock-in technique - to improve the signal-to-noise ratio, another Helmholtz coil can be introduced into the system, which superimposes a time-varying component H_{AC} with a field strength on the order of only 0.1 mT on the static external field H_{DC}. Now the measured signal can be analyzed by means of a lock-in amplifier, which is adjusted to the frequency of H_{AC}, which can lead to a significant improvement of the measurement [106].

The absorption of the sample is given by the imaginary part of the complex dynamical susceptibility χ, which can be derived using the LLG equation. In the case of a saturated sample as a function of applied field

H_0, one obtains a symmetrical Lorentzian curve described by

$$\chi'' = M_S \frac{B_{eff}}{B_{eff} + \mu_0 H_{eff}} \cdot \frac{\Delta H}{\Delta H^2 + (H_0 - H_{FMR})^2}, \tag{2.11}$$

where B_{eff} and H_{eff} denote the effective flux density and the effective field strength, respectively, which depend on the anisotropy of the system, M_S is the saturation magnetization, and ΔH the linewidth of the resonance[104]. This equation can be used to fit the FMR measurement data in order to determine H_{FMR} and ΔH.

Analogous to the damped harmonic oscillator, increased damping also causes a broadening of the resonance peak in the case of ferromagnetic resonance. This can be quantified by the linewidth ΔH, which, using the empirically motivated equation

$$\Delta H = \frac{4\pi f \alpha}{\gamma \mu_0} + \Delta H_0 \tag{2.12}$$

yields the Gilbert damping parameter α, where ΔH_0 denotes the extrapolated linewidth at $f = 0$[107].

The experimental method of ferromagnetic resonance thus allows characterization of a magnetic thin film in terms of gyromagnetic ratio, effective magnetization, anisotropies, and Gilbert damping.

2.5 SQUID Magnetometry

A superconducting quantum interference device (SQUID) is used to measure magnetic fields with extremely high sensitivity[108]. It uses a superconducting loop interrupted by Josephson junctions to measure an electric current that changes as a function of the externally applied field, exploiting the fact

that magnetic flux in a Josephson junction can only change in multiples of $2e/h$. A SQUID magnetometer uses this principle to measure the magnetic moment of a sample by moving it through a set of detection coils that react to the sample's stray field. In a vibrating sample magnetometer (VSM), this movement is repeated periodically to increase the signal to noise ratio. Another set of coils can be used to apply an external magnetic field, making it possible to measure M-H curves. By measuring minor and major loops, this gives insight into coercive fields, remanence, saturation magnetization, and many more.

Under optimal conditions, the SQUID magnetometer used throughout this thesis (Quantum Design MPMS®3) has a sensitivity of $\leq 10^{-8}$ emu, however, this can only be achieved with a ferromagnet in remanence at zero field. Higher magnetic fields lead to lower sensitivity, mainly due to diamagnetic contributions from the sample holder or substrate. In normal conditions, a sensitivity of $\approx 10^{-6}$ emu is easily achieved, which corresponds to a cubic Fe sample with an edge length of 18 µm or a 30 nm thick Fe film with a surface area of $0.5 \times 0.5\,\mathrm{mm}^2$. This estimate assumes a magnetic moment of $2.19\,\mu_\mathrm{B}$ and a mass density of $7874\,\mathrm{kg/m}^3$.

Measuring the major loop for a sample along different orientations makes it possible to obtain information on its anisotropy. In the simplest case, the uniaxial anisotropy K can be determined by means of the *area method*, where two measurements along the easy and hard direction are performed. The area between the two M-H curves is then calculated, which is equal to the anisotropy energy K [109].

2.6 Transmission Electron Microscopy

A common experimental imaging method with atomic resolution is high resolution transmission electron microscopy (HR-TEM). Figure 2.6 shows

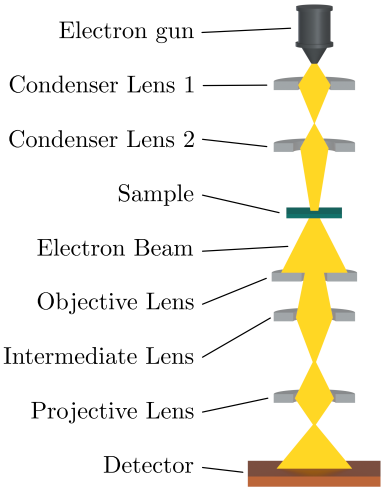

Figure 2.6: Schematic drawing of a transmission electron microscopy (TEM) setup, operated in bright field mode. The electron beam, coming from the electron gun at the top, is directed by a set of apertures and lenses to the sample, and the transmitted electrons to the detector. Some apertures and lenses are grouped together for a better overview.

a schematic sketch of such a device, where highly energetic electrons are generated and accelerated in an electron source with voltages on the order of several hundred kV. This electron beam is then focused on the sample using a system of condensers which act as lenses, as well as several apertures [110]. For this method to work, the sample has to be thin enough to allow for the transmission of electrons. The maximum thickness depends, among others, on the atomic number of the elements involved, as well as the acceleration voltage, and is usually on the order of 100 nm. Lower acceleration voltage and higher atomic number require thinner samples.

TEM devices can be operated in different modes, mainly refraction, bright- and dark field. Depending on the operational mode, different lens systems will be employed behind the sample, before the electrons finally hit a detector. Images are then constructed by spatially resolving the number of

electrons hitting the detector.
In bright field configuration, mainly unscattered electrons reach the detector, meaning that areas with high scattering cross section or high absorption will appear darker.
For dark field images, the unscattered electron beam is blocked by an aperture and thus areas with increased scattering will appear brighter, such as grains, crystal defects, or stacking faults.
Lastly, in diffraction mode, what is obtained is not a real space image of the sample, but instead the diffraction pattern arising from the interference of the electron wave functions. In this mode, a single crystalline sample will show a set of well defined spots, whereas a polycrystalline sample with random orientations will show ring-like structures.

The preparation of suitable TEM samples from a thin film will be discussed in section 2.8.4.

2.7 Energy Dispersive X-ray Spectroscopy

Highly energetic electrons, e.g. in electron microscopy setups, can be used to determine the elemental composition of a sample [110]. Energy dispersive x-ray (EDX) spectroscopy studies the fluorescent light emitted when electrons pass through a material with sufficiently high energy. The photon energy is characteristic for certain electronic transitions and therefore elements, which are denoted according to their principal quantum number n (K, L, M, and so forth) with a Greek letter index representing Δn (α, β, γ, and so forth). For example, an electron transition in iron from $n = 3$ to $n = 1$ would be labeled Fe K_β. An exemplary EDX scan is shown in figure 2.7.

In an EDX measurement, it is necessary to measure the x-ray intensity as a function of energy, oftentimes given in terms of a photon count. The number of photons emitted is proportional to the abundance of a

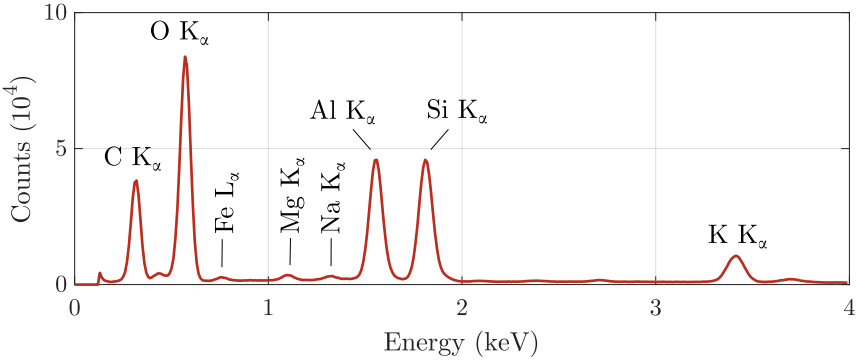

Figure 2.7: Exemplary EDX spectrum of a material containing carbon, oxygen, iron, magnesium, sodium, aluminum, silicon, and potassium, with corresponding labels.

certain element in a material. This enables straightforward qualitative measurement of the elements present in a sample. For quantitative results, evaluation programs use the characteristic x-ray production cross section for each electronic transition, which yields values with an error margin of approximately 3 %[111].

This method can also be used in a spatially resolved manner by scanning over a sample. The spatial resolution in this case is limited by the electrons interaction volume, which in turn is influenced by the penetration depth of the electrons. The penetration depth heavily depends on both the material and the acceleration voltage, but is usually on the order of 1 µm[110]. In the case of a thin TEM lamella, this effect is of course reduced, and spatial resolution is significantly increased compared to scanning electron microscopy (SEM) EDX.

2.8 Sample Preparation Techniques

Many of the physical phenomena studied in this work occur at the nanometer and micrometer scale in thin films of ferromagnetic material. In the following, the techniques for thin film deposition and lithography processes are outlined[34], followed by a description of the process for preparing the TEM samples. Lastly, a method for the exfoliation of 2D materials is introduced.

2.8.1 Thin Film Deposition

Substrates - the starting point for the fabrication of thin films is always a substrate onto which material is deposited. The substrate should be chosen so that the crystal system, as well as the lattice constant, are matching that of the material that is to be deposited. This reduces crystallographic defects and mechanical stress, which could lead to degradation of electrical, optical, or magnonic properties. Sometimes intermediate layers can be introduced to create a transition between different materials, reducing the aforementioned effects. For the $Ni_{80}Fe_{20}$ FMR samples studied in chapter 3, a Si sample was chosen, which is suitable for many metallic, polycrystalline thin films. For the $Ni_{80}Fe_{20}$ samples studied in x-ray transmission in chapter 4, a Si substrate with a silicon nitride (Si_3N_4) membrane window was chosen. The single crystal yttrium iron garnet (YIG) films, on the other hand, were grown on a gadolinium gallium garnet (GGG) substrate. Lastly, the Fe_5GeTe_2 flakes of chapter 5 were also placed on an x-ray transparent Si_3N_4 membrane window substrate. Whenever the thin film needed to be patterned on the µm or even nm scale, a lithography mask is first applied to the substrates using the lithography techniques presented in section 2.8.2. The subsequent thin film deposition techniques can be broadly categorized

by the kinetic energy carried by the atoms and molecules that are being deposited.

$Ni_{80}Fe_{20}$ layers - in this work, to deposit $Ni_{80}Fe_{20}$ layers, a single-crystalline silicon substrate with a Si_3N_4 membrane window was used, onto which the $Ni_{80}Fe_{20}$ layers were deposited using ion beam sputter deposition. For that, the silicon substrate was placed in an evacuated chamber with a $Ni_{80}Fe_{20}$ target, which is hit by a beam of highly energetic ionized Ar atoms from an ion source. When the energy of the Ar ions is transferred to the atoms of the target, they can overcome their bonding energy and move freely inside the evacuated chamber. When they reach the substrate, they condensate, forming a thin film of the desired material. A sketch of the setup can be seen in figure 2.8. The isotropic and highly energetic character of ion beam sputtering deposition makes it difficult to have structures with very sharp edges, and the high penetration depth leads to interface roughness.

Microstrips - in order to fabricate structured samples with sharp edges, as is desired for the microstrips used for the excitation of spin waves, another physical vapor deposition (PVD) method was used, *resistive thermal evaporation*. The system used for this kind of deposition technique is much more simple than the one discussed before. In an evacuated chamber, a small amount of material that is to be deposited is put into an open container, either tungsten or molybdenum, which is heated by running a current through it. When the temperature is high enough, the material will slowly evaporate, and the material will deposit on the substrate, which is suspended on the opposite side of the container. A sketch of this setup can be seen in figure 2.9. Due to the relatively low energies of the atoms, it is possible to have sharp edges even with a thick lithographic mask.

YIG films - the YIG films, on the other hand, were grown on a GGG

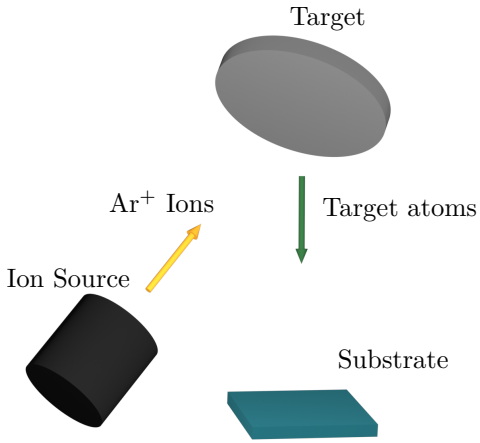

Figure 2.8: Sketch of the setup for the ion beam sputtering. Inside a vacuum chamber, highly energetic ions from an ion source hit a target made from the material that is to be deposited. The ions transfer enough kinetic energy to overcome the target atoms binding energy. The freely moving target atoms condensate inside the chamber and on the substrate, forming a thin layer.

substrate using liquid phase epitaxy (LPE). Although the specific procedure can vary, the general idea is to have a solution with saturated concentration of the material that is to be deposited, and in which the substrate is then submerged [112]. For the right choice of temperature, substrate, solvent, and solute, the thin film will grow layer for layer, with high material purity and crystallographic quality. With this method, it is possible to fabricate YIG films with ultra low damping, which was required for the magnonic analog adder devices studied in the context of this work.

In general, it is much easier to produce polycrystalline, metallic thin films of high quality, such as $Ni_{80}Fe_{20}$. Sputtering methods allow for high deposition rates using a target of the desired material. With YIG, it is much more complicated, and only a handful of companies produce high quality YIG films that are commercially available. For this work, YIG

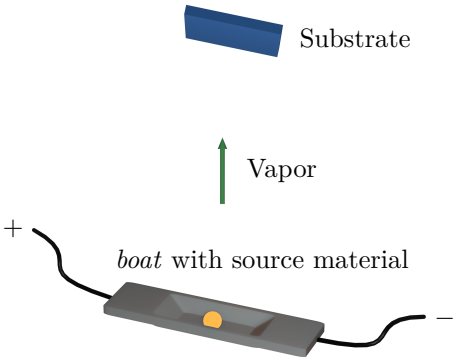

Figure 2.9: Sketch of the setup for the resistive thermal evaporation. Inside a vacuum chamber, the source material is heated up in a *boat* by means of resistive Joule heating until evaporation starts. The vapor fills the chamber and condensates on all surfaces, including the substrate. For better homogeneity, the substrate holder is rotating continuously.

samples were bought from *Innovent Jena*, which have shown to possess a crystalline structure with extremely low damping [113,114].

2.8.2 Lithography

Structuring of a sample can be achieved in different ways, with the best approach mainly determined by the involved length scales. While structures on the mm scale can be easily realized using commercially available marker pens [115], it gets exceedingly more difficult when the µm, or even nm scale is reached [34]. In general, there's two different ways of structuring a sample, either the material is deposited on the entire substrate and subsequently removed at certain points, or the material is only deposited in a certain area. Both these methods rely on some kind of lithographic mask, either a temporary mask made from a so-called *resist*, or a permanent mask that

can be used for multiple lithography processes. While the latter is especially useful in mass production, the former is widely used for prototypical applications, especially in scientific research.

Depending on the requirements, different lithography methods are available. In the context of this work, *optical lithography* using a UV laser, as well as *electron beam lithography* will were used to fabricate samples[35]. In both cases, some kind of resist is applied to the substrate using a spin coating technique, which allows to fabricate a temporary lithography mask. One distinguishes between positive and negative resist. In the case of a positive resist, the area that is exposed to either light or the electron beam will be more readily removed by a solvent after contact with a chemical called the *developer*. In the case of a negative resist, the exposed areas will actually be more resilient, while the rest of the resist is removed by the solvent.

Positive resist is especially useful in so-called *lift-off* procedures, depicted in figure 2.10(a), where in a first step, a system of one or more resists is applied to the substrate. The areas where material should be deposited are then exposed, and the resist is removed using the developer, as well as a solvent. Next, a thin film of material is deposited onto the sample, using the methods described in section 2.8.1. When the leftover resist is now removed using a strong solvent, the deposited material will be removed wherever a layer of resist remained, and only remain in the previously exposed areas.

Negative resists are often used for etching procedures, depicted in figure 2.10(b). In a first step, the material is deposited on the entire substrate, then the negative resist is applied and exposed wherever the material should remain. After the development step, the resist only remains in these previously exposed areas. Now, an etching step is performed, either using *wet etching*, where liquid chemicals are used to etch away the material, or using *dry etching*, where the material is removed by the bombardment with highly energetic ions. The etch rate depends on the material and is usually

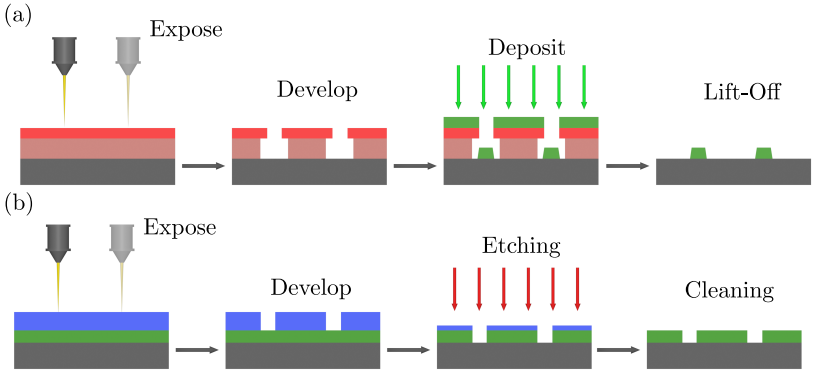

Figure 2.10: Steps of a lithography process using (a) a positive resist (red) with a lift-off technique and (b) a negative resist (blue) with an etching technique. The deposited material is shown in green, the substrate in gray.

much lower for resist than for deposited material and substrate. In a final cleaning step, all residual resist is then removed, leaving material wherever the sample was not previously exposed.

2.8.3 Sample Thinning for Transmission Measurements

The dynamic magnetization measurements performed in transmission geometry require very low sample thickness, so that the attenuation of the x-rays is kept low, giving a good signal-to-noise-ratio. For most samples, this was achieved by using commercially available Si substrates with a micron sized Si_3N_4 membrane and depositing material as described in sections 2.8.1 and 2.8.2. However, some materials require a specific substrate, and so the YIG films could only be grown on GGG substrates, which are not available with a prefabricated membrane window. In order to use these substrates in a transmission experiment, they have to be thinned down to thicknesses on the order of 100 nm. In the case of the GGG substrates, the entire sample

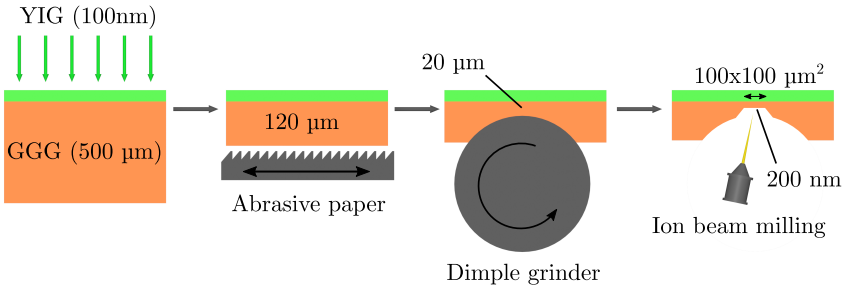

Figure 2.11: Illustration of the different steps during the thinning process of a YIG sample. The initially 500 µm thick GGG substrate (orange) with 100 nm YIG (green) on top, is first thinned down to 120 µm using a fine abrasive paper. Next, a dimple grinder is used to locally reduce the thickness down to 20 µm. Lastly, an x-ray transparent window of approximately $100 \times 100\,\mu m^2$ and 200 nm thickness is created using ion beam milling. Aspect ratio not to scale for a better visibility.

was first thinned to 120 µm using a fine abrasive paper. In a next step, a dimple grinder is used to further thin the center of the substrate down to approximately 20 µm. Then, in a final step, a focused ion beam (FIB) setup was used to uniformly thin an area of approximately $100 \times 100\,\mu m^2$ down to about 200 nm, which is then transparent for x-rays. It is important that the YIG layer is not damaged during the FIB process, since the highly energetic Ga^+ ions can locally alter the magnetic properties of the ferrimagnet, which leads to unforeseeable and irreproducible experimental results.

2.8.4 Lamella Preparation for TEM

TEM measurements were performed on magnetic thin films, in order to investigate their crystallographic structure and elemental composition. For that, small lamellas had to be fabricated with a thickness of only 50-100 nm. This was done using a FIB setup, and the main steps of the procedure are

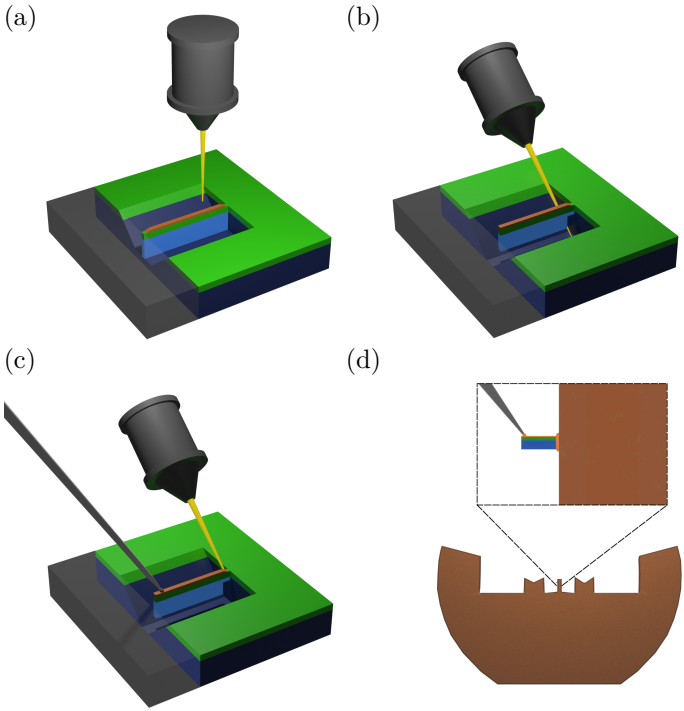

Figure 2.12: Process of cutting a lamella for TEM using a focused ion beam (yellow). (a) Wedge-shaped cut at normal incidence in an area with a protective Pt layer (brown). (b) J-shaped undercut at 52° incidence. (c) Attachment to the micro manipulator needle using a gas injection system. (d) TEM sample holder with the inset showing the attached lamella.

shown schematically in figure 2.12 [116].

First, a protective layer of Pt is deposited locally on the area where the lamella is going to be cut out, approximately 20x20 µm^2 in size. Then, a wedge-shaped cut is made using the focused ion beam at normal incidence, as shown in figure 2.12(a), with a slab of approximately 1 µm width.

This is done so that in a next step, the sample can be tilted with the ion beam at an incidence angle of approximately 52°. This allows to make

a J-shaped undercut, separating the slab from the sample, as shown in figure 2.12(b).
The lamella is then only attached at one point, and in a next step, a micro manipulator is used to bring a needle close to the surface of the slab, which is then attached locally using a gas injection system (GIS) needle, depositing Pt atoms acting as an adhesive. Once the needle is attached, the ion beam is used to cut through the remaining connection. This is also illustrated in figure 2.12(c).
In a last step, the micro manipulator is used to bring the slab close to a TEM sample holder, to which it is attached with Pt from the GIS needle. Once attached, the micro manipulator needle is detached, and the slab, which still has a thickness of approximately 1 µm can be thinned locally using the ion beam. The TEM sample holder, as well as the final result of the TEM lamella preparation is shown in figure 2.12(d).

2.8.5 Mechanical Exfoliation of 2D Materials

One aspect that make van der Waals materials attractive is the fact that it is possible to transfer thin sheets of material from a single crystal to a substrate using mechanical exfoliation [38,117]. These flakes can have atomically flat surfaces due to the fact that coupling between the individual two dimensional layers is weak compared to the molecular bonds within one layer.
Figure 2.13 schematically shows the steps of a mechanical exfoliation process using polydimethylsiloxane (PDMS), a viscoelastic silicon based polymer. First, the single crystal is cleaved using a wafer processing tape, until the crystal surface is visibly shiny. The now exposed, unoxidized surface is then exfoliated using another piece of wafer processing tape, where a variety of different flakes will remain due to the tape's adhesion. During this process, the orientation of the single crystal is kept fixed so that the crystallographic

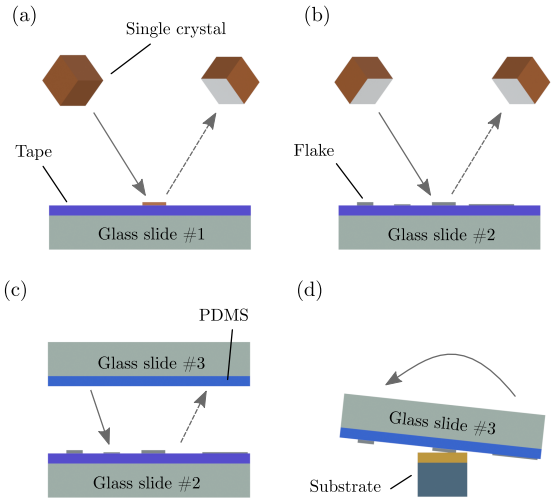

Figure 2.13: Schematic drawing of the mechanical exfoliation procedure. (a) Cleaving of the single crystal, (b) exfoliation of material onto wafer preparation tape, (c) transfer from tape to PDMS stamp, and (d) stamping of the flake onto silicon nitride membrane substrate.

axes of all flakes are aligned.

Next, the wafer processing tape is brought into contact with a PDMS stamp on a glass substrate. With the correct pressure, the flakes will be transferred to the stamp, which are then examined in an optical microscope to measure their lateral size, check their homogeneity, and for a first estimate of their thickness by means of optical contrast. Once a flake with the desired properties has been selected, a stamping setup with an optical microscope and micromanipulators is used to transfer the flake from the curved PDMS stamp to a substrate, in this case a silicon nitride membrane.

In order to stack different materials, this process is repeated, but lack of adhesion between certain materials can make this process very difficult. One important material, which is used both for electrical insulation, as well as protection from oxidation, is hexagonal boron nitride (hBN).

Although it is in principle possible to exfoliate single atomically thin layers, such a sample will quickly be oxidized when the procedure is not performed in a high enough vacuum, e.g. in a glove box. Due to technical limitations, it was therefore only possible to prepare samples with thicknesses on the order of 30 nm. These could be exposed to atmospheric conditions for several minutes before capping them with an hBN layer without compromising their magnetic properties, as was confirmed by their XMCD spectra. In principle, all of the previous steps should be conducted in a glove box without any contact to the atmosphere. This is especially important when stacking of different layers in vdW heterostructure is of interest, since oxidation drastically changes surface properties and therefore proximity effects.

2.9 Sample Preparation of the Analog Adder Devices

In the following, the fabrication procedure of the analog adder devices will be discussed in detail, including all lithography steps, used resist, layer thickness, and so forth.

$Ni_{80}Fe_{20}$ Based Device

The starting point for the $Ni_{80}Fe_{20}$ based device was a commercially available silicon substrate with Si_3N_4 membrane windows. One substrate consists of a 3×3 array of membranes with designated breaking points and an overall size of 10×10 mm^2. Each of the 9 fragments is 2×2 mm^2 in size and the membrane itself has a size of 100×100 µm^2 and a thickness of 200 nm, making it transparent for soft x-rays. Having 9 potential devices

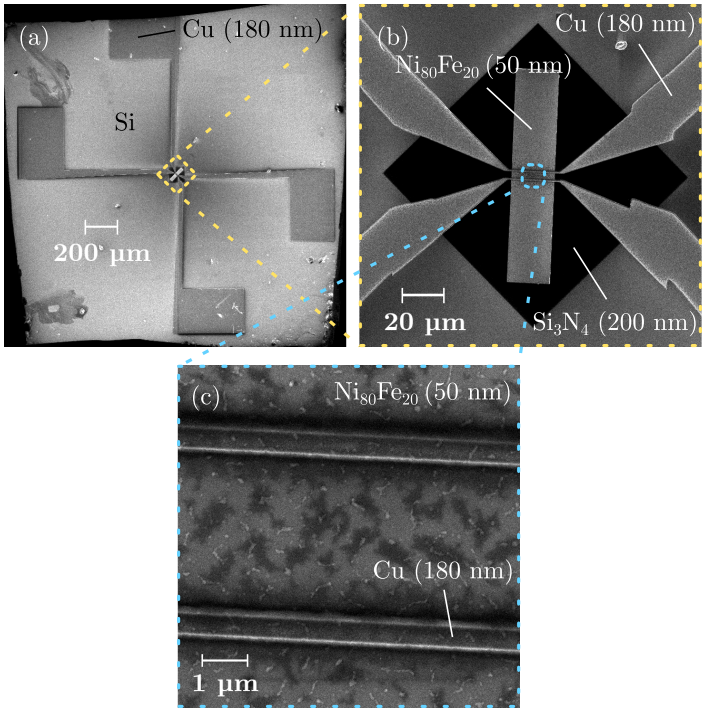

Figure 2.14: SEM images of the $Ni_{80}Fe_{20}$ based adder device with increasing magnification. (a) Sample overview with the four bonding pads and the membrane in the center (b) Si_3N_4 membrane (black) with the rectangular $Ni_{80}Fe_{20}$ waveguide and two microstrips with leads going to the bonding pads (c) Close-up of the two microstrips with visible inhomogeneities.

on one chip significantly reduces the time needed for lithography while also making extensive structure optimization more feasible. Despite its low thickness, the membrane was able to withstand cleaning by spraying with solvents from a bottle, as well as blow drying using nitrogen. It is however not possible to clean them using an ultrasonic bath.

After cleaning the substrate with acetone and isopropyl alcohol for 30 seconds each, they are blow dried using nitrogen gas. A layer of *PMMA*

200K 7% is then spin coated onto the substrate using a wafer dicing tape to protect the membrane from the spin coater vacuum. The sample is then placed on a heat plate at 160 °C for 4 min. A second layer of resist, this time *PMMA 950K 2.5%* is then spin coated using the same parameters, followed by another 4 minute long heat treatment at 160 °C.

The substrate with these two layers of positive resist is then placed in the load lock of the *Raith Eline* electron beam lithography system. In this first lithography step, a 20×100 µm^2 $Ni_{80}Fe_{20}$ waveguide is patterned onto each of the silicon nitride membranes at a dose of 375 µC/cm^2. The dose was determined beforehand in a trial run, where small stripes are patterned in part onto the silicon substrate, and in part onto the silicon nitride membrane. After development, their size is measured and compared to the supposed value. The dose where the measured width is closest to the target width is then chosen. It is important to note that the dose on top of the membrane was approximately 10 % larger due to the fact that some electrons will penetrate the membrane without interacting with the resist. After exposure, the sample is placed in a developer for 60 s and then rinsed with water for 45 s. The result is checked under an optical microscope to ensure that there is no resist left in the areas that were exposed to the electron beam.

The substrate is then put into the vacuum chamber of the ion beam sputtering machine, where 50 nm of $Ni_{80}Fe_{20}$ are deposited first, followed by a 2 nm MgO layer to prevent oxidation, both at a base pressure below 1×10^{-7} mbar.

The lift-off procedure is performed using *N*-Methyl-2-pyrrolidone (NMP) at a temperature of 70 °C. After approximately two hours, the resist with the metal film on top is rinsed away by spraying it with acetone and isopropyl alcohol. If necessary, the substrate can be put into NMP again to get rid of any resist leftovers.

After this lift-off step, another 50 nm layer of MgO is sputtered on top of the entire substrate in order to provide electrical insulation between the

magnetic material and the microstrips, which are patterned next. For the microstrips, the two layers of resist are again spin coated onto the substrate in the same way described before. Using the Raith Eline, two 500 nm wide microstrips with a 4 µm gap are patterned on top of the previously sputtered $Ni_{80}Fe_{20}$ waveguides. Larger bonding pads are patterned away from the membrane in order to be able to electrically contact the sample. After development, the samples are put into a Leybold UNIVEX thermal evaporation chamber, where a layer system of Cr(8 nm)/Cu(180 nm)/Cr(8 nm) is then deposited for the microstrips and bonding pads.
Another lift-off procedure is performed in order to finalize the sample. All this was done on the 3 by 3 membrane array, meaning this procedure yields up to 9 devices. However, due to problems such as stitching errors or contamination of the sample, usually some of the devices are not usable. The electrical conductivity of the microstrips is checked using a *Keithley 2450* sourcemeter that limits both applied voltage and maximum current in order to protect the microstrips from being destroyed. The sample is contacted using two probe needles attached to micro manipulators.

Samples with low resistance (on the order of 100 Ω) are then glued onto a sample holder that is suited for the STXM measurements at the x-ray microscope MAXYMUS. Scanning electron microscopy images of a finalized sample at different magnifications can be seen in figure 2.14. The shown sample has not been electrically contacted yet, so the bonding pads are still pristine. Slight misalignment, which does not impair device functionality, can be seen at intermediate magnification. The inhomogeneities seen at highest magnification are not magnetic in nature since they were not visible in the STXM difference images. It is possible that some residual resist is left from the lift-off process of the microstrips.

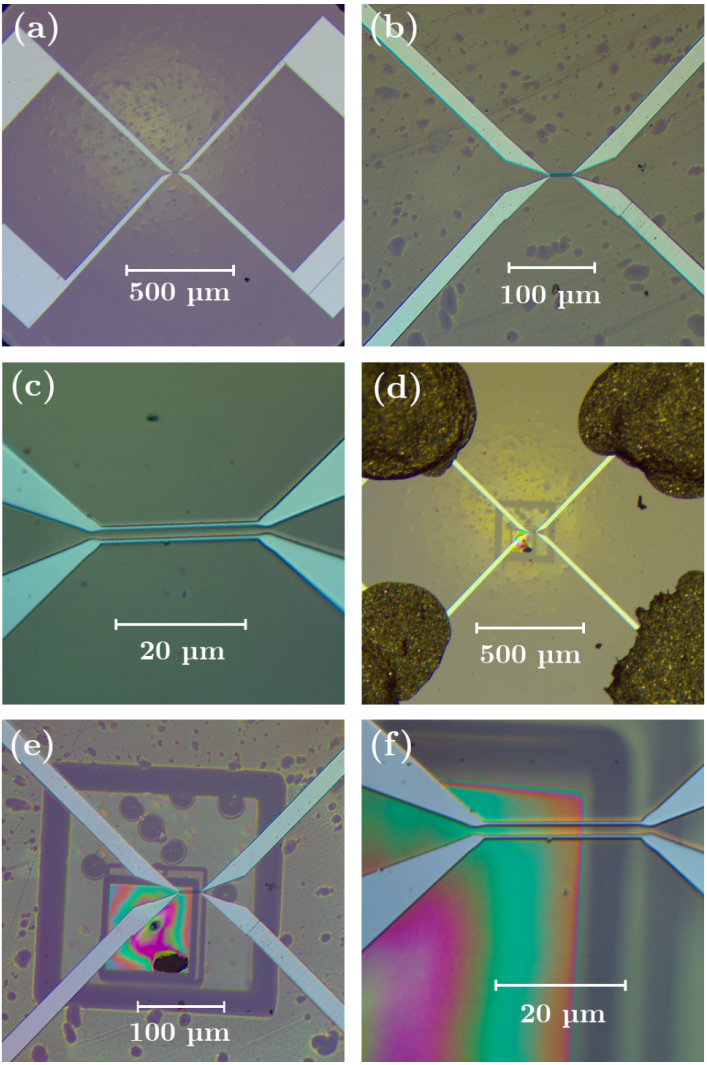

Figure 2.15: Optical micrographs of the YIG based adder device before (a-c) and after (d-e) focused ion beam milling with increasing magnification. The microstrip antennas can be seen ad the center of the device, with larger contact pads at the edges to establish electrical contact.

YIG Based Device

The starting point for the YIG based device was a commercially available YIG film of 100 nm thickness on top of a GGG substrate, grown by LPE, as introduced in section 2.8.1.

A substrate of this kind was first cut into 10×10 mm^2 pieces, which were cleaned in acetone and isopropyl alcohol using an ultrasonic bath. For the cutting process, it is necessary to first apply a protective layer of resist so that the substrate surface is not contaminated by the small particles flying around. This layer is then removed in the aforementioned ultrasonic bath. The 10×10 mm^2 pieces are then coated with the same resist layers as the Si substrates for the $Ni_{80}Fe_{20}$ samples. First, *PMMA 200K 7%* and then a layer of *PMMA 950K 2.5%*. However, due to the insulating properties of YIG, an additional layer is needed, namely an *Espacer* containing conductive polymers to prevent charging effects during electron beam lithography, and it is applied by spin coating at 4000 RPM for 60 s.

Unlike the $Ni_{80}Fe_{20}$ samples, the YIG samples can not be structured by lift-off techniques. There have been attempts to sputter YIG, however, the homogeneity and low damping of samples grown by LPE can not be reached yet [83]. Attempts to structure YIG by etching a prefabricated film have also proven to be difficult on the µm scale. The etching process would locally change the properties of YIG at the edges, introducing inhomogeneities and undesired effects on spin-wave propagation [83].

The entire YIG film is used as the spin-wave propagation medium, and only the microstrips are added. This is done in the *Raith Eline*, where two 500 nm wide microstrips with a 2 µm gap, as well as larger bonding pads for electrical contacting are defined and patterned with a dose of 250 µC/cm^2. This is done for a 3×3 array on the 10×10 mm^2 substrate, each structure approximately 2.5×2.5 mm^2 in size and a 1.25 mm margin on each side. The sample is rinsed in deionized water for 60 s and then put into a developer for 60 s and rinsed in water for 45 s, and the result is checked under an

optical microscope.
Next, to realize the microstrips, a stack of Cr(8 nm)/Cu(180 nm)/Cr(8 nm) is deposited on the substrate again using the Leybold UNIVEX thermal evaporation chamber with a subsequent lift-off procedure using NMP at 70 °C
After applying a protective layer of resist, the sample is cut into 2×2 mm^2 pieces which are then thinned down individually. This is necessary to make them transparent enough for x-rays, which is needed for the STXM measurements. The procedure for this was introduced in section 2.8.3, and was done here with a first thinning step down to 120 µm, then locally down to 20 µm, and lastly down to 200 nm using FIB. After the first two steps, the sample is already glued onto the final sample holder, which also fits into the FIB setup. A layer of carbon is deposited onto the backside to reduce charging effects during the focused ion beam milling, similar to the *Espacer* used during electron beam lithography. The transparent window cut with FIB is approximately 100×100 µm^2 in size.

Figure 2.15 shows optical micrographs of a YIG based adder device before and after focused ion beam milling with increasing magnification. Some inhomogeneities are visible in the intermediate magnification, which are thought to exist in the GGG layer. By comparing figure 2.15(b) and (e), one can see that these areas are visible as black dots once the FIB milling is done. The STXM images later on, however, will show that the YIG layer and therefore spin-wave propagation is not heavily affected by this. In Fig 2.15(d), the sample is already electrically contacted using conductive silver to connect the bonding pads with the leads on the sample holder. The highest magnification of the finished sample (f) shows that a very homogeneous area surrounds the two microstrips, as indicated by the color gradient.

2.10 Simulations

The most common way to simulate magnetic systems at length scales where the atomic structure is negligible, is by applying micromagnetic theory. This continuum approach incorporates the energy contributions from the different magnetic interactions, some discussed in section 1.1.2, into a total magnetic energy

$$E = E_{\mathrm{z}} + E_{\mathrm{s}} + E_{\mathrm{a}} + E_{\mathrm{ex}} + ..., \tag{2.13}$$

where E_{z}, E_{s}, E_{a} and E_{ex} are the energy contributions from the Zeeman effect, the stray field, anisotropy, and exchange interaction, respectively. Depending on the systems, other interactions can contribute to the total energy, while others might not be of significance.
The general approach of micromagnetic theory is to minimize the total energy with respect to the magnetization $\mathbf{M}$ of the system.
If the dynamic behavior of a system is of interest, the Landau-Lifshitz-Gilbert equation (Equation (1.19)) is used to describe how $\mathbf{M}$ changes over time, as was introduced in section 1.2.1. This approach is used by freely available micromagnetic simulation software such as *OOMMF* [118] or *MuMax3* [119], where a system is discretized into a grid for which the temporal evolution of $\mathbf{M}$ is calculated.

In the context of this work, however, a different approach for modeling the layered two-dimensional materials in chapter 5 was chosen. It is based on the dynamic matrix method, where instead of numerically solving the LLG equation, the problem is formulated in terms of an eigenvalue equation [55]

$$i\omega\mathbf{m}(\mathbf{r}) = \gamma\mu_0\tilde{\mathbf{A}}\mathbf{m}(\mathbf{r}), \tag{2.14}$$

where i denotes the imaginary unit, ω the angular frequency, γ the gyromagnetic ratio, μ_0 the vacuum permeability, and $\tilde{\mathbf{A}}$ the so-called dynamic matrix. This approach is able to calculate spin-wave dynamics in an ex-

tended film much more efficiently than the conventional method used by *OOMMF* and *MuMax3* [55]. It is particularly suited for calculating the dispersion relation and spin-wave mode profiles of multilayered systems, such van der Waals materials. While intralayer coupling is strong in these materials, the interaction between individual layers can be modeled using an interlayer coupling energy, as well as dipolar contributions.
To that end, the magnetization can be written as

$$i(\omega/\gamma\mu_0)m_{x_n}(\mathbf{r}) = -m_{y_n}(\mathbf{r})H^{\mathrm{e}}_{z_n} + M_{s_n}h^{\mathrm{e}}_{y_n}(\mathbf{r}), \tag{2.15}$$

$$i(\omega/\gamma\mu_0)m_{y_n}(\mathbf{r}) = m_{x_n}(\mathbf{r})H^{\mathrm{e}}_{z_n} - M_{s_n}h^{\mathrm{e}}_{x_n}(\mathbf{r}), \tag{2.16}$$

where m_{x_n} and m_{y_n} denote the x- and z-components of the magnetization in the nth layer, H^{e} the static and h^{e} the dynamic part of the effective field. Here, x is parallel to the spin-wave wavevector $\mathbf{k}$, and z points along the thin film normal. The dynamic part of the effective field has to include contributions from all sublayers, since dipolar interactions are long-range and have to be taken into account here. Using the matrix formulation from equation (2.14), the transpose of the eigenvector $\mathbf{m}(\mathbf{r})$ can be written as

$$\mathbf{m}^{\mathrm{T}}(\mathbf{r}) = [m_{x_1}(\mathbf{r}), m_{y_1}(\mathbf{r}), m_{x_2}(\mathbf{r}), m_{y_2}(\mathbf{r}), ..., m_{x_N}(\mathbf{r}), m_{y_N}(\mathbf{r})]. \tag{2.17}$$

The key is now to compile the dynamic matrix $\tilde{\mathbf{A}}$, as well as the effective field, which can be done by considering the different magnetic interactions, as was done in section 1.1.2. In addition to the contributions discussed there, an extra term is added to account for the exchange interaction arising between layers, which is much weaker than the intralayer exchange interaction due to the larger distances involved. The different matrix elements and how they are derived can be found in reference [55].

For the calculation of the dispersion relation of such a multilayer system, the following parameters are required: Uniaxial anisotropy constant K_{u}, saturation magnetization M_{s}, exchange stiffness A_{ex}, total thickness, number of layers, gap width, and interlayer coupling strength J_{inter}.

Part III

Results

3 | Gilbert Damping in Annealed Permalloy Thin Films

In recent years, wave-based computing using spin waves has been discussed as a possible avenue for technologies beside the conventional complementary metal oxide semiconductor (CMOS) approach. Utilizing both amplitude and phase of the spin waves opens up new possibilities for conceiving and designing new devices without the drawback of heat production caused by moving electrons [8–10,120]. This might give magnonics, the field of study that is concerned with using spin waves as potential information carriers, an edge over CMOS technologies for certain machine learning and neuromorphic computing applications [26,121]. This approach relies on materials that allow for spin-wave propagation on length scales comparable to the device size, and therefore a low Gilbert damping parameter. A low damping system is metallic Permalloy (Py) [81,122,123], a magnetic nickel-iron alloy, which can be readily grown on Si substrates using relatively simple methods such as thermal evaporation, ion beam- and magnetron sputtering [124,125].

While the spin waves themselves do not cause Joule heating while propagating, the excitation mechanism oftentimes require very high current densities, usually on the order of $1 \times 10^{10}\,\mathrm{A/m^2}$ to $5 \times 10^{11}\,\mathrm{A/m^2}$, resulting in significant local heating [4]. This can in turn alter material properties,

with detrimental effects for device functionality. The effect of vacuum annealing on $Ni_{80}Fe_{20}$ thin films has gotten little attention in literature, albeit being very important for device conception and fabrication. Previously, the structure of Ni films grown on Si have been studied as a function of temperature [126], where a formation of nickel silicides at temperatures above 350 °C was observed. This is well below the eutectic temperature of the system [127], and the experimental evidence suggested that Ni was the major moving species during the nickel silicide growth. A systematic study of the effect of elemental composition on the magnetic properties in $3d$ transition-metal binary alloy thin films has also been conducted [71,128], however, a link between temperature induced structural changes and magnetic properties has not been established yet.

In the following, the experimental results of studying the Gilbert damping parameter as a function of annealing temperature will be discussed. To that end, samples annealed at different temperatures up to 350 °C are studied by means of ferromagnetic resonance (FMR) measurements, combined with high resolution transmission electron microscopy (HR-TEM) and energy dispersive x-ray spectroscopy (EDX) to investigate their crystallographic structure and elemental composition. Using these results, a connection between magnonic properties and structural changes could be established.

3.1 Sample Design and Preparation

To ensure coherent results that allow for the direct comparison of different samples, a single $10 \times 10\,\mathrm{mm}^2$ Si substrate was covered with 36 nm of $Ni_{80}Fe_{20}$ by means of ion beam sputtering using an Ar source at a base pressure of 3.9×10^{-7} mbar and a working pressure of 1.53×10^{-4} mbar. After deposition, the sample was cut into four pieces, each $5 \times 5\,\mathrm{mm}^2$ in size.

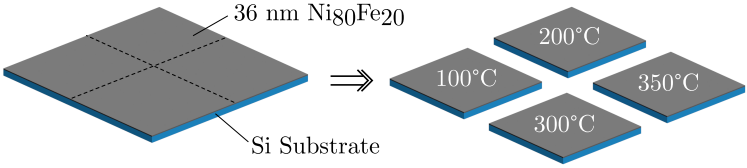

Figure 3.1: Schematic illustration of the sample design for the investigation of the effect of vacuum annealing on the structure and magnonic properties of $Ni_{80}Fe_{20}$.

These were then individually annealed in a vacuum furnace at a pressure below 4×10^{-7} mbar at $T_a = 100$, 200, 300, and 350 °C respectively. A sketch of the basic sample design is shown in figure 3.1.

The samples were then contacted electrically and connected to a vector network analyzer (VNA) to perform VNA-FMR measurements.
For the structural analysis, a TEM lamella was cut out of each sample before and after annealing, according to the procedure described in section 2.8.4. These samples were then studied using a Philips CM-200 FEG TEM operated at an acceleration voltage of 200 kV, combined with complementary EDX analysis, as introduced in sections 2.6 and 2.7 respectively.

3.2 FMR Measurements

The FMR measurements were performed using a vector network analyzer (VNA-FMR), as introduced in section 2.4, by varying the magnetic field for fixed excitation frequencies between 2 GHz and 25 GHz. The range of the magnetic field sweep was chosen so that the resonance was well visible. These FMR measurements have been carried out before and after annealing, meaning that four datasets before annealing were obtained, and one for each temperature after annealing. The dataset before annealing will be

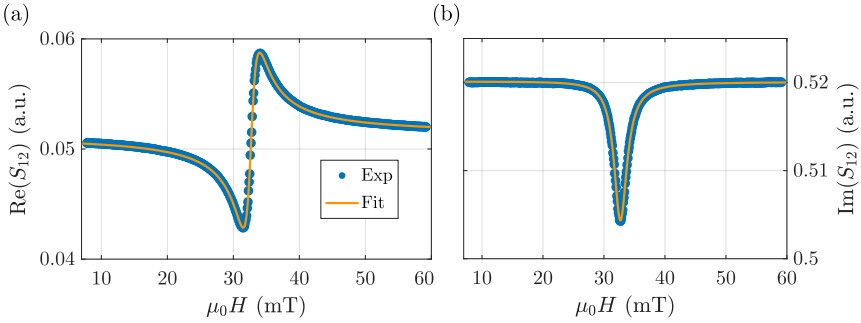

Figure 3.2: Exemplary FMR data of the unannealed sample with the experimental data points, together with a fit function, measured at a frequency of 5 GHz. (a) Real and (b) imaginary part of the S_{12} parameter together with Lorentzian fit. One set of parameters was used to fit both real and imaginary part of the scattering parameter.

labeled $T_a = 20\,°C$.

An exemplary measurement of the real and imaginary part of S_{12} is shown in figure 3.2. The experimental data is modeled using a sum of symmetrical and asymmetrical Lorentz functions

$$S \cdot \frac{\Delta H^2}{\Delta H^2 + (H - H_{res}^2)} + A \cdot \frac{\Delta H (H - H_{res})}{\Delta H^2 + (H - H_{res}^2)}, \tag{3.1}$$

with the prefactors S and A, the resonance field H_{res} and the half width half maximum of the absorption line ΔH [104]. From this fit, the resonance field and linewidth can be extracted and used to determine the Gilbert damping α, the effective magnetization M_{eff}, and the g-factor according to equation (2.8) and (2.12).

Figure 3.3 shows the relationship between excitation frequency f and resonance field H_{res}, which can be described by equation (2.8), the Kittel formula [48,103]. It is shown exemplary for two different annealing temperatures, namely 20 °C and 300 °C. It can be seen that the two samples show slightly different behavior, with the sample annealed at 300 °C showing a

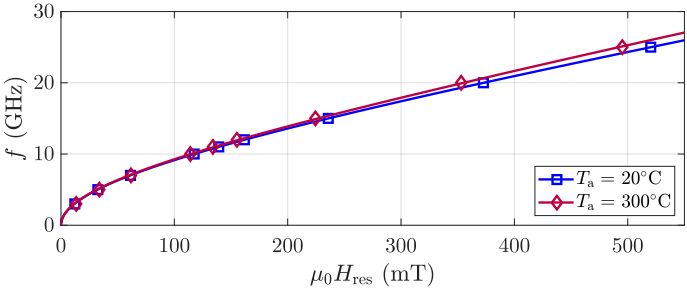

Figure 3.3: Resonance field H_{res} as a function of frequency f, as obtained from the Lorentzian fit to S_{12} for two annealing temperatures, 20 °C (blue squares) and 300 °C (red diamonds). The line represents a fit using the Kittel formula to extract the gyromagnetic ratio and the effective magnetization.

greater slope towards higher fields. While not shown here, the measurements between 20 °C and 200 °C do not show any significant difference. By fitting the Kittel formula to the experimental data, it is possible to extract M_{eff}, as well as the g-factor of the sample. This was done for the four unannealed samples, as well as all annealed samples, and the results are plotted in figure 3.4. Figure. 3.4(a) shows the g-factor as a function of annealing temperature T_{a}, and it can be seen that up to a temperature of 200 °C, g stays at a value of approximately 2.11, in accordance with literature values for $Ni_{80}Fe_{20}$ [128]. When further increasing the temperature, g increases to a value of approximately 2.32 ± 0.12 for $T_{\mathrm{a}} = 300\,°\mathrm{C}$ and even to 2.36 ± 0.12 at $T_{\mathrm{a}} = 350\,°\mathrm{C}$. The increasing error is a result of the fit using the Kittel formula, which is not able to accurately describe the shape of the curve at higher annealing temperatures.

A similar trend can be observed for the effective magnetization M_{eff}, where a steady value of (852 ± 10) mT is observed up to annealing temperatures of 200 °C. When T_{a} is further increased, M_{eff} will decrease by a factor of 0.84 down to a value of (716 ± 97) mT for $T_{\mathrm{a}} = 300\,°\mathrm{C}$ and to (621 ± 87) mT for $T_{\mathrm{a}} = 350\,°\mathrm{C}$. The magnetization is therefore decreased by a factor of

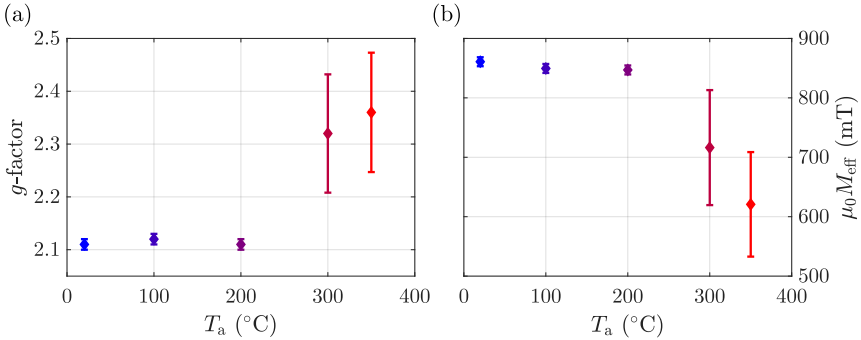

Figure 3.4: (a) g-factor and (b) effective magnetization as a function of annealing temperature T_a, obtained using the Kittel formula. Color indicates temperature, error bars according to the fitting error (adapted from [129]).

0.73 when the sample is annealed at 350 °C, while the g-factor increased by a factor of 1.12. For both these values, the error margin increases significantly for higher annealing temperatures, owing to the linewidth broadening which results in more uncertainty of the resonance position. This linewidth broadening can be used to obtain information on dissipation mechanisms, such as the Gilbert damping.

Equation (2.12) can be used to determine the Gilbert damping parameter α from the measurement of the resonance linewidth ΔH as a function of excitation frequency f, which is shown in figure 3.5(a). Again, the data for the unannealed sample overlaps with that of the samples annealed at 100 °C and 200 °C. It shows linear behavior over the whole frequency range, and from its slope α can be determined.

At an annealing temperature of 300 °C, the data points show clear deviation from the liner behavior. Similar nonlinearities have been observed in magnetic thin films where extrinsic contributions to the FMR signal were studied, a topic closely related to the two-magnon model of scattering[130–133]. The same is true for the measurements at $T_a = 350$ °C, and it

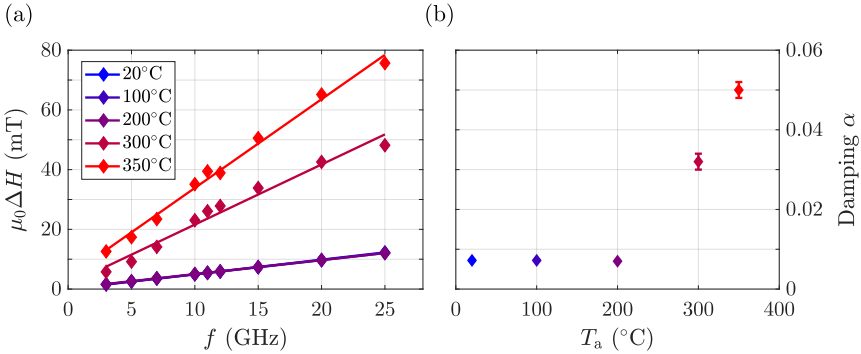

Figure 3.5: Determination of α from the FMR data. (a) FMR linewidth as a function of frequency for different annealing temperatures and (b) Gilbert damping parameter α as a function of annealing temperature T_a. Measurements with $T_a = 20\,°C, 100\,°C$, and $200\,°C$ are indistinguishable and overlap in (a). Adapted from [129].

is striking that the deviation from the linear behavior is almost identical for both 300 °C and 350 °C. The two measurements only differ by the slope of their linear background, indicating that the mechanism for the nonlinearities is the same in both cases.

Figure. 3.5(b) shows the Gilbert damping parameter α as a function of annealing temperature T_a, as obtained from the data shown in figure 3.5(a). It can be seen that again, no significant change is observed at temperatures up to 200 °C, with a steady value of $\alpha = (7.2 \pm 0.1) \times 10^{-3}$, again in accordance with literature [71] . A further increase of T_a leads to an increase of the Gilbert damping to a value of $(32 \pm 2) \times 10^{-3}$ for $T_a = 300\,°C$, up to a more than sixfold increase to $(50 \pm 2) \times 10^{-3}$ for $T_a = 350\,°C$.

Overall, the FMR measurements indicate that the samples undergo significant changes when annealed at temperatures of 300 °C and above. To investigate the nature of this transition, a structural analysis using TEM and EDX was conducted.

3.3 Structural Analysis

Figure 3.6 shows composite images of the samples annealed at different temperatures. The unannealed sample was indistinguishable from the one annealed at 100 °C, which is why it was omitted here. On the left side, the bright field images are shown, with material and structural contrast, as introduced in section 2.6. At the center, a spatially resolved EDX map is shown, with the colors indicating the elements Si (green), Ni (blue), Fe (yellow), and Pt (red). This EDX map is used to determine a cross section of the elemental composition, which is shown on the right, given in terms of atomic percent. The spatial resolution of the EDX map is however not sufficient to distinguish individual grains, so the color distribution in the EDX map only indicates the presence of a certain element, not its exact local density. Inhomogeneities on these length scales can therefore not be studied using the EDX data.

In figure 3.6(a), the sample annealed at 100 °C is presented. The bright field image shows three distinct phases with small transitional regions in between, resulting from a slight sample tilt and the finite sample thickness. From the bright field image, the thickness of the Ni-Fe layer could be determined to be (36 ± 1) nm. The EDX map reveals that these three regions, from top to bottom, correspond to Pt, Ni-Fe, and Si. The Pt layer is a remnant from the sample preparation procedure, as introduced in section 2.8.4. The cross section shows that the Ni-Fe layer consists of approximately 75 % Ni and 20 % Fe. For better statistics, instead of using the cross section, the EDX map was averaged over large areas of each phase, which yielded a value of 71 % Ni, 22 % Fe, 6 % Si, and 1 % Pt for the Ni-Fe layer. The relatively large Si signal arises from scattering of electrons into the adjacent Si layer, an effect that is also responsible for the large Si signal within the Pt layer.

The sample annealed at 200 °C can be seen in figure 3.6(b). The bright

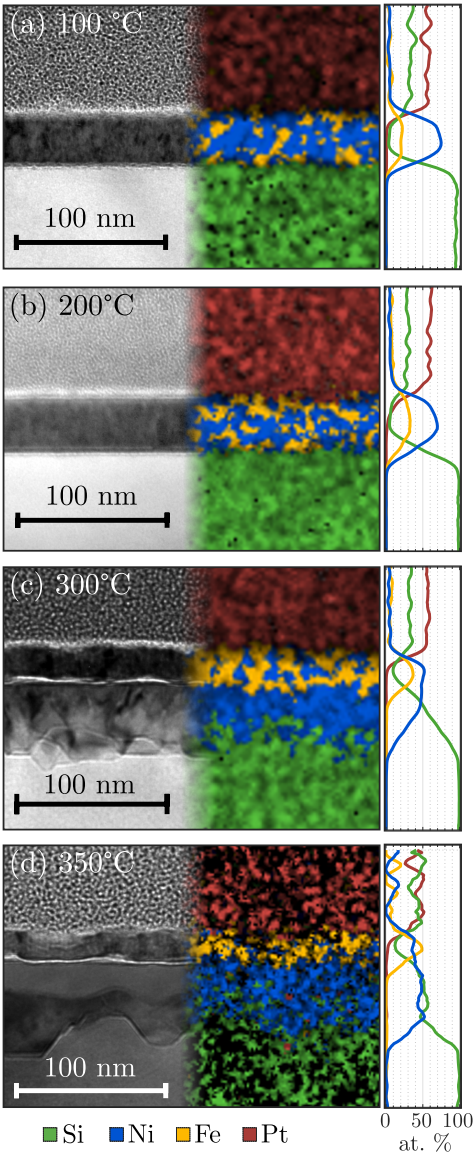

Figure 3.6: TEM bright field images, together with EDX maps and corresponding cross sections for different annealing temperatures, (a) 100 °C, (b) 200 °C, (c) 300 °C, and (d) 350 °C. Colors representing the elements Si (green), Ni (blue), Fe (yellow), and Pt (red). Adapted from [129].

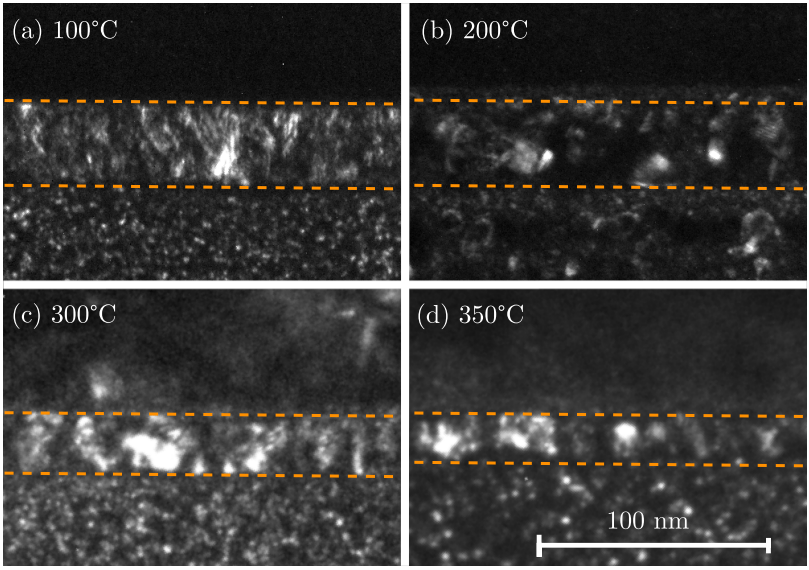

Figure 3.7: TEM dark field images for different annealing temperatures, (a) 100 °C, (b) 200 °C, (c) 300 °C , and (d) 350 °C. The orange dashed line marks the boundaries of the Ni-Fe layer (adapted from [129]).

field image looks slightly different from the previous one with regards to contrast and brightness due to different operating conditions of the electron microscope and the thickness of the lamella. The same is true for the EDX maps, which show the same general features, with three clearly separated layers of Pt, Ni-Fe, and Si. The transitions regions are more pronounced, which indicates that the sample tilt was larger than in figure 3.6(a). The Ni-Fe layer is again measured to be (36 ± 1) nm thick. When averaging over the Ni-Fe layer, an elemental composition of 69 % Ni, 22 % Fe, 11 % Si, and 1 % Pt was obtained. The slight deviation compared to the sample annealed at 100 °C is within the error margin of the EDX measurements.

Figure 3.6(c) shows the sample annealed at 300 °C, with several striking features. The bright field image shows a fourth phase that has emerged between the Ni-Fe layer and the Si substrate. The EDX analysis reveals

that this newly formed phase consists of Si and Ni atoms, in accordance with a previous study where the formation of nickel silicides was observed in a similar system at comparable temperatures [126]. Ni atoms have moved from the Ni-Fe layer into the Si substrate, leaving behind a Ni-Fe layer with decreased Ni concentration. This is also confirmed by the EDX cross section, and by averaging over the Ni-Fe layer an elemental composition of 52 % Ni, 36 % Fe, 11 % Si, and 1 % Pt is found. The newly formed Ni-Si layer is found to contain 47 % Ni, 3 % Fe, 50 % Si, and 0 % Pt with a thickness ranging from 29 nm to 53 nm. Despite this massive structural change, the Ni-Fe layer is clearly separated from the Ni-Si layer, with no transitional region in between. While the Ni atoms migrated into the Si layer, Fe atoms had to move in the opposite direction, since the resulting Ni-Fe layer has clearly decreased in size down to a value of (24 ± 2) nm.

In figure 3.6(d), the sample annealed at 350 °C is shown, where the same features observed at $T_a = 300$ °C are visible, only with larger magnitude. The different appearance of the bright field image can be attributed to different measurement parameters and lamella thickness.
Again, Ni atoms have migrated from the Ni-Fe layer into the Si substrate forming nickel silicides, leaving behind a Ni-Fe layer with decreased Ni concentration and a thickness of only (20 ± 3) nm. The composition of the Ni-Fe layer was determined to be 38 % Ni, 38 % Fe, 24 % Si, and 0 % Pt. The Ni-Si layer was determined to contain 55 % Ni, 1 % Fe, 44 % Si, and 0 % Pt with a thickness ranging from 35 nm to 61 nm. However, the large fluctuations in the EDX cross section, as well as the dark spots in the EDX map indicate that the signal to noise ratio of this measurement was much lower compared to the previous measurements, which makes the determined values for the elemental composition less reliable.
The migration of different atomic species will inevitably result in a change of the crystallographic order. A hint of this can already be seen in the bright field images, where a decreased homogeneity of the Ni-Fe layer for annealing temperatures of 300 °C and above is observed.

To confirm this, additional TEM measurements in dark field configuration were performed, as shown in figure 3.7 for annealing temperatures of $T_a = 100\,°C$, $200\,°C$, $300\,°C$, and $350\,°C$. The microscopy images of the unannealed sample are again omitted since they are indistinguishable from the ones of the sample annealed at $100\,°C$.
The decrease of the Ni-Fe layer thickness for higher annealing temperatures is again clearly visible, with thicknesses of 35 nm, 35 nm, 25 nm, and 20 nm for $T_a = 100\,°C$, $200\,°C$, $300\,°C$, and $350\,°C$ respectively.
Individual grains are visible at all temperatures, however, their size increase considerably at annealing temperatures of $300\,°C$ and above. Additionally, due to the decreasing thickness of the Ni-Fe layer, the grain size becomes comparable to the Ni-Fe layer thickness at high annealing temperatures.

3.4 Discussion

The presented results obtained from the FMR measurements and the structural analysis using TEM and EDX demonstrate that $Ni_{80}Fe_{20}$ thin films undergo irreversible changes when exposed to excessive temperatures. This means that in magnonic devices based on $Ni_{80}Fe_{20}$, Joule heating could lead to detrimental effects on the magnonic properties of the device and impair its functionality. Combining the results from these two different approaches, a link between the change in magnetic properties and the structural changes can be established.

Table 3.1 gives an overview over the different parameters that were determined for varying annealing temperature. The decrease of the effective magnetization M_{eff} by up to 27 %, as well as the increase of g by 12 % and the sixfold increase of the Gilbert damping parameter α correlate with the migration of Ni atoms from the Ni-Fe layer into the Si substrate and

Table 3.1: Overview over g-factor, effective magnetization M_{eff}, Gilbert damping parameter α, and thicknesses of the NiFe and NiSi layer t_{NiFe} and t_{NiSi} for different annealing temperatures T_{a}.

T_{a}(°C)	100	200	300	350
g	2.12±0.01	2.11±0.01	2.32±0.12	2.36±0.12
$\mu_0 M_{\mathrm{eff}}$ (mT)	849±8	847±8	716±97	621±87
α (10^{-3})	7.2 ± 0.1	7.0 ± 0.1	32 ± 2	50 ± 2
t_{NiFe} (nm)	36±1	36±1	24±2	20±3
t_{NiSi} (nm)	-	-	41±12	48 ±13

the simultaneous increase of Fe content in the Ni-Fe layer. Both bright and dark field images showed a reduction of the Ni-Fe layer thickness from 36 nm to 25 nm at temperatures of 300 °C and 20 nm at 350 °C, while grain size increased.

Earlier works by Julies *et al.* could show that for a system consisting of a Ni thin film grown on a Si substrate, Ni atoms readily move into the Si substrate at temperatures above 200 °C[126]. It was shown that nickel silicides are formed in the process, with Ni_2Si forming at temperatures above 200 °C, and NiSi at temperatures of 350 °C. This behavior can also be observed in the present measurements by TEM and EDX.
In principle, the newly formed Ni-Si layer could magnetically interact with the Ni-Fe layer, affecting the damping parameter, however, it has been shown that Ni-Si compounds are almost exclusively non-magnetic, making this scenario highly unlikely[134,135].

The observed thickness decrease of the NiFe layer was accompanied by an increase of Fe content. Naively, one could expect this to increase the magnetization of the NiFe layer due to the higher magnetic moment of Fe compared to Ni[71,128]. However, a decrease of M_{eff} was observed in the FMR experiments. This could be caused by an increase of the anisotropy

constant K_u, which in turn would decrease M_{eff} according to $M_{eff} = M_s - 2K_u/M_s$ [104]. The dark field images on the other hand have shown that despite the relatively low annealing temperature, grain formation occurred, significantly reducing the homogeneity of the sample. This results in more non-magnetic areas compared to the initial polycrystalline $Ni_{80}Fe_{20}$ layer, thereby reducing M_{eff}.

The observed inhomogeneities will also affect the damping of the system by amplifying extrinsic contributions to the Gilbert damping parameter α, an effect that will be particularly strong when the magnon wavelength is comparable to the grain size.

Different models can be used to describe the magnon energy dissipation in systems with inhomogeneities such as grains. Depending on the relative size of the grains compared to the film thickness, either the two-magnon model or the local resonance model can be employed. These models include the local variation of the anisotropy fields in inhomogeneous thin films with grains and have shown to reproduce the non-linear behavior of the FMR linewidth as a function of frequency that was observed in figure 3.5(a) [130–133,136]. However, associating the observed effects with individual dissipation channels is not feasible, due to the diversity of the mechanisms involved, as was also discussed in 1.2.2.

3.5 Conclusion

Overall, FMR measurements showed a more than sixfold increase of the Gilbert damping parameter in 36 nm thin $Ni_{80}Fe_{20}$ films grown on Si at annealing temperatures above 300 °C. This was accompanied by a 12 % increase of g and a 27 % decrease of the effective magnetization. Utilizing TEM and EDX analysis, this could be linked to the migration of Ni atoms out of the Ni-Fe layer into the Si substrate forming nickel silicides, and

the simultaneous movement of Fe atoms into the Ni-Fe layer, resulting in a Ni-Fe layer with only 57 % of the original thickness and a significantly decreased amount of Ni. The newly formed Ni-Si layer was determined to have a thickness of up to 61 nm with a clear boundary towards the Ni-Fe layer.

Grain formation was observed as a result of the movement of Ni and Fe atoms well below the eutectic temperature of the system, which could be linked to the change in α in terms of the two-magnon scattering induced viscous Gilbert damping.

The results therefore demonstrate that $Ni_{80}Fe_{20}$ thin films can undergo irreversible structural changes when exposed to excessive temperatures over long periods of time. The associated effects on the magnetic properties can have a fatal impact on magnonic devices and have to be considered when designing them.

This seemingly unfavorable effect could however be exploited by being able to locally change the magnetization and damping of a sample, which could find applications in the fabrication of magnonic crystals [25] or to induce a damping gradient to reduce unwanted reflections.

4 | Realization of a Magnonic Analog Adder with Frequency Division Multiplexing

For certain computational problems, the binary approach does not represent the optimal solution with regards to speed and energy efficiency. One example is machine learning, where some recent approaches have shifted their focus towards alternative computing schemes, which are more suitable for the kinds of operations that need to be performed in e.g. neural networks[137–140]. One possible avenue is analog computing, which utilizes the continuous nature of a physical quantity to perform computations or model other systems. Electrical[141,142], acoustic[143], and optical[144] methods have been considered for practical implementations.

Magnonics as the overarching topic of this thesis aims to use coherent spin waves for information processing[10,11]. Due to the lack of charge transport, energy losses arising from Joule heating are thought to be minimized, while also enabling wave-based computing. The dispersion relation of magnons, which gives rise to submicrometer wavelengths at frequencies typically

between 100 MHz and 10 GHz provide an excellent match for the length and time scales of modern nanoscale devices. Most effort in magnonics is directed towards binary logic gates[13,14] or transistors[15], but others have also pursued the possibility of neuromorphic computing[145] and analog computing[146].
A spin-wave interferometer on the nanoscale has already been realized, but the employed experimental techniques using visible light and microwave spectroscopy didn't allow for the required resolution in phase and k-space[147]. A concept for a magnonic analog adder has been proposed recently[148], however, an experimental realization of such a device was still lacking.
In this chapter, the experimental realization of magnonic analog adder devices based on two different materials, namely Permalloy ($Ni_{80}Fe_{20}$) and yttrium iron garnet (YIG) is presented. First, the sample design and preparation will be discussed, followed by a short description of the electrical setup. The results obtained using TR-STXM while varying the relative phase and amplitudes of the excitation signals give a proof of concept for the working principle, which relies on the interference of spin waves. Next, the frequency-division multiplexing capabilities of the device will be discussed, followed by concluding remarks and an outlook on further research.
All TR-STXM measurements have been performed at the *MAXYMUS* endstation of the *UE46* beamline at the *Helmholtz-Zentrum Berlin für Materialien und Energie*.

4.1 Sample Design and Preparation

In order to excite coherent spin waves which can interfere with each other, two metallic Cu microstrips with a width of 500 nm were patterned on

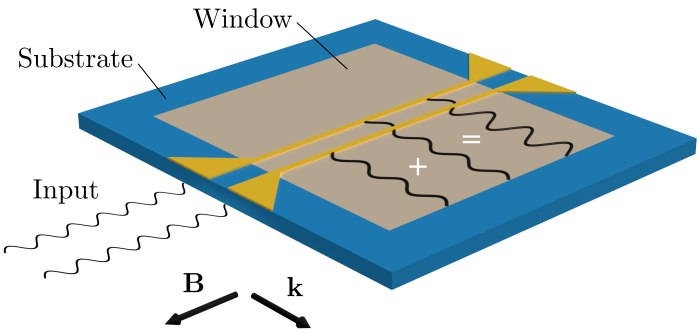

Figure 4.1: Sketch of the basic design principle of the magnonic analog adder, consisting of a magnetic substrate with an x-ray transparent window, onto which two microstrips are patterned. At the input, RF currents with an arbitrary phase shift are applied so that the spin waves which are excited by the microstrips Oersted field are in phase and interfere constructively (adapted from [149]).

top of a magnetic thin film using electron beam lithography and thermal evaporation, introduced in section 2.8. This was realized for two different magnetic materials, both used extensively in magnonics research, namely Permalloy, a metallic nickel iron alloy, as well as YIG, an insulating ferrimagnet, both having a low Gilbert damping parameter and low magnetic anisotropy. A sketch of the sample design is shown in figure 4.1. When a high frequency alternating current is flowing through these microstrips, a magnetic field is generated around them, which couples to the magnetic moments within the thin film, thereby exciting the coherent spin-wave dynamics[86]. The current densities for this excitation scheme are typically on the order of $10^{11}\,\mathrm{A/m^2}$. The spin waves can then travel through the film and interfere depending on their relative phase.

To observe and study this spin-wave interference, the measurement technique of TR-STXM was employed, which was introduced in sections 2.2

and 2.3. With this method, it is possible to directly observe the spin-wave interference by measuring the out-of-plane sample magnetization projected on the x-ray beam axis in a time-resolved manner, exploiting the x-ray magnetic circular dichroism (XMCD) effect, as introduced in section 1.3. This method requires the samples to be transparent to x-rays, which limits its total thickness to a few hundred nanometers, heavily depending on the material used. The procedure of sample preparation differs significantly for the two devices, and has been discussed in detail in chapter 2.9. The gap width was chosen to be 4 µm for the $Ni_{80}Fe_{20}$ based sample and 2 µm for the YIG based device.

4.2 Electrical Setup

The electrical setup used for the excitation of coherent spin-wave dynamics is shown in figure 4.2. An arbitrary waveform generator (AWG), which is synchronized to the synchrotron pulses, is used to generate two sine wave signals with an arbitrary phase shift φ. The synchronization scheme allows for a phase stabilized excitation of spin waves, as introduced in section 2.3. This also makes it possible to freely adjust the relative phase between the two input signals, which is crucial when determining the interference conditions for the adder device.

The two input signals are then going through a 30 dB broadband amplifier, which is protected by two -3 dB attenuators that prevent overload both from the AWG, as well as potential reflections.
Two pick-off tees are used to measure the input signal, which is sent to an oscilloscope with an attenuation of -20 dB coming from the pick-off tee.
The input signal is then going into the sample holder inside the STXM chamber, which is kept at 10 mbar He atmosphere to reduce heating effects,

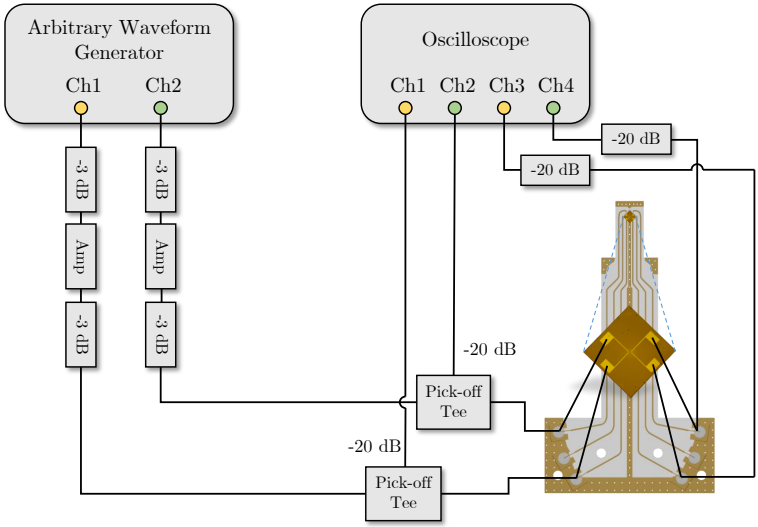

Figure 4.2: Sketch of the electrical setup used for the magnonic analog adder. The excitation signal is generated by an arbitrary waveform generator, with an adjustable phase shift between Channel 1 and 2. Both input and output signal are measured using an oscilloscope.

and into the two microstrips. This excites the spin-wave dynamics, but, depending mainly on the signal frequency, much of the power is reflected and not actually going through the sample, partially due to impedance mismatch. The output signal is then measured using Channel 3 and 4 of the oscilloscope, which is protected by -20 dB attenuators.

High current densities on the order of $1 \times 10^{10}\,\mathrm{A/m^2}$ to $5 \times 10^{11}\,\mathrm{A/m^2}$ are needed to create the oscillating magnetic field required for the excitation of spin-waves. Overall, this setup enables complete control over the excitation signal with regards to amplitude, phase, and in principle signal shape.

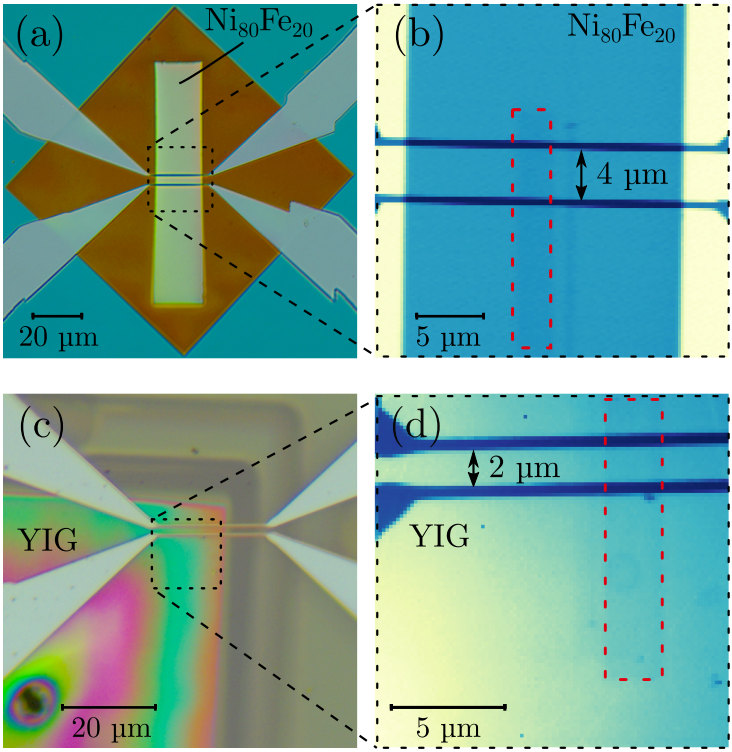

Figure 4.3: Optical micrographs (a,c) and STXM images (b,d) of the $Ni_{80}Fe_{20}$ (a,b) and YIG (c,d) based adder devices. In the static STXM images, the color indicates the number of photons measured in transmission. Blue indicates less, white indicates more transmission. The dashed red line marks the area where the dynamic measurements were taken.

4.3 STXM Measurements

Once electrical contact has been established, the dynamic magnetization measurements can be performed. With the sample installed inside the UHV chamber of MAXYMUS, it is first evacuated down to a pressure of approximately 10^{-6} mbar, and then flooded with He until a pressure

of 10 mbar is reached. The He atoms provide a way of heat dissipation, protecting the sample from excessive heat produced by the relatively high current densities flowing through the microstrip, which could lead to its destruction. Additionally, the magnetic properties of the films change as a function of temperature, an undesired effect that is reduced in He atmosphere.

Figure 4.3 shows optical micrographs of the devices, together with static STXM images of the area around the microstrips where the time-resolved magnetization measurements are made. The images for the $Ni_{80}Fe_{20}$ and YIG based devices were taken at 709.0 eV and 709.8 eV respectively. The microstrips are clearly visible as darker areas since they absorb more light. In case of the $Ni_{80}Fe_{20}$ device, the waveguide is also clearly visible due to its increased absorption with a width of approximately 20 µm. The dashed red lines in figure 4.3 mark the area where most of the spin-wave movies were recorded. These areas are slightly darker than their surroundings due to x-ray induced carbon deposition during the TR-STXM measurements, which were done before the image was taken. The interaction between highly energetic x-rays and residual carbon oxides in the UHV chamber leads to the deposition of a layer of C atoms on the surface, which in turn reduce transmission and make these areas appear darker.
The data presented in the following was obtained using the method introduced in section 2.3 and shows the z-component of the dynamic magnetization.

Device characterization

Before testing the devices for their functionality as analog adders, it is important to ensure optimal measurement conditions. This includes the choice of photon energy, determining their dispersion relation and field-dependence, as well as decay length. This will be done for both types of

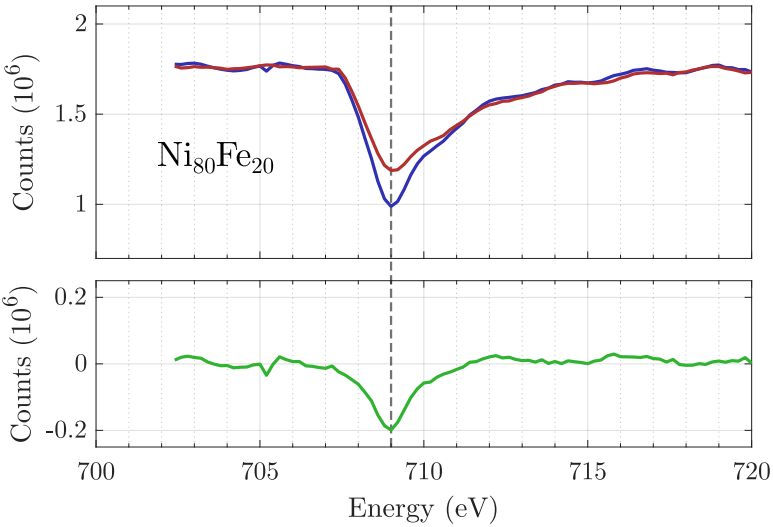

Figure 4.4: XAS (top) and XMCD (bottom) spectra of the $Ni_{80}Fe_{20}$ based analog adder device near the Fe L_3 edge. The XAS spectra were obtained by switching the magnetic field direction between parallel (blue) and antiparallel (red) alignment of photon angular momentum and magnetization.

devices, always starting with the $Ni_{80}Fe_{20}$ based one and then covering the YIG based device.

Choice of energy

Before the time-resolved measurements are performed, it is crucially important to determine the photon energy with the highest XMCD contrast. Figure 4.4 shows exemplary XAS and the corresponding XMCD measurements for a $Ni_{80}Fe_{20}$ sample near the Fe L_3 edge. The XAS spectra are recorded with $\pm 250\,\mathrm{mT}$ external field applied in the out-of-plane direction. From the XMCD spectrum, the maximum is determined to be at 709.0 eV, which was used in subsequent TR-STXM measurements. This notably

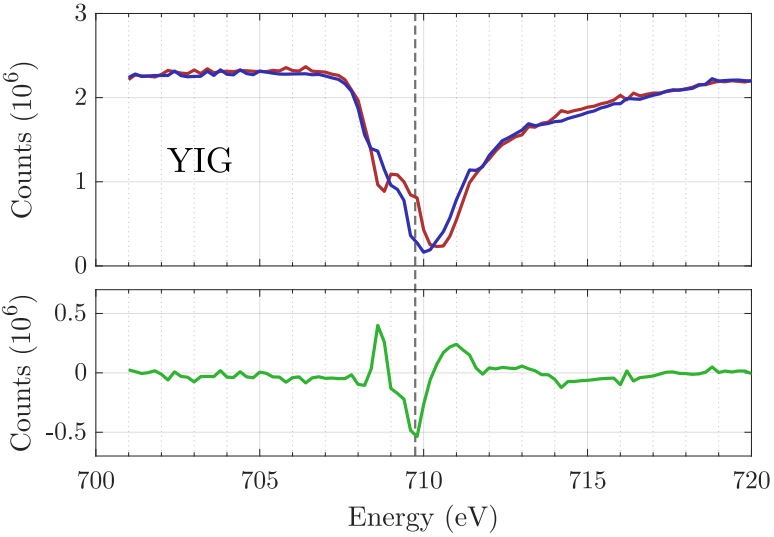

Figure 4.5: XAS (top) and XMCD (bottom) spectra of the YIG based analog adder device near the Fe L_3 edge. The XAS spectra were obtained by switching the magnetic field direction between parallel (blue) and antiparallel (red) alignment of photon angular momentum and magnetization.

differs from the literature value of 706.8 eV, which can be attributed to an energy offset of the undulator and monochromator.

The corresponding spectra for the YIG based adder are shown in figure 4.5, also measured at ±250 mT. The typical multiplet structure of YIG is visible, corresponding to the different Fe^{3+} sublattices[150]. One can see that small changes in the photon energy will have a large effect with regards to the magnitude and even sign of the XMCD effect. It is therefore more difficult to determine the correct energy in the case of YIG, as an additional shift of the absolute energy coming from the experimental setup can heavily affect the measurement. From the XMCD spectrum in figure 4.5 the optimal energy for the TR-STXM measurements was determined to be 709.8 eV. The counts of the XMCD spectra correspond to typical APD count rates in the multi bunch mode.

Determining the dispersion relation

An important step for testing the magnon adder is to obtain a basic understanding of the spin-wave dispersion relation, which gives the relationship between the energy (or frequency) of the spin waves and their wave vector **k**. For an in-plane saturated film in Damon-Eshbach geometry, the dispersion relation is given by equation (1.21). This was used to calculate the dispersion relation for the $Ni_{80}Fe_{20}$ and YIG based adder devices, shown in figure 4.6. It can be seen that increasing the magnitude of the external field results in the dispersion relation shifting up in frequency, while its general shape stays the same. The black crosses mark the points on the dispersion relation at which the TR-STXM measurements presented in this chapter were performed. For the $Ni_{80}Fe_{20}$ based adder, measurements were performed at $-25\,\mathrm{mT}$, $-40\,\mathrm{mT}$ and $-80\,\mathrm{mT}$, at excitation frequencies of $5.07\,\mathrm{GHz}$, $5.93\,\mathrm{GHz}$, and $7.57\,\mathrm{GHz}$. All shown measurements for the YIG based device were taken at a field of $-28\,\mathrm{mT}$, at excitation frequencies $2.72\,\mathrm{GHz}$ and $3.07\,\mathrm{GHz}$.

Field scan

Another interesting relationship is that between wave vector and external magnetic field. This can be studied experimentally in an elegant fashion by repeatedly performing time resolved line scans while varying the external magnetic field. That kind of measurement yields information on how the wavelength changes as a function of external field, and it can be repeated at different frequencies. This is then used to determine the parameters at which the adder device operates, and is especially important for determining

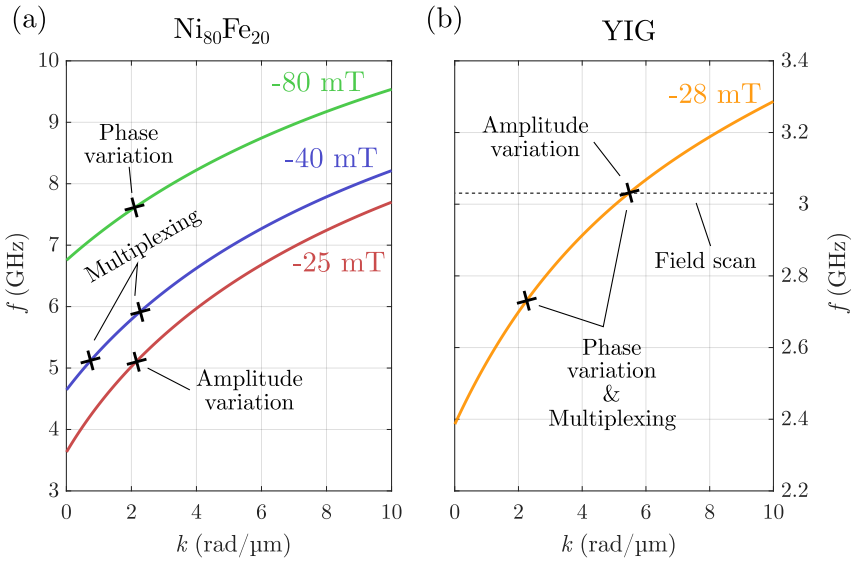

Figure 4.6: Dispersion relations for the (a) $Ni_{80}Fe_{20}$ and (b) YIG based adder devices for different external fields. The black crosses mark the values, at which the experimental data was recorded. The dashed line marks the frequency at which the field scan was done for the YIG based device. Parameters for $Ni_{80}Fe_{20}$: A_{ex}=1.3 × 10^{-11} pJ/m, M_s=515 kA/m, g=2. Parameters for YIG: A_{ex}=0.36 × 10^{-11} pJ/m, M_s=140 kA/m, g=2

the frequency for demonstration of the multiplexing capabilities, in order to have two wavelengths that are different enough to be discernible in the TR-STXM measurements.

Figure 4.7 shows such a *field scan* for the YIG based devices, ranging from −70 mT to 70 mT. Similar measurements have been performed for the $Ni_{80}Fe_{20}$ based device, but are omitted here since they do not give additional insight.

The center of figure 4.7 shows different line-scans as a function of external magnetic field, evaluated using the FFT algorithm introduced in section 2.3. What is displayed is the z-component of the dynamic magnetization,

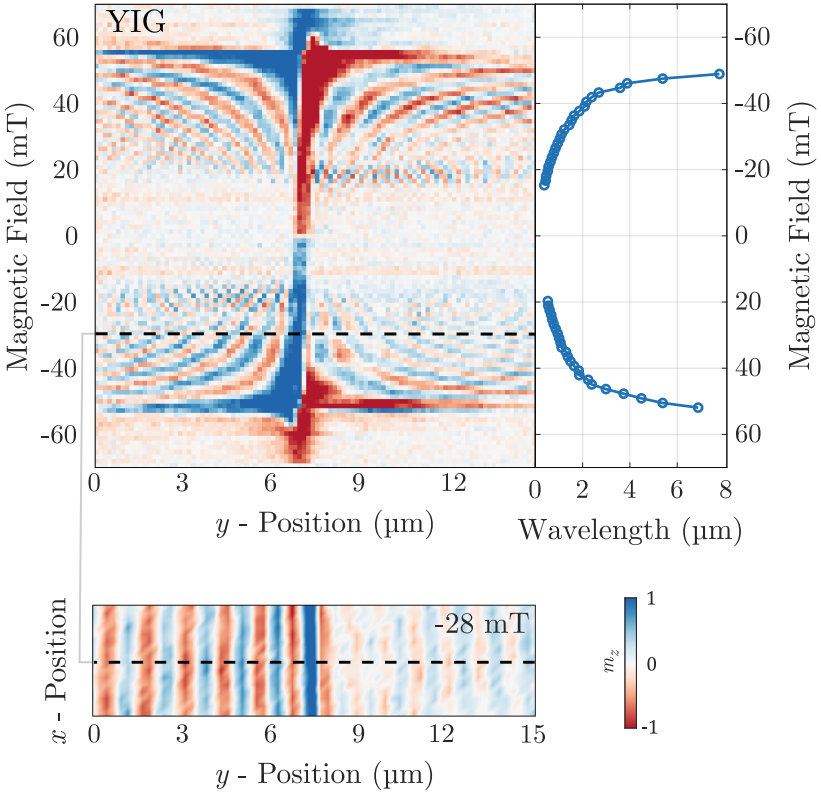

Figure 4.7: Field scan of the YIG based device recorded at 3.07 GHz with a line scan length of 15 µm along the y-direction (center), with the wavelength plotted as a function of magnetic field (right). At the bottom, an exemplary TR-STXM scan is shown to illustrate the direction along which the line scans were performed. Color indicates out-of-plane magnetization m_z.

normalized to the maximum value, indicated by the colorbar. The left part of the figure shows an TR-STXM area scan, corresponding roughly to the area in figure 4.3(d) marked by the red dashed line, just with an offset along the y-direction. This measurement was taken at a field of -28 mT and illustrates how the line scans were implemented, namely along

the y-direction, marked on the left with a dashed black line, which is also shown in the center.

It is evident that there is only a certain field range in which propagating spin waves are excited, with a minimum field of approximately 15 mT and a maximum field of 55 mT. The underlying mechanisms that give rise to these limits have already been discussed in in chapter 1.2.3. Another feature visible in the field sweep, as well as the single TR-STXM measurement at the bottom of figure 4.7, is the asymmetry of spin-wave emission. For negative fields, the amplitude is significantly larger towards the left, and the effect is reversed for positive fields. This is due to the relative phase between the momentary direction of the magnetic moments underneath the microstrip with respect to the Oersted field.

Decay length

Another aspect of device characterization is determining the decay length of spin waves in the magnetic material. The attenuation of spin waves can be modeled by an exponential decay of the amplitude. Figure 4.8 shows two examples how this is done, for the $Ni_{80}Fe_{20}$ and YIG based devices, respectively. In each case, the top part shows a TR-STXM measurement, analyzed using the FFT algorithm, of an area around the two microstrips. Only one microstrip is active, and shown with a dark gray. The inactive one is drawn in with a light gray for reference. The lower part of the figure shows a cross section of m_z, obtained by averaging along the x-axis in the image above. The blue circles mark the experimental values to which a function of the form

$$a \sin(bx + c) \cdot \exp(-dx) + e \tag{4.1}$$

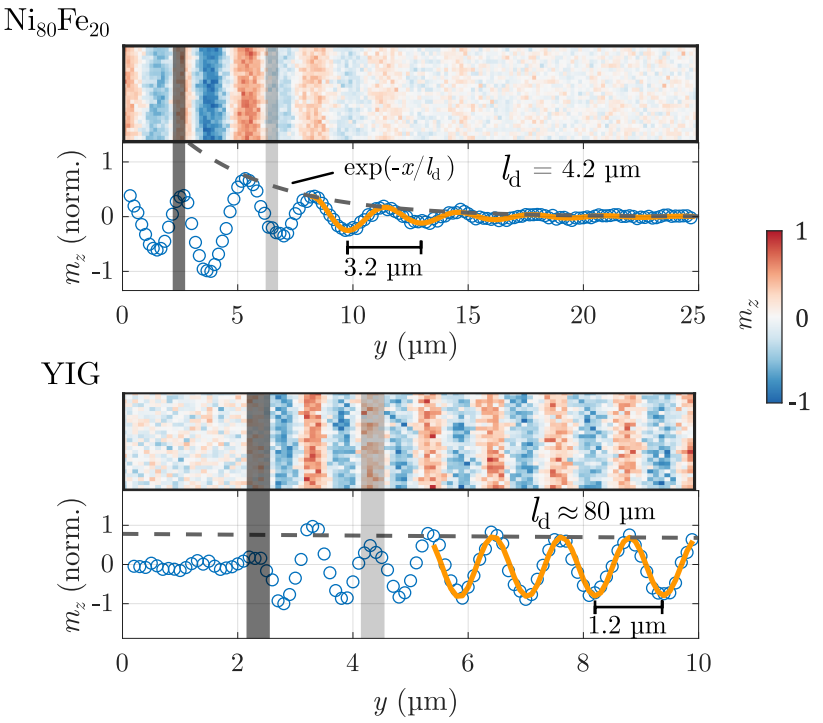

Figure 4.8: TR-STXM measurements with corresponding cross section for the $Ni_{80}Fe_{20}$ based device at 5.07 GHz and −25 mT (top) and the YIG based device at 3.07 GHz and −28 mT (bottom). Only the first microstrip is active. The cross section was obtained by averaging along the x-axis, and a fit (orange) was used to extract decay length, as wall as wavelength.

can be fitted. The parameters b and d are used to calculate the wavelength $\lambda = 2\pi/b$ and the decay length $l_\mathrm{d} = 1/d$. The decay length gives the distance after which the amplitude has decreased by a factor of $1/e \approx 0.37$. This is depicted in figure 4.8 by the gray dashed line, the envelope of the sine wave. Underneath the second microstrip, the signal is clearly distorted for both devices, so the fit was only applied to the area beyond the second microstrip.

The decay length crucially depends on the frequency. However, the order of magnitude of spin-wave attenuation can be approximated by looking at one exemplary frequency. For the $Ni_{80}Fe_{20}$ based device, a frequency of 5.07 GHz was chosen, where a wavelength of 3.2 µm and a decay length of $l_d = (4.2 \pm 0.4)$ µm was measured, with the cross section in figure 4.8 showing excellent agreement between the exponential envelope and the experimental data.

For the YIG based device, the measurements were performed at a frequency of 3.07 GHz and an external field of −28 mT. This yielded a wavelength of 1.2 µm, and a decay length of (80 ± 40) µm. The large uncertainty in l_d arises partly because the scan area is much smaller than the attenuation length. Spin-wave propagation is highly sensitive to inhomogeneities in the film thickness, which affect all relevant energy terms of the effective field (Equation (1.20)), with a different temperature dependence for each contribution.

Phase variation

Calibration - the first step in verifying the analog adder devices functionality is to study the interference conditions. For this, the phase between the two input signals going into the two microstrips is varied, while measuring the amplitude using TR-STXM. The asymmetric emission of spin waves gives a distinguished direction, which lets us define a *first* and *second* microstrip.

For the first measurement, equal excitation amplitudes are applied with a random initial guess for the phase, and then subsequent measurements are taken while incrementing the phase in steps of 90°. This will only approximate the point of destructive interference, and further optimization is made by means of a bisection method. Since the amplitudes haven't been optimized yet, this approach will only yield a local minimum, and not com-

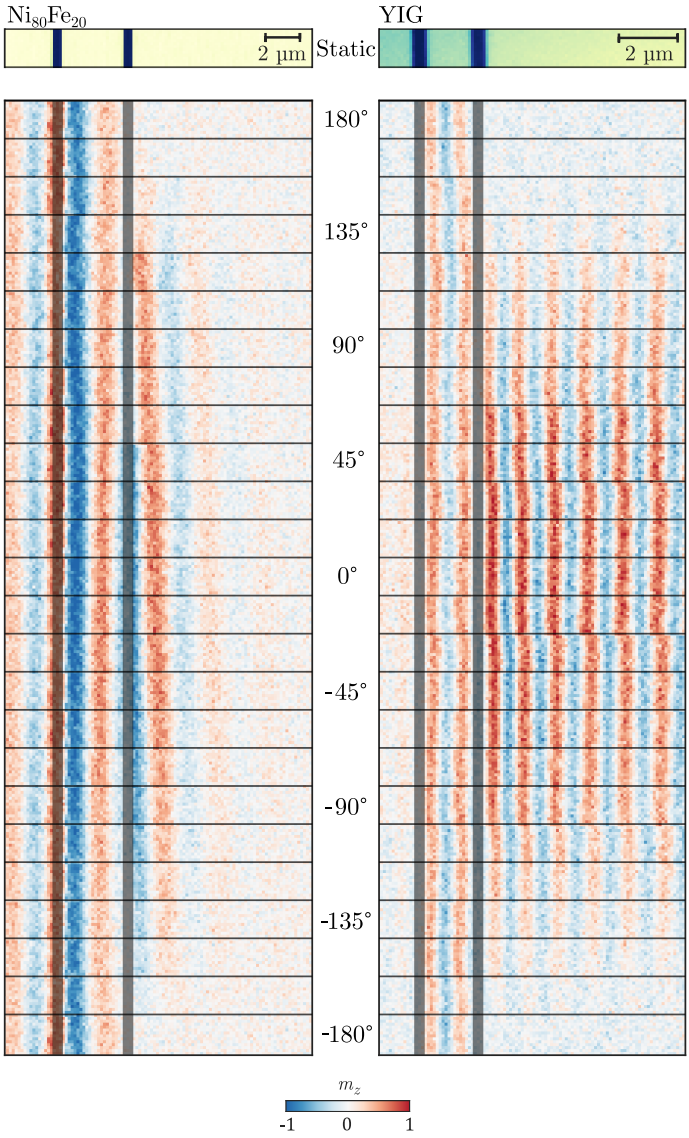

Figure 4.9: TR-STXM images of a phase variation series for the $Ni_{80}Fe_{20}$ based device at 7.57 GHz and −80 mT (left) and YIG based device at 3.07 GHz and −28 mT (right). Corresponding static images are found at the top, color indicates m_z (colorbar only for dynamic measurements).

plete destructive interference. To achieve that, one input signal strength is fixed and the other varied until the spin-wave amplitude is minimized. The different amplitudes compensate variations in signal transmission, and, more importantly, the attenuation of the spin waves traveling from the first to the second microstrip, where they interfere. This attenuation is much larger in the $Ni_{80}Fe_{20}$ device compared to the one based on YIG due to their difference in Gilbert damping.

Once the phase and amplitude needed for complete destructive interference are determined, this phase is defined to be $\varphi = 180°$. From this starting point, a systematic study of the phase dependence in steps of 15° is performed, with the corresponding TR-STXM measurements for one frequency shown in figure 4.9, for both the $Ni_{80}Fe_{20}$ and YIG based devices.

A static STXM image of the scan area is shown at the top, and the microstrips are marked in each image with a gray box. Phase of the first (top) microstrip was kept fixed while the one of the second (bottom) one was varied. Both devices show more signal to the right of the second microstrip around 0° and almost no signal for 180° phase shift.

$Ni_{80}Fe_{20}$ - In the $Ni_{80}Fe_{20}$ based device (left side of figure 4.9), the waves are strongly attenuated and almost no signal is left at the edge of the scan area, which extends 10 µm beyond the second microstrip. Due to the high attenuation, the excitation signal of the second microstrip had to be reduced by a factor of 0.2 compared to the first microstrip to compensate for the attenuation. Between the two antennas, the spin-wave pattern is left almost unchanged when varying the phase, in accordance with the consideration of asymmetric spin-wave emission. The area in between is therefore dominated by the waves coming from the left microstrip, whose phase is left unchanged. One peculiar feature is the apparent change in wavelength when going from left to right. The behavior is expected to be symmetric around the point of constructive interference (0°), however, increasing the phase shift results in a different pattern than reducing

it. This is most likely arising from electrical crosstalk between the two microstrips, which isn't necessarily symmetric around 0° phase shift.

YIG - The YIG based device (right side of figure 4.9) shows an overall increased signal-to-noise ratio, but also much higher emission asymmetry. All data was recorded at 3.07 GHz and −28 mT. The sign of the magnetic field was again chosen so that the waves travel rightwards along the x-direction. This is necessary since the homogeneous area of the FIB window extends far more towards this direction, as can be seen in figure 4.3(c). Hardly any signal is detected to the left of the first microstrip, and so the area between the two antennas is completely dominated by the effect of the left microstrip. At 180° phase shift, there's no periodic signal remaining left of the second microstrip, showing complete destructive interference. Both images at 165° and −165° show a small signal, as is expected.

Quantitative analysis of the phase variation measurements

While the general characteristics of constructive and destructive interference can be seen in figure 4.9, a quantitative evaluation is necessary to confirm the operating principle. For that, the FFT amplitude is determined as a function of phase φ by averaging over an area beyond the second microstrip, as depicted in figure 4.10(a) for the $Ni_{80}Fe_{20}$ based device. The top part of the figure shows the amplitude obtained by Fourier analysis of a TR-STXM measurement, with the corresponding cross section below. It can be seen that the amplitude is largest close to the microstrip towards the right, and decaying exponentially. The averaging area was chosen at a distance roughly corresponding to the gap between the two microstrips. In a device with electrical output, this constitutes a suitable position of the readout.

In figure 4.10(b), the amplitude as obtained from averaging is plotted as a function of the relative phase φ, normalized to the maximum value. At

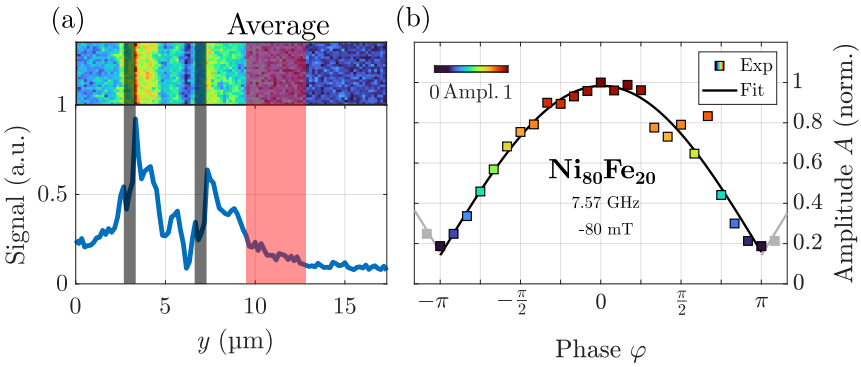

Figure 4.10: Quantitative analysis of the phase variation measurements in the $Ni_{80}Fe_{20}$ based device at a frequency of 7.57 GHz and an external field of −80 mT. (a) FFT Amplitude of a TR-STXM measurement (top) with the respective cross section (bottom). The area where the average is taken is marked in red. (b) Normalized spin-wave amplitude as a function of relative phase. The colored squares represent the experimental data points, the solid line shows the theoretical prediction for two interfering waves.

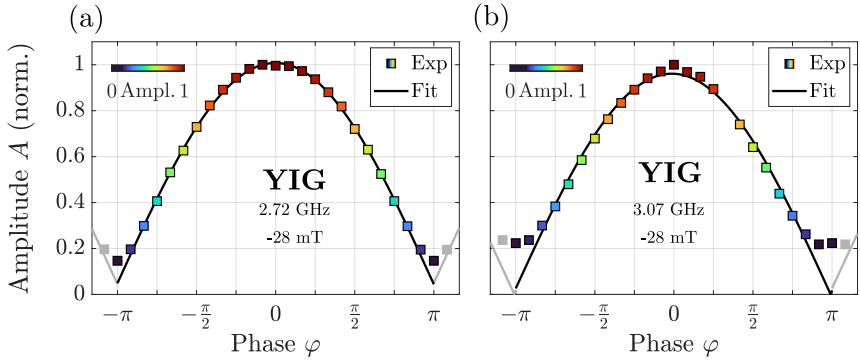

Figure 4.11: Normalized spin-wave amplitude as a function of relative phase for the YIG based analog adder device at an external field of −28 mT and at an excitation frequency of (a) 2.72 GHz and (b) 3.07 GHz. The colored squares represent the experimental data points, the solid line shows the theoretical prediction for two interfering waves (adapted from [149]).

the position where the averaging is done, the spin waves coming from both microstrips are interfering. Damon-Eshbach type spin waves are expected to be of sinusoidal form, and so their linear superposition can be described as

$$\sin(kx) + \sin(kx + \varphi) = 2\cos(\varphi/2) \cdot \sin(kx + \varphi/2) \tag{4.2}$$

for one moment in time. This assumes that their amplitude is equal, which was ensured by determining the point of complete destructive interference. The resulting wave is therefore another sine-wave with a phase shift of $\varphi/2$ and an amplitude proportional to $2\cos(\varphi/2)$. This proportionality was used for the fit function seen in figure 4.10(b), which is of the form

$$a \cdot \cos(\varphi/2) + b. \tag{4.3}$$

Overall, there's good agreement between the theoretical prediction and the experimental data, however, due to the high spin-wave attenuation, signal-to-noise ratio was sometimes poor, resulting in some outliers. Another striking feature is that the amplitude A does not completely vanish at a phase shift of $\pm\pi$. This non-zero residual value arises in parts from imperfect amplitude balancing and interference conditions, as well as inhomogeneities in the sample that don't allow for perfect destructive interference over the whole area. The most significant contribution, however, stems from measurement noise, which will be even more obvious in the context of amplitude variation in section 4.3.

The corresponding analysis for the YIG based sample is shown in figure 4.11 for two frequencies, 2.72 GHz and 3.07 GHz, both with an external field of -28 mT. Again, equation (4.2) was used to fit the experimental data, this time with better agreement than in the case of $Ni_{80}Fe_{20}$. The two most important factors for the improved results are the increased signal-to-noise ratio for YIG, as well as the reduced electrical cross-talk, owing to the insulating properties of YIG. However, a non-zero signal is observed at supposedly complete destructive interference, again partly

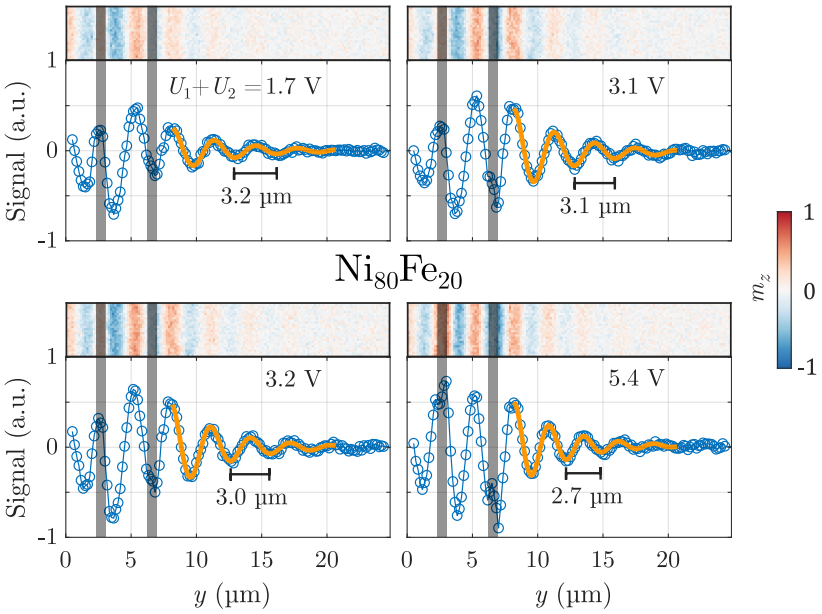

Figure 4.12: Amplitude variation in the $Ni_{80}Fe_{20}$ based device at an external field of -25 mT and an excitation frequency of 5.07 GHz. Exemplary TR-STXM measurements with corresponding cross sections at constructive interference for different input signal strengths.

caused by imperfect amplitude balancing and interference conditions, as well as inhomogeneities. The last aspect is much more pronounced in the YIG based adder device due to the manual thinning process. The most important factor, the interplay between evaluation method and measurement noise, will be discussed in the following section.

Amplitude variation

The performance of an analog adder device can only be tested by systematically varying the excitation strengths, and therefore the spin-wave

amplitudes. By evaluating these amplitude variation measurements, it is possible to confirm the commutative property

$$a + b = b + a, \tag{4.4}$$

the general functionality of the addition operation

$$1 + 5 = 2 + 4 = 3 + 3, \tag{4.5}$$

as well as linearity, since doubling the input will result in double the output.

To demonstrate that the analog adder devices fulfill these requirements, the phase is set to $\varphi = 0$, the condition for constructive interference between the spin waves emitted by the two microstrips. Next, the strength of the excitation signal at each microstrip is varied individually. In the following, this signal strength will be given in units of mV, as measured right in front of the sample using channel 1 and 2 of the oscilloscope, as depicted in figure 4.2. The $-20\,\mathrm{dB}$ attenuation from the pick-off tee is compensated in the oscilloscope software.

$Ni_{80}Fe_{20}$ - for the $Ni_{80}Fe_{20}$ based device, a problem occurred due to the relatively low signal-to-noise ratio. In order to achieve sufficiently high spin-wave amplitudes, the excitation signal had to be so high that any variation resulted in a change of temperature that affected the samples magnetization. This in turn, in accordance with equation (1.21), resulted in a different wavelength and therefore changing interference conditions. This effect can be seen in the amplitude series shown in figure 4.12. Four measurements with increasing input signal are shown, with the top showing Fourier analyzed TR-STXM scans, and the bottom the corresponding cross section. Using equation (4.1), the wavelength was determined, which decreases significantly, from 3.2 µm to 2.7 µm when increasing the input signal roughly by factor of 3. Overall, it was not possible to obtain good quantitative results for the $Ni_{80}Fe_{20}$ based device using this method.

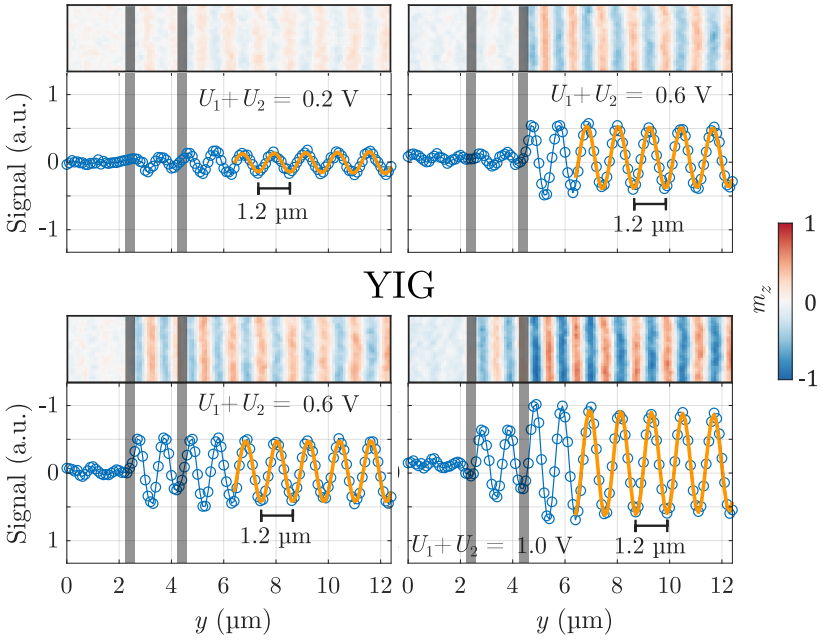

Figure 4.13: Amplitude variation in the YIG based device at an external field of −28 mT and an excitation frequency of 3.07 GHz. Exemplary TR-STXM measurements with corresponding cross sections at constructive interference for different input signal strengths.

YIG - exemplary TR-STXM measurements of the YIG based adder device with different amplitudes are shown in figure 4.13. It can be seen that increasing the input power results in significantly higher spin-wave amplitudes. The top right and bottom left panel of figure 4.13 both show a total input amplitude of 0.6 V, with one microstrip being supplied with 0.1 V and the other one with 0.5 V. Due to the low damping of YIG, it was not necessary to adjust the excitation signal to compensate the reduced amplitude of the spin-wave coming from the left microstrip. This is why the resulting spin-wave pattern on the right side looks identical in the top right and lower left panel of figure 4.13. Most importantly, it can be seen that

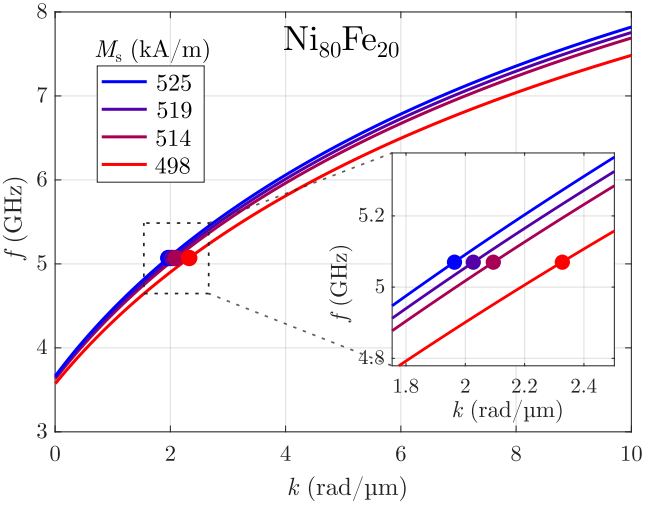

Figure 4.14: Dispersion relations of a 50 nm $Ni_{80}Fe_{20}$ film with different values of M_s to reproduce the wavelengths observed in the previous amplitude variation measurements, marked by filled circles.

the wavelength does not change at different input powers and stays at a constant value of 1.2 µm, proving the stability of the interference condition in a quantitative manner.

Quantitative analysis of the amplitude variation measurements

Figure 4.12 has illustrated how the spin-wave wavelength in the $Ni_{80}Fe_{20}$ based device changed as a function of excitation amplitude. The observed effect can be understood in terms of a change in saturation magnetization caused by a change in temperature. To quantitatively understand this effect, the dispersion relation of a 50 nm $Ni_{80}Fe_{20}$ film was calculated for

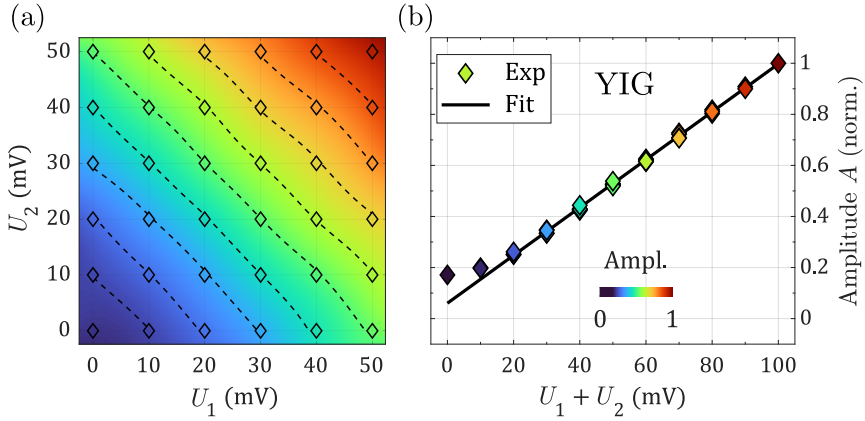

Figure 4.15: Quantitative analysis of the amplitude variation in the YIG based device at a frequency of 3.07 GHz and an external field of −28 mT. (a) Amplitude landscape with equiamplitude lines, color corresponding to their value. (b) Normalized amplitude as a function of the sum of input voltages, together with a linear fit (adapted from [149]).

different values of M_s using equation (1.21). Figure 4.14 shows the dispersion relations that match the experimentally determined wavelengths from figure 4.12, corresponding to saturation magnetization values of 525 kA/m, 519 kA/m, 514 kA/m, and 498 kA/m.

For the quantitative analysis of the YIG device, the input signal was varied from 0 mV to 50 mV in steps of 10 mV for each microstrip, resulting in 36 data points, which are depicted as a surface plot in figure 4.15(a). Again, the amplitude was determined by averaging the FFT amplitude in an area behind the second microstrip according to 4.10(a). So each data point corresponds to a TR-STXM measurement over the whole area.
Figure 4.15(a) mainly serves the purpose of indicating what measurements were made, however, the color of the data points also indicate the measured amplitude. A continuous landscape was then obtained by linear interpolation between the data points, and additional equiamplitude lines were drawn in. The value at which these equiamplitude lines are plotted is

determined by averaging over all data points that are expected to have the same amplitude, namely where the sum of input signals U_1 and U_2 is equal. When a data point deviates from the equiamplitude line, it means that it did not yield the expected result, so it indicates that the device is not working properly. However, in figure 4.15(a), all data points align nicely with the dashed lines. The color scale is not very well suited for checking whether or not the expected linear relationship is fulfilled.

To evaluate the results in a quantitative fashion, the data points are also plotted as a function of the sum of the two inputs, namely $U_1 + U_2$, in figure 4.15(b). All data points corresponding to one equiamplitude line are therefore now on top of each other. It can be seen that the amplitudes agree within 2 %, a value that could be further improved by electrical measurement [14].

One noticeable feature, similar to the phase variation analysis, is the non-zero amplitude at zero input. In this case, the reason cannot be imperfect interference conditions, since no signal whatsoever is transmitted through the microstrips, and no coherent spin waves are excited. Also, with the employed stroboscopic measurement method, thermal magnons are not detectable, and so they can not contribute to this signal.

This means that the remaining signal must come from the interplay of the evaluation method and measurement noise and is therefore no inherent feature of the device.

Frequency-division multiplexing

For practical computing applications, bandwidth plays an important role. One common way to increase bandwidth is frequency-division multiplexing, where signals with different frequencies are processed in parallel [151]. When operating the analog adder in the linear regime, the overall signal can be described as a linear superposition of the signals at different frequencies.

Therefore, each spin wave should in principle interfere independently, meaning that when the signal is separated into its frequency components, each component should individually show the behavior that was demonstrated in the previous sections. This means that depending on their relative phase, they interfere in the manner shown in figure 4.10 and figure 4.11. This linearity will also ensure that the addition of spin-wave amplitudes is linear in the sense discussed in section 4.3 and shown specifically in figure 4.15(b).

For the simultaneous usage of different frequencies, demultiplexing is required, disentangling the overall signal into its frequency components by utilizing the Fourier transformed signal. By choosing different components of the Fourier spectrum, it is possible to obtain sensitivity for only one frequency component. Hence careful consideration regarding channel number N and *magic number* M is needed. While N is fixed for one measurement, M_1 and M_2 will determine the individual excitation frequencies according to equation (2.5). If M_1 and M_2 differ by an integer multiple of N, it is not possible to disentangle the signals.

$Ni_{80}Fe_{20}$ - figure 4.16 shows TR-STXM measurements of the $Ni_{80}Fe_{20}$ based device with multiplexing using two frequencies, namely 5.07 GHz and 5.93 GHz. The top right panel shows a static image for reference, with the microstrips clearly visible. The middle and bottom row show the four possible combinations of constructive and destructive interference for the two frequencies respectively. The area for which the interference was optimized is again below the second microstrip.
One can see that in the first of the four panels (label *Constructive*), both frequencies interfere constructively, and a mix between long and short wavelengths can be seen below the second microstrip.
In the second panel (label *Destructive*), the spin waves cancel out for both frequencies, and very low intensity remains. However, it can be seen that some signal still remains, especially close to the edges of the $Ni_{80}Fe_{20}$ stripe.

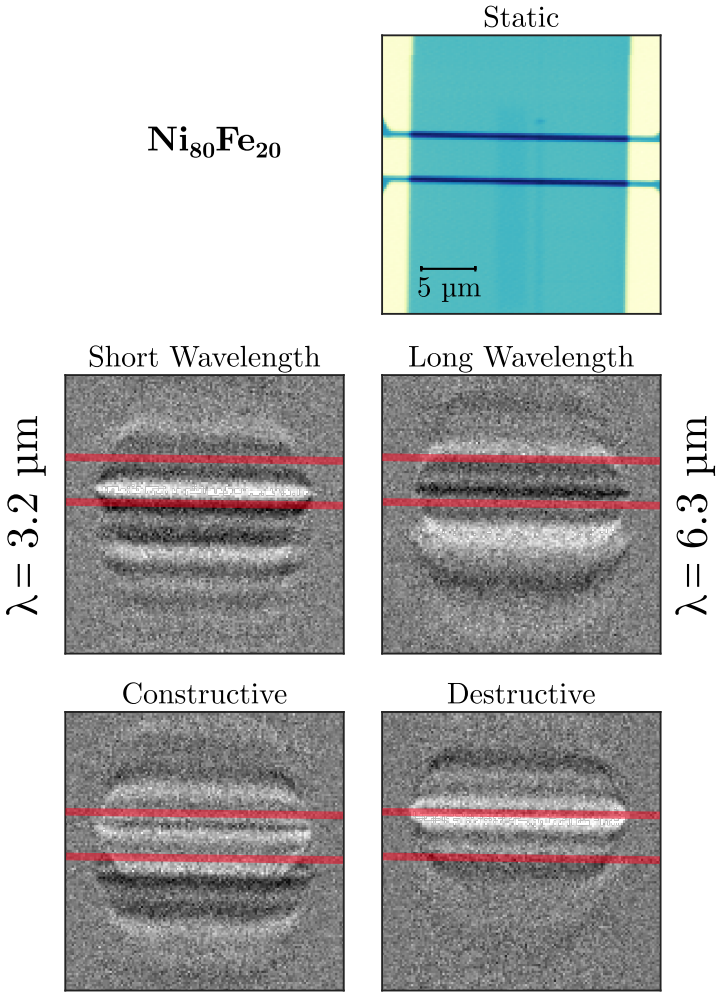

Figure 4.16: Demonstration of frequency multiplexing in the $Ni_{80}Fe_{20}$ based adder device at an external field of −40 mT. TR-STXM measurements with two simultaneous excitations at 5.07 GHz and 5.93 GHz, individually either interfering constructively or destructively (middle and bottom row). Color indicates normalized m_z component, microstrip position marked by red lines. Static STXM image for reference (top right).

The demagnetizing field in these areas change spin-wave propagation [152] and therefore interference conditions, which were optimized only for the center of the $Ni_{80}Fe_{20}$ stripe.
The third panel (label *Short Wavelength*) shows the case where the 5.07 GHz component interferes destructively, while the shorter wavelength 5.93 GHz component interferes constructively. Below the second microstrip, only short wavelengths are visible. The opposite case is shown in the last panel (label *Long Wavelength*), where only a long wavelength is visible below the second microstrip.

The choice of frequencies was not optimal for the $Ni_{80}Fe_{20}$ adder, and so it was not possible to separate the signal into its frequency components in a single measurement. It was nevertheless possible to show the feasibility of frequency-division multiplexing in the case of two frequencies by individually controlling their interference. The number of different frequencies used is however limited by Joule heating, which increases with the total signal amplitude. As was discussed before, an increase in temperature leads to a change in wavelength and therefore alters the interference conditions. When this change is too large, device functionality will be impaired.

YIG - for the YIG based analog adder, the excitation frequencies were chosen more carefully, and so it was possible to disentangle the measured signal. Figure 4.17 again shows TR-STXM measurements for the four different combinations of constructive and destructive interference of two excitation frequencies. Here, it was possible to split up the signal in two parts, corresponding to oscillations at 2.72 GHz and 3.07 GHz, indicated by the arrows. The scan area corresponds to the one marked by the red dashed line in figure 4.3(d). The most interesting features can be seen in figure 4.17, since both frequency components interfere constructively, and their superposition shows both long and short wavelengths.

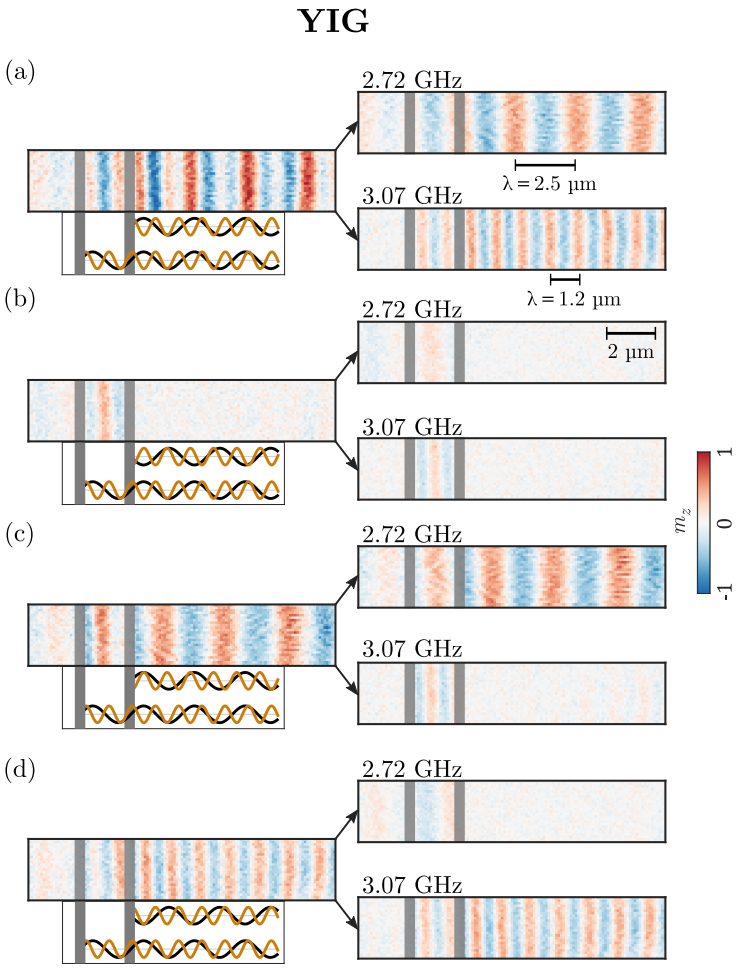

Figure 4.17: TR-STXM measurements of frequency multiplexing in the YIG based adder device at −28 mT with simultaneous excitation at 2.72 GHz and 3.07 GHz. The left side shows the overall signal (top) with a sketch of the frequency components (bottom). The right side shows the demultiplexed signal for the two frequency components. Different interference conditions are shown, (a) both frequencies interfere constructively, (b) both interfere destructively, (c) the long wavelength component interferes constructively, the short one destructively, (d) the opposite of (c). Color indicates normalized m_z component (adapted from [149]).

When split up, only one of the frequencies is visible anymore. It is important to keep in mind that all three images shown in figure 4.17(a) show the same TR-STXM measurement, just post-processed in different ways, demonstrating a way of demultiplexing using Fourier transformation. Figure 4.17(b) shows the case where both components interfere destructively. While there's still short and long wavelengths visible in between the microstrips, no signal remains behind the second microstrip. Comparing this to the measurements shown in figure 4.9, it becomes evident that the different frequency components do not impair each other and interference conditions are still optimal. This again shows that the device is operating in the linear regime. Finally, the cases where one of the frequencies is interfering constructively and the other destructively is shown in figure 4.17(c) and (d).

4.4 Conclusion

It was shown that an analog adder prototype consisting of an extended ferromagnetic layer and based on interfering spin waves is feasible. For that, two different devices, one based on metallic $Ni_{80}Fe_{20}$, the other on the ferrimagnetic insulator YIG were fabricated using electron beam lithography and thin film deposition methods. The devices were first characterized using x-ray absorption spectroscopy, as well as field-dependent TR-STXM line scans to obtain information on the relation between frequency, external field, and wavelength of the spin waves.

To explore the interference conditions of each device, TR-STXM measurements were performed while varying the relative phase between the two inputs. The data was analyzed by means of an FFT algorithm to obtain information on the spin-wave amplitude, which could successfully be fitted to the theoretical prediction.

The input signal amplitudes were then varied in order to show the adder devices functionality with regards to linearity, commutativity, and the addition operation in general. A quantitative confirmation, however, was only possible for the YIG based device. In case of the $Ni_{80}Fe_{20}$ based device, Joule heating resulted in a change in wavelength which affected the interference conditions, affecting the quantitative analysis and demonstrating the importance of temperature control.
Lastly, the frequency-division multiplexing capabilities of the magnonic analog adder were explored by simultaneous excitation with two different frequencies. For the $Ni_{80}Fe_{20}$ based device, it could be shown that the two frequency components could be controlled independently with regards to either destructive or constructive interference, additionally confirming that the device was operating in the linear regime. The same could be done for the YIG based device, with the added merit of being able to separate the different frequency components using the FFT analysis method. This also demonstrated a technique for demultiplexing, which could also be employed in an electrical measurement setup.

Overall, the functionality of a magnonic analog adder was shown by means of direct observation of the spin-wave interference using TR-STXM, constituting an important step towards alternative computing schemes in magnonics.

One possible next step for future studies would be to implement an electrical setup for measuring the spin-wave amplitude in order to ensure compatibility with other electronic devices and even CMOS architecture. Another interesting feature that is yet unexplored in this device are nonlinear effects, which could open up a range of new applications. However, due to the working principle of the analog adder, which relies on controlled spin-wave interference, it would be necessary to reach the nonlinear regime while still maintaining stable interference conditions, which for $Ni_{80}Fe_{20}$ requires temperature stability. This might be possible in a sample with

electrical readout, since no membrane window is needed for observation, and heat conduction is therefore greatly increased.

5 | Direct Observation of Propagating Spin Waves in the van der Waals Magnet Fe_5GeTe_2

The discovery of two-dimensional (2D) van der Waals (vdW) materials, starting with graphene, has opened up many new opportunities to study physical phenomena in reduced dimensionality [37,153]. This is interesting both from a fundamental physics point of view, as well as in perspective of new technological applications. Many physical systems behave in different and often unexpected ways in the 2D limit. This has been studied with regards to electron transport, optics, and optoelectric properties, most prominently in graphene [154,155]. Possibilities for exploiting these effects in new technological applications has been of great interest and inspired many scientific endeavors [156–158].

Another physical phenomenon that behaves differently in reduced dimensionality is magnetism, and the discovery of 2D magnetic materials such as $Cr_2Ge_2Te_6$ and $FePS_3$ made it possible to systematically study the magnetic properties of these materials down to the monolayer limit [43,44].

Table 5.1: Overview over different magnetic 2D vdw materials and their critical temperature in bulk $T_{C,bulk}$, few layer systems $T_{C,few}$, and monolayers $T_{C,mono}$. A more complete overview can be found in [165].

Material	$T_{c,bulk}$(K)	$T_{c,few}$(K)	$T_{c,mono}$(K)
$CrCl_3$ [166,167]	18	16	-
$Cr_2Ge_2Te_6$ [168–170]	61	30	-
CrI_3 [171]	61	-	45
$CrBr_3$ [172,173]	37	-	34
$CrTe_2$ [174,175]	310	300	200
Fe_3GeTe_2 [176,177]	230	-	130
Fe_5GeTe_2 [162–164]	270-330	270-300	-

Most magnetic vdW materials have a relatively low Curie temperature well below room temperature, owing to the fact that atoms near a vdW interface find a reduced number of nearest neighbors to which they can couple, thus reducing the overall interaction energy and rendering the magnetically ordered state less stable against thermal fluctuations [1]. Nevertheless, some materials have been discovered that show magnetic ordering even in very thin films, such as $FePS_3$ [41,42], CrI_3 [44], Cr_2Te_3 [159,160] and Fe_3GeTe_2 [161]. The Curie temperatures for a selection of 2D vdW materials are shown in table 5.1, with values for the bulk material, few layers, and monolayers. It can be seen that many vdW materials have a too low Curie temperature for room temperature technological applications. One of these candidates is Fe_5GeTe_2, which exhibits Curie temperatures between 270 K and 330 K depending on the specific growth conditions and resulting Fe content [162–164].

Preparing devices with magnetic vdW materials comes with a set of challenges, first and foremost their tendency to oxidize under ambient conditions and the occurrence of mechanical stress. When preparing a sample using mechanical exfoliation, it is also difficult to control the size

of the flake, and it has to be protected from oxidation by another layer, usually hexagonal boron nitride (hBN).

Precise control of spin-wave dynamics in 2D materials could open up the possibility of vdW heterostructures for magnonic applications. Measuring spin-wave dynamics with both spatial and temporal resolution can additionally give insight into properties such as magnetic coupling and anisotropies [48,103]. By comparing the spin-wave dispersion to a model, some of these parameters can be inferred. However, only very few experimental techniques allow for the direct determination of the spin-wave dispersion at sub-optical wavelengths, and so the functionality of ferromagnetic vdW layers as a spin-wave medium has not been studied yet in a direct manner. Raman spectroscopy on CrI_3 [178] and antiferromagnetic resonance studies on $CrCl_3$ [179] gave insight only into the dispersion relation with no direct observation of coherent propagating spin-waves. Time-resolved scanning transmission x-ray microscopy (TR-STXM), with its unique combination of sub-optical resolution down below 20 nm and temporal resolution down to 10 ps, is an optimal method to investigate spin-wave dynamics in thin flakes with a typical thickness of 3 nm to 100 nm.

In this chapter, the results of studying Fe_5GeTe_2 flakes by means of SQUID magnetometry, as well as static and time resolved STXM will be presented. Propagating spin-waves are excited by means of coupling of the Oersted field of a microstrip to the magnetic moments in the Fe_5GeTe_2 flake and directly observed by TR-STXM. The results are compared to a model based on the semi-analytical dynamic matrix approach introduced in 2.10. First, the sample design and preparation will be discussed. Then, the SQUID magnetometry and static STXM measurements are presented, followed by the TR-STXM results for different external fields and excitation frequencies. These dynamic measurements are then compared to the multilayer model, where the influence of saturation magnetization and interlayer coupling strength on the spin-wave dispersion is discussed. Finally, concluding remarks and an outlook on future studies is given.

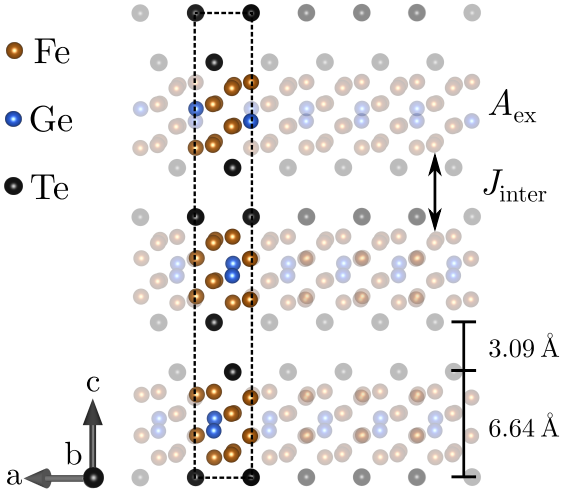

Figure 5.1: Crystal structure of Fe_5GeTe_2 with the unit cell marked by dashed lines. Intralayer exchange A_{ex} and interlayer coupling J_{inter} symbolically marked, as well as layer thickness and vdW gap width.

5.1 Sample Design and Preparation

Figure 5.1 shows a sketch of the crystal structure of Fe_5GeTe_2 with its rhombohedral symmetry, best described by the R$\bar{3}$m space group (No. 166)[180]. The a and b axes lie within the vdW layers, and the c-axis perpendicular to this plane. The unit cell is marked by dashed lines and spans across three van der Waals layers, each with a thickness of 6.64 Å and a gap width of 3.09 Å. The crystal structure shown in figure 5.1 includes two split sites for one of the five Fe atoms, of which only one is occupied at one time. This was found to induce intrinsic structural disorder, while still maintaining local short-range, and is expected to have an influence on the magnetic properties of Fe_5GeTe_2 with regards to homogeneity and damping[162,181].

Generally, magnetic interactions are strongly anisotropic in magnetic 2D materials, owing to the difference in distance between magnetic atoms within a layer and that across the layer gap width. This can be modeled by introducing an interlayer coupling constant J_{inter} complementing the intralayer exchange stiffness A_{ex}. While the exchange stiffness is given in units of J/m, J_{inter} is given in terms of energy per unit area (J/m^2). This kind of anisotropic exchange can readily be implemented in the multilayer model introduced in section 2.10 and will be used to calculate the magnetic properties of Fe_5GeTe_2 later on.

The basis for the preparation of thin flakes was a single crystal of Fe_5GeTe_2, which was synthesized from the pure elements Fe, Ge, and Te. These were placed in a vacuum-sealed quartz ampule at a ratio of 6:1:2 together with iodine acting as a mineralizer. The ampule was then put in an oven and heated up to a temperature of 750 °C at a rate of 120 °C/h, kept at the maximum temperature for 2 weeks, and then slowly cooled down inside the oven. Energy-dispersive x-ray (EDX) spectroscopy was employed to measure the elemental composition of the bulk crystal. Using a Tescan SEM Vega TS 5130 MM equipped with a silicon drift detector, a composition of $Fe_{4.93(6)}GeTe_{2.00(2)}$ was found. Part of this bulk crystal was used for the SQUID measurements in section 5.2.

The attractive vdW forces between individual layers are much weaker than the covalent bonds within one layer, which makes it possible to separate individual layers from a bulk crystal of Fe_5GeTe_2 following the mechanical exfoliation procedure introduced in section 2.8.5. Thin flakes were exfoliated using a polydimethylsiloxane (PDMS) stamp to transfer a sheet of material from a glass slide onto a silicon substrate with an x-ray transparent Si_3N_4 membrane with a Cu microstrip. The microstrip was patterned by electron beam lithography (EBL) and thermal evaporation, and electrical insulation to the Fe_5GeTe_2 flake was achieved by exfoliation and stamping of an hBN flake between the microstrip and the Fe_5GeTe_2 flake. Another hBN flake was stamped on top to protect the Fe_5GeTe_2

flake from oxidation.

5.2 Static Measurements

SQUID Magnetometry

All SQUID magnetometry measurements are conducted on a piece of the bulk Fe_5GeTe_2 crystal using an MPMS3 SQUID-magnetometer from Quantum Design. It is mounted on a heatable sample holder for temperature dependent measurements in different orientations, either with the field applied in plane ($H \perp c$) or out-of-plane ($H \parallel c$) relative to the vdW layers, as shown in figure 5.1. The magnetic moment was always measured along the same axis as the applied field. To calculate the magnetization M from the measured magnetic moment m using the definition $M = m/V$, the volume V has to be determined. This was achieved by weighing the bulk crystal, and calculating the mass density ρ from the lattice parameters and stoichiometry, which yields a value of $7284\,\mathrm{kg/m^3}$. The volume could then be determined as

$$V = \frac{m_\mathrm{m}}{\rho} = \frac{1.85 \times 10^{-9}\,\mathrm{kg}}{7284\,\mathrm{kg/m^3}} = 2.54 \times 10^{-13}\,\mathrm{m^3},$$

with the weighed mass m_m.

Field cooling and warming

Figure 5.2 shows the result of field cooling (FC) and field warming (FW) measurements, for which the sample was first heated up to a temperature

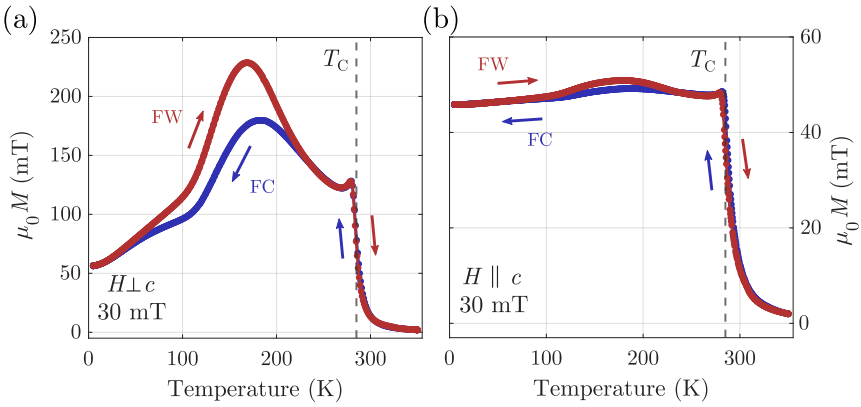

Figure 5.2: Field cooling (FC, blue) and field warming (FW, red) measurements of bulk Fe_5GeTe_2 with the external field applied (a) in-plane and (b) out-of-plane. The arrows indicate the temperature sweep direction, and the dashed line marks the Curie temperature T_C.

of 350 K. Then, a constant magnetic field of 30 mT was applied and the magnetization was measured while cooling the sample down (FC) and then heating it up again (FW). This was done in both in-plane ($H \perp c$) and out-of-plane ($H \parallel c$) geometry, shown in figure 5.2(a) and (b), respectively. From these curves, the Curie temperature T_C can be readily determined by finding the temperature at which the magnetization rapidly drops off, which is also marked by a gray dashed line. This drop-off occurred at a temperature of approximately $T_C = 285$ K, in accordance with literature [162–164]. It can also be seen that for the in-plane measurement in figure 5.2(a), the magnetization drops off for lower temperatures, after reaching a maximum between 170 K and 180 K. Since the saturation magnetization is not expected to decrease for lower temperatures, this indicates that the applied field of 30 mT is not able to saturate the sample in the plane and that an additional temperature dependent out-of-plane anisotropy is present in the sample with increasing effect for lower temperatures. The maximum of the M-T-curves indicates at which temperature this out-of-plane anisotropy

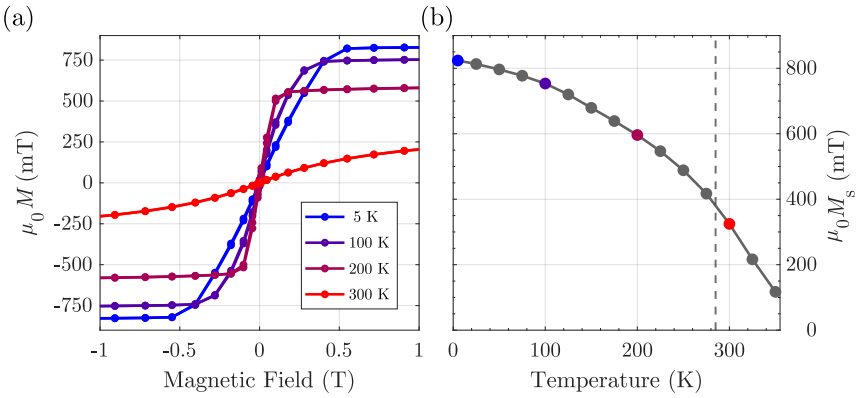

Figure 5.3: Temperature dependent SQUID magnetometry measurements of bulk Fe_5GeTe_2. (a) M-H-curves, measured at different temperatures T with an in-plane configuration. (b) Saturation magnetization M_s as a function of temperature T, with the Curie temperature T_C marked by the gray dashed line and the data points corresponding to the exemplary M-H-curves in (a) are colored accordingly.

might be weakest, namely between 170 K and 180 K. The different position of this maximum for the FC and FW measurements most likely stems from the formation of domains in the material. The out-of-plane measurements in figure 5.2(b) show an almost constant value below T_C, but again with a small maximum between 170 K and 180 K. This can presumably be understood in terms of a slight misalignment of the field and the crystallographic axes.

Temperature dependent M-H-curves

Figure 5.3(a) shows exemplary M-H-curves, measured in an in-plane configuration at different temperatures T. Diamagnetic contributions were subtracted by means of a linear fit to the saturated regime at high fields [1], in this case up to 7 T. It can be seen that the magnetization at high fields

is highest for 5 K and steadily decreases for higher temperatures. At 5 K, the saturation magnetization is measured to be 655 kA/m, corresponding to 823 mT. With the volume of the unit cell $V_{\mathrm{uc}} = 4.15 \times 10^{-28}\,\mathrm{m}^3$, and the number of Fe atoms per unit cell ($N_{\mathrm{Fe}} = 15$), the magnetic moment per Fe atom is determined to be $1.95\,\mu_{\mathrm{B}}$. Interestingly, the field needed to saturate the sample first decreases and then increases with increasing temperature. While the sample at 5 K needed approximately 0.5 T to saturate, only 0.2 T were needed to saturate it at a temperature of 200 K. At 300 K, paramagnetic behavior is observed, with the point of saturation lying outside the shown field range, at a value of approximately 3.5 T. This can be attributed to the transition from ferro- to paramagnetic behavior, as well as change in anisotropy as a function of temperature, which will be discussed in more detail later on. In the previous FC and FW measurements, a field of 30 mT was applied, and the shape of the M-T-curve suggested that the samples was not fully saturated in-plane or out-of-plane, which is confirmed by the M-H-curves in figure 5.3(a).

The major loops were used to determine the saturation magnetization M_{s} as a function of temperature T, which is presented in figure 5.3(b). The temperatures of the exemplary M-H-curves are marked by colored circles. It can be seen that even at temperatures above T_{C}, it was possible to saturate the sample, with the curve following the expected trend of a ferromagnetic sample in an applied magnetic field [56].

Determining magnetic anisotropy

The previous measurements have already hinted at a temperature dependence of the magnetic anisotropy of Fe_5GeTe_2. To quantify this, the anisotropy of bulk Fe_5GeTe_2 was determined by evaluating the M-H-curves for in-plane and out-of-plane orientation and employing the area method

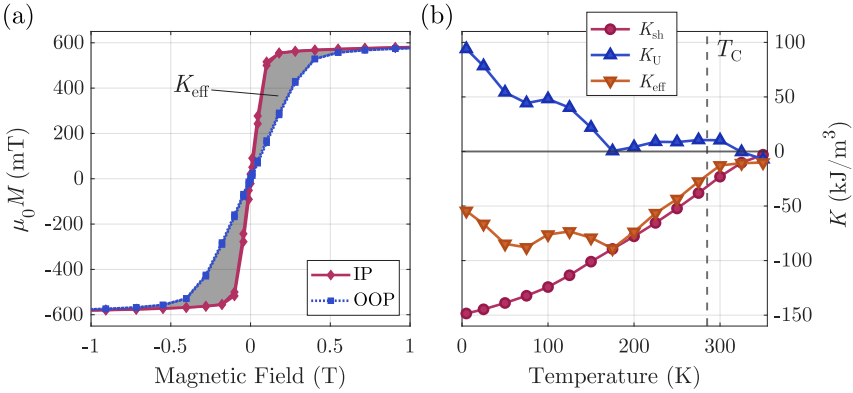

Figure 5.4: (a) Exemplary M-H curves for in-plane (red) and out-of-plane (blue) orientation of the external magnetic field with the enclosed area marked in gray, which is equal to K_{eff}. (b) Anisotropy constants as a function of temperature T. K_{eff} denotes the effective anisotropy constant, determined using the area method, K_{sh} the shape anisotropy, determined from M_{s} and the demagnetization factor. K_{U} is the uniaxial anisotropy constant, which was obtained via $K_{\text{U}} = K_{\text{eff}} - K_{\text{sh}}$. The experimental data points are connected by lines to guide the eye.

introduced in chapter 2.5 [109]. One exemplary measurement of this kind is shown in figure 5.4(a), with the area between the in-plane and out-of-plane measurements marked in gray. This yields an effective anisotropy constant K_{eff}, which includes both shape- and magnetocrystalline anisotropy, both of which were introduced in chapter 1.1.2. From this effective anisotropy, it was possible to get an estimate for the uniaxial anisotropy constant K_{U}, namely by calculating the shape anisotropy K_{sh} and subtracting it from K_{eff}. The energy density associated with the shape anisotropy was approximated by using the previously determined saturation magnetization, shown in figure 5.3(b) and by applying equation (1.11), with the demagnetization factor determined using an approximation for a rectangular rod [61]. The Fe_5GeTe_2 crystal had an aspect ratios of approximately 5:5:1, resulting in a demagnetization factor of $N_{\text{d}} \approx 0.57$. The energy associated with the

shape anisotropy was then calculated via $K_{\mathrm{sh}} = -\mu_0 N_{\mathrm{d}} M_{\mathrm{s}}^2/2$.

The results of this approach are shown in figure 5.4(b), with the shape anisotropy increasing for lower temperature, following the trend of M_{s} shown in figure 5.3(b). The effective anisotropy, as determined by the area method shows a non-monotonic behavior with two local minima at approximately 80 K and 180 K. Interestingly, these two contributions almost cancel out at higher temperatures, resulting in a relatively low uniaxial anisotropy K_{U}. At temperatures below 180 K, K_{U} increases steadily towards lower temperatures.

Static STXM

For the static STXM measurements, an Fe_5GeTe_2 flake of ≈110 nm thickness, determined by AFM, was placed on top of an x-ray transparent Si_3N_4 window and capped with an hBN layer. The magnetization state and domain pattern of the Fe_5GeTe_2 flake was imaged for different external fields and temperatures.

Field Sweep

Figure 5.5 shows exemplary images of this flake at T=40, 140, and 240 K for different external field strengths applied in-plane. It can be seen that at a temperature of 40 K, it is not possible to saturate the sample in-plane with a field of ±250 mT, which is the maximum achievable field strength in the STXM setup. Instead, stripe domains are visible throughout the flake. Shape and size of these domains are not heavily affected by the external field. At $T = 140$ K, it was possible to saturate the flake with a field of −250 mT, while the magnetic contrast was strongly reduced already

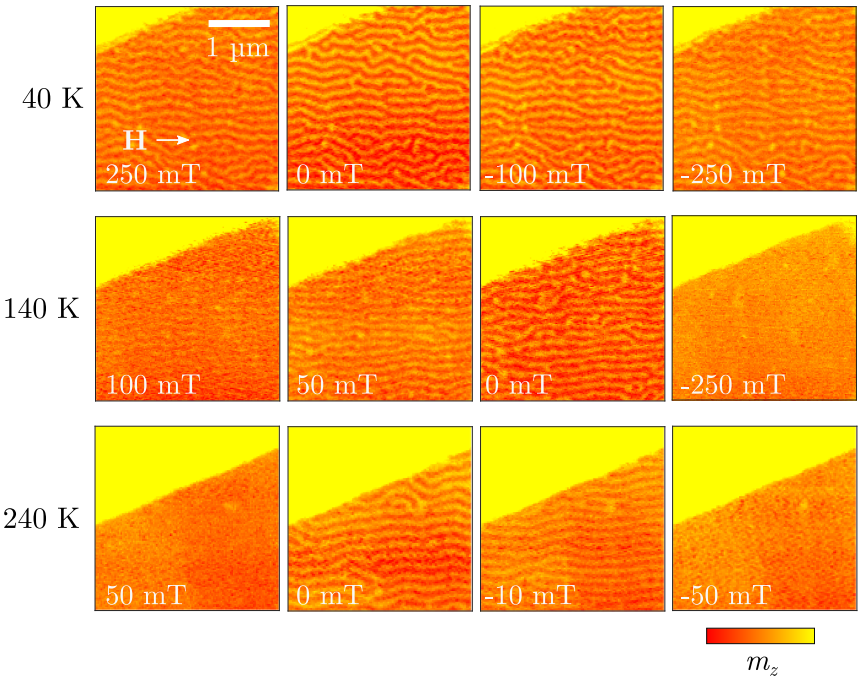

Figure 5.5: Static STXM images of a Fe_5GeTe_2 flake at different temperatures and external fields applied in-plane. From top to bottom, the temperature is increasing, and the field strength is increasing from left to right. Color of the flake indicates the out-of-plane magnetization component m_z.

at 100 mT. This indicates that the domains are oriented out-of-plane at remanence and are already partially aligned with the field, resulting in a smaller projection of the m_z component and therefore smaller XMCD contrast. The last row of figure 5.5 shows images taken at a temperature of 240 K, where the sample already saturates in the external field of ±50 mT. In this case, a field of −10 mT already changes the domain walls shape and size, with the domain wall orientation aligning with the externally applied field. The direction of the positive magnetic field is shown in the

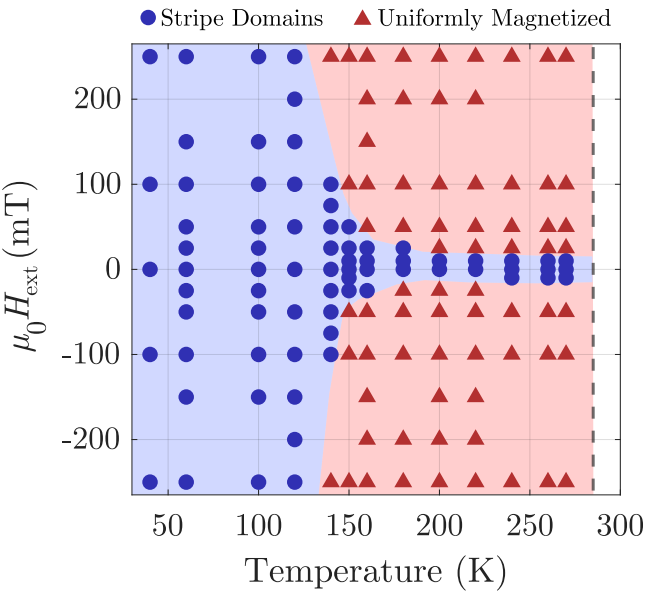

Figure 5.6: In-plane magnetic phase diagram of Fe_5GeTe_2, obtained from static STXM images. Blue circles represent stripe domain states, red triangles uniformly magnetized states. The shaded areas are drawn in to guide the eye. The grey dashed line marks the Curie temperature.

first picture of figure 5.5 and is the same for all images shown there.

Static images have been recorded at several other combinations of temperature and external field, the results of which are condensed in the phase diagram shown in figure 5.6. Due to the relatively large thickness of the flake (110 nm), it is expected that the $M(T)$ behavior matches that of the bulk single crystal, which is confirmed by the static STXM measurements. The blue circles mark the images where the flake was found to be in a stripe domain state, whereas red triangles mark the uniformly magnetized state. The phase diagram shows that for low temperatures, it is not possible to bring the sample into a uniformly magnetized state with the available field strengths. Instead, the sample forms stripe domains that

are in majority aligned with the external field, as was seen in figure 5.5. At temperatures of about 130 K and above, it is possible to uniformly magnetize the sample with the 250 mT field available. The required saturation field strongly decreases as a function of temperature up to the point where the sample can be easily saturated by a field of approximately 25 mT. Overall, this shows that for the TR-STXM measurements on a uniform magnetic background, the temperature has to be sufficiently high, so that the external field can saturate the sample, as it is required for the coherent propagation of spin waves in the flake.

5.3 Spin-Wave Dynamics

A schematic representation of the sample used to perform TR-STXM measurements is shown in figure 5.7. A Fe_5GeTe_2 flake is placed on a Si substrate with an x-ray transparent Si_3N_4 membrane window with a conducting microstrip through which an RF current is flowing. This current induces an Oersted field, indicated by the black loops with arrows. This magnetic field couples to the magnetic moments in the Fe_5GeTe_2 flake and induces precession of the magnetic moments, which propagate through the sample in the form of coherent spin waves, as introduced in section 1.2.3. An external magnetic field $\mathbf{B}$ is applied to align the magnetic moments uniformly, which also determines the type of spin wave that is excited. With the microstrip, as well as the external field parallel to the x-axis, Damon-Eshbach type spin waves are excited, propagating along the y-axis. What is measured in the TR-STXM experiment is the out-of-plane component of the magnetization, m_z, as a function of time.

In the following, if not stated otherwise, the TR-STXM results will be shown for a Fe_5GeTe_2 flake of 28 nm thickness in an external field of 22.5 mT at a temperature of approximately 190 K.

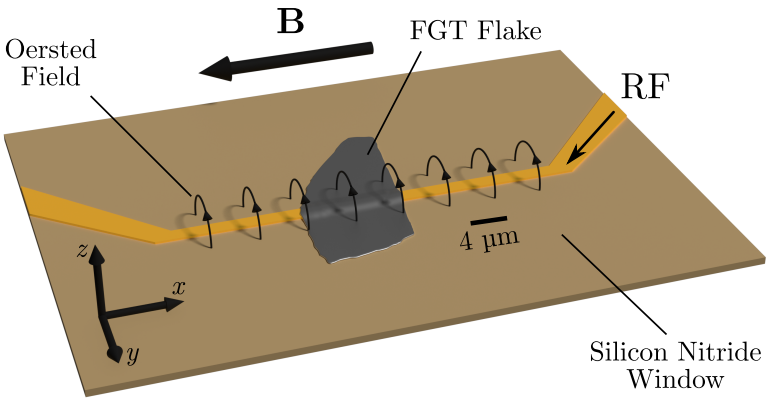

Figure 5.7: Sketch of the basic experimental setup used for the TR-STXM measurements. An RF current is sent through a patterned microstrip, onto which a thin flake of Fe_5GeTe_2 is placed by means of mechanical exfoliation. The alternating Oersted field excites coherent spin-wave dynamics in the Fe_5GeTe_2 flake when an external field **B** is applied.

Choice of energy

To determine the appropriate x-ray energy with highest XMCD contrast, XAS spectra were recorded at a temperature of 100 K with an applied field of ± 250 mT. A static STXM image was taken to confirm that the Fe_5GeTe_2 flake is in a uniformly magnetized state. Figure 5.8 shows the recorded XAS spectra for the two opposite field directions and the difference spectrum. It can be seen that the highest XMCD contrast is obtained at an energy of $\approx$708.8 eV.

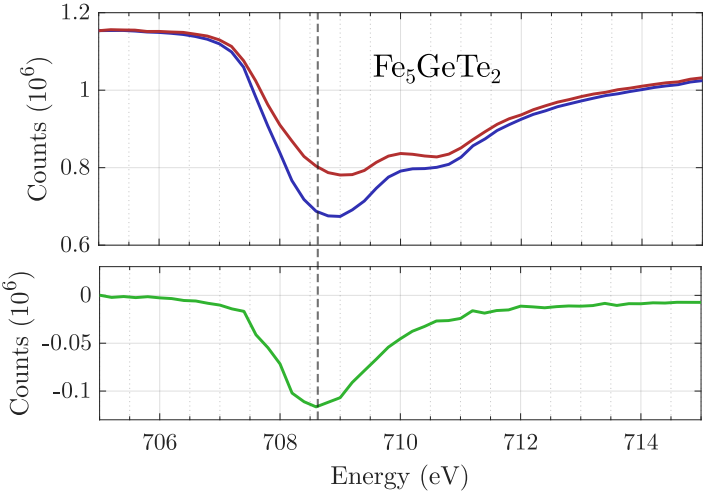

Figure 5.8: XAS (top) and XMCD (bottom) spectra of the Fe_5GeTe_2 flake that was used for the dynamic measurements. Spectra taken near the L_3 edge of Fe by switching the magnetic field direction between parallel (blue) and antiparallel (red) alignment of photon angular momentum and magnetization.

Temperature determination

The sample was cooled down using a cryostate, however, due to Joule heating caused by the RF current running through the microstrip, the nominal value of the cryostate does not reflect the real temperature of the Fe_5GeTe_2 flake, since the temperature sensor is sitting on the sample holder, not on the flake itself. To account for that, the XMCD contrast, which changes as a function of magnetization and therefore temperature, was first measured with the excitation current turned on. This was done for both positive (C^+) and negative (C^-) circular x-ray polarization , and in the case of the TR-STXM measurements of the Damon-Eshbach type

spin-waves, the ratio was calculated as

$$\frac{I(\mathrm{C}^+, T_{\mathrm{set}})}{I(\mathrm{C}^-, T_{\mathrm{set}})} = 0.933.$$

Next, the RF current was turned off and the cryostate was used to slowly increase the temperature of the sample. Since no extra heat is produced at the microstrip, one can assume that the nominal temperature is equal to the real temperature, at least after a certain equilibration time. The cryostate temperature was slowly increased until the XMCD contrast (the previously calculated ratio with the current turned on) was recovered. This was the case when the cryostate was set to a temperature of 190 K, which is therefore the temperature of the flake during the TR-STXM measurements.

Observation of propagating spin waves

According to the methods introduced in sections 2.2 and 2.3, time resolved measurements of the out-of-plane magnetization component m_z were recorded.

Damon-Eshbach - figure 5.9(a) shows a static image of the Fe_5GeTe_2 flake with the microstrip running through its center along the x-axis. Stepwise thickness variations can be seen at the edges of the flake, however, they do not extend far into the flake and therefore do not affect the measurement. The thickness of the flake was additionally estimated by means of x-ray absorption, more precisely by determining the x-ray intensity on the flake (I) and next to it (I_0) and then modeling it using equation (2.4), Beer's law. The absorption coefficient of Fe_5GeTe_2 was estimated using the tools in [88,89], and with that the thickness could be determined to be approximately 28 nm.

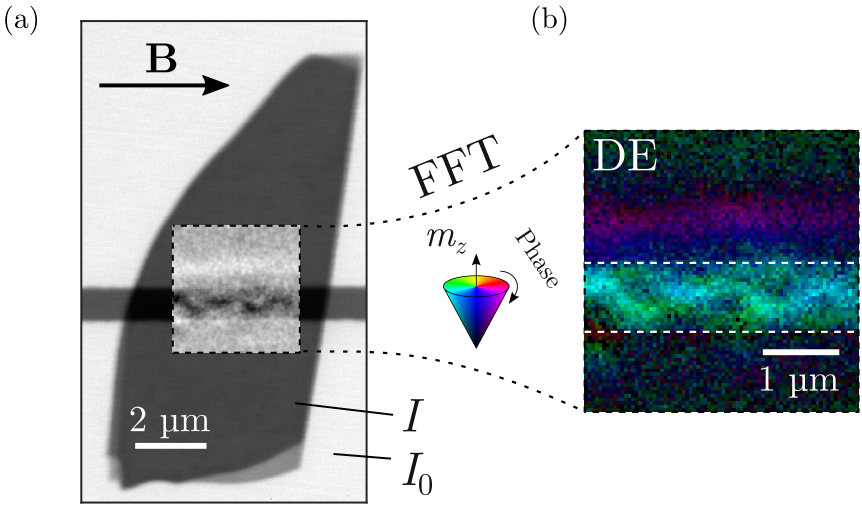

Figure 5.9: (a) Static STXM image of the 28 nm thick Fe_5GeTe_2 flake with the microstrip running horizontally through its center. The inset shows a snapshot of the time-resolved measurement, recorded at a frequency of 3.08 GHz, an applied field of −22.5 mT and a temperature of 190 K. (b) FFT processed, phase resolved image depicting the results of the dynamic measurement. The white dashed lines in (b) mark the microstrip.

The rectangular area at the center of the flake, marked by dashed lines, shows a normalized snapshot of a dynamic measurements performed at an excitation frequency of 3.07 GHz, with the color indicating the normalized out-of-plane magnetization. Using the Fast Fourier Transform (FFT) algorithm introduced in 2.3, the individual frames of the dynamic measurements can be combined to create a single frequency filtered image that also contains the phase information of the measurement and therefore the propagating nature of the spin waves. This kind of information can be visualized using a HSV representation, where the hue (H) depicts the relative phase of a pixel and the brightness or value (V) represents its amplitude. Figure 5.9(b) shows this kind of representation, with the colored cone left of figure 5.9(c) showing how phase and amplitude are

encoded. The Damon-Eshbach type spin waves are clearly visible above of the microstrip, with a continuous phase variation along their propagation direction. Their amplitude quickly decreases, indicating a large damping in the material. This constitutes the first direct observation of coherent spin waves in a 2D magnetic materials with both spatial and phase information. The excitation of DE type spin waves is found to be highly asymmetric, with almost no spin wave signal below the microstrip. This was already observed for the YIG based analog adder in chapter 4 and can be explained in terms of the relative phase between the momentary direction of the magnetic moments underneath the microstrip with respect to the Oersted field.
On top of the microstrip, some inhomogeneities in the dynamic signal can be seen. These most likely stem from magnetic inhomogeneities in the sample due to the split Fe sites, in combination with the strain that the Fe_5GeTe_2 flake experiences when put on top of a 55 nm thick microstrip. To exclude the possibility of backward volume (BV) type spin waves, the inhomogeneities on top the microstrip were compared for different excitation frequencies and showed no frequency dependence whatsoever, making it implausible to stem from a BV type excitation.

Backward volume - figure 5.10(c) shows the results of a dynamic measurement performed on a different flake with a thickness of 50 nm, at a frequency of 3.08 GHz, an external field of −40 mT and a temperature of approximately 250 K. BV type spin waves are observed, which are mainly confined to the microstrip, only slightly advancing into the flake. The emergence of BV type spin waves in DE field geometry has been observed in several other TR-STXM experiments in different materials before[114,149,182], however, the underlying excitation mechanism is not fully understood. For the present case, it is likely that the flake is not in a perfect uniformly magnetized state resulting from temperature variations within the microstrips, flake thickness irregularities and strain, changing the

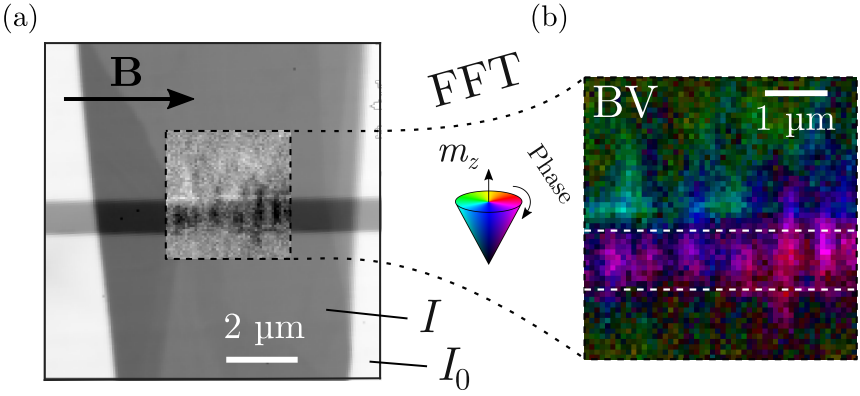

Figure 5.10: (a) Static STXM image of a 50 nm thick Fe_5GeTe_2 flake with the microstrip running horizontally through its center. The inset shows a snapshot of the time-resolved measurement, recorded at a frequency of 3.08 GHz, an applied field of −35 mT, and a temperature of 250 K. (b) FFT processed, phase resolved image depicting the results of the dynamic measurement. The white dashed lines in (b) marks the microstrip.

response to the external magnetic field. These short range local changes in the magnetization landscape can then excite BV waves. The effect is most dominant in the area around the microstrip due to higher temperatures, the large magnitude of the Oersted field, and strain.

Determining the dispersion relation

From the dynamic measurements, it is possible to extract information about the spin-wave dispersion relation. This is done by determining the wavelength of the spin waves for different frequencies. Figure 5.11 shows how this can be done for a single snapshot of the time-resolved measurements, measured at an excitation frequency of 3.84 GHz. The top part shows a snapshot of the TR-STXM measurement, while the bottom part shows a cross section of the normalized signal, averaged along the

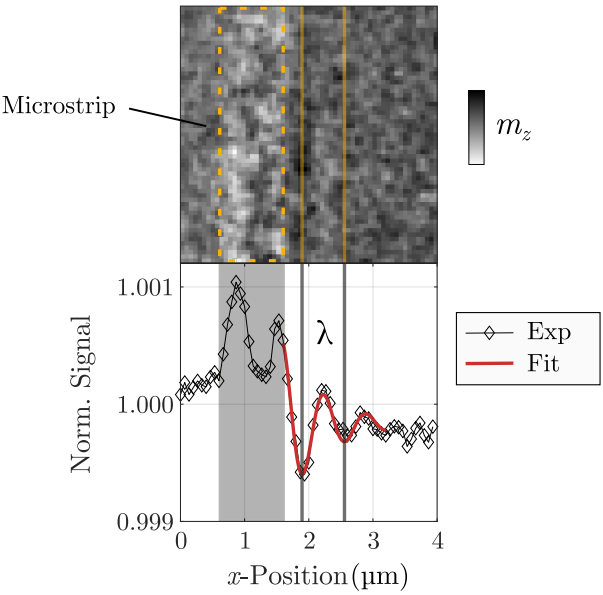

Figure 5.11: Exemplary TR-STXM movie of the 28 nm thick Fe_5GeTe_2 flake (top), recorded at an excitation frequency of 3.84 GHz and a field of −22.5 mT, with the corresponding cross section (bottom), together with a fit (orange line) from which the wavelength and decay length was determined.

direction of the microstrip. The gray area in the cross section indicates the position of the microstrip, while the gray lines indicate the minima of the excited spin wave. These are also marked in the TR-STXM snapshot by the dashed yellow rectangle and the two yellow lines, respectively. To determine both wavelength and decay length of the spin waves, a fit function of the form

$$a \sin(bx + c) \cdot \exp(-dx) + e \tag{5.1}$$

was used to model the experimental data behind the microstrip. The decay length is equal to the distance the wave travels before its amplitude is reduced by a factor of $1/e$. The decay length was determined to be on

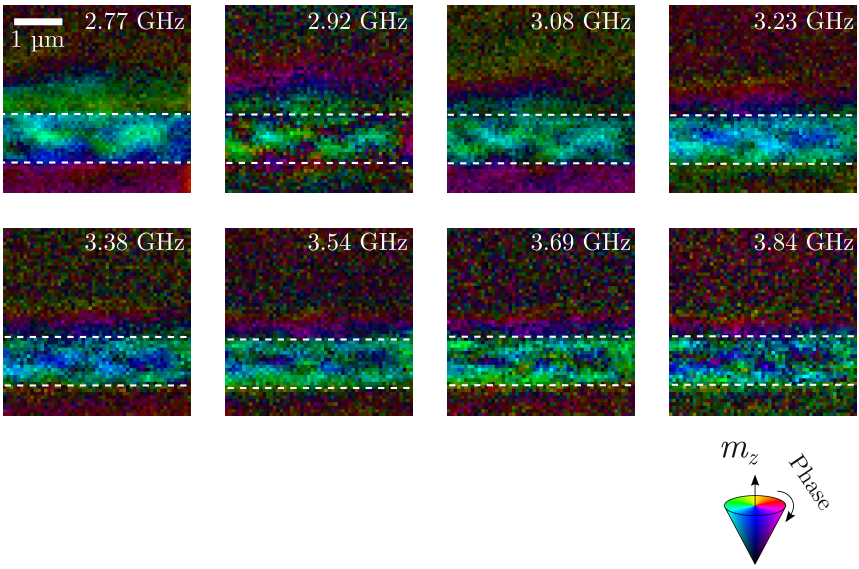

Figure 5.12: Frequency-filtered images of the time-resolved STXM measurements of the 28 nm thick Fe_5GeTe_2 flake for different excitation frequencies f with an applied field of -22.5 mT. Both phase and amplitude are encoded in the color map, according to the cone at the bottom right. The white dashed lines mark the position of the microstrip.

the order of 0.6 µm in the case of 3.84 GHz. Compared to other magnonic materials, such as $Ni_{80}Fe_{20}$ and yttrium iron garnet (YIG), where spin waves can travel on the order of 10 µm and 100 µm, respectively, Fe_5GeTe_2 shows a very high damping. This is in accordance with the Gilbert damping parameter α of the respective materials, 7×10^{-3} for Py [71], 1×10^{-4} for YIG [72], and 3×10^{-2} for Fe_5GeTe_2 [164]. It was not possible to use this fit function for every data point, as it relies on a good signal to noise ratio. Instead, the wavelength was then determined manually by looking at the cross-section at different frames of the TR-STXM measurement.

Figure 5.12 shows frequency filtered representations of the TR-STXM measurements for different excitation frequencies. These were used to

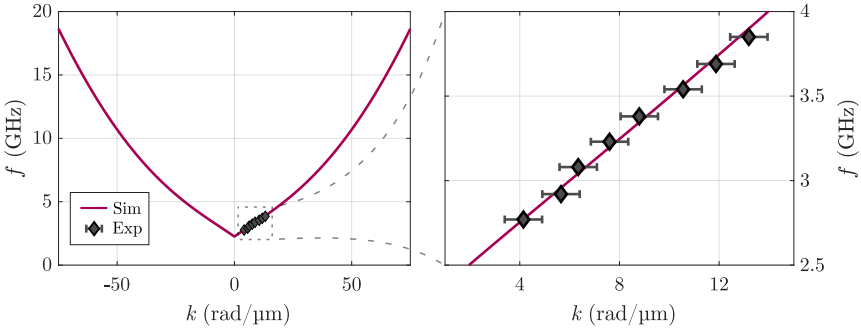

Figure 5.13: (a) Experimentally determined points of the dispersion relation (gray diamonds) together with the simulation results using a multilayer approach (purple line) with a (b) zoom into the experimentally relevant range, with the smallest and largest k vector corresponding to wavelengths of 1.5 µm and 0.5 µm, respectively.

extract the wavelength and obtain information on the spin-wave dispersion relation. The images show that the wavefront above the microstrip is not homogeneous, especially for long wavelengths. This is most likely due to inhomogeneities in the sample and makes determining the wavelength more difficult. Another striking feature is that the irregularities on top of the microstrip look very similar for each measurement, not showing any frequency dependence, and thus ruling out the possibility of it arising from some kind of backward volume type excitation.

5.4 Simulations

5.4.1 Fitting the dispersion relation

The multilayer approach introduced in section 2.10 can be used to model the dispersion relation of the Fe_5GeTe_2 flake, and the results are shown

in figure 5.13. Figure 5.13(a) shows the frequency f as a function of spin-wave k-vector, with the gray diamonds representing the experimental data, and the purple line the best fit obtained from calculations based on the multilayer model[55]. The following parameters were used for the calculation of the dispersion relation:
$M_s = 210\,\mathrm{kA/m}$, $A_{ex} = 9\,\mathrm{pJ/m}$, $B_{ext} = 22.5\,\mathrm{mT}$, $H_{aniso} = 1.6\,\mathrm{kA/m}$, $J_{inter} = 16\,\mathrm{mJ/m^2}$, and a thickness of 28 nm, divided into 29 layers with a gap of 0.309 nm. The experimental data points show a linear trend, as can be seen more clearly in figure 5.13(b), however, for larger values of k, it shows quadratic behavior. This is in contrast to the classic Damon-Eshbach type dispersion relation shown in figure 1.5, where after an initial steep increase at low k, the slope decreases for intermediate values of k before finally showing quadratic behavior for large values of k. These three regimes arise from the interplay of dipolar and exchange interaction, dominating spin waves with very long and very short wavelengths respectively. The intermediate regime arises when dipolar and exchange interaction are of similar strength. To understand the behavior in the case of Fe_5GeTe_2, calculations based on the multilayer approach were performed for different values of the saturation magnetization M_s, which are shown in figure 5.14 and 5.15.

5.4.2 M_s variation

In figure 5.14(a), the dispersion relations calculated for different values of M_s are shown. All other simulation parameters are kept constant. It can be seen that for a very low saturation magnetization (50 kA/m), the entire dispersion relation is dominated by exchange and shows a quadratic behavior over the whole k range.
In case of a high saturation magnetization (650 kA/m), the typical Damon-Eshbach type behavior is observed. For the two curves with intermediate

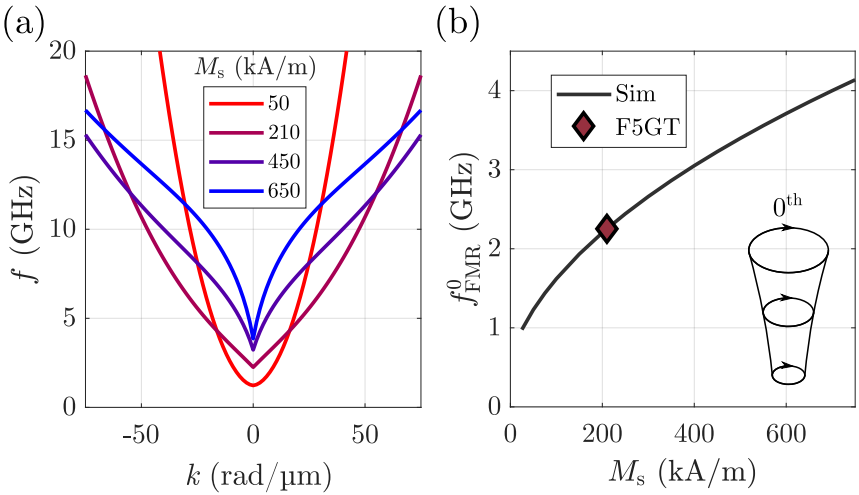

Figure 5.14: (a) Simulated dispersion relation of the 0^{th} order mode for different values of the saturation magnetization M_s, (b) FMR frequency of the 0^{th} order mode as a function of M_s. A sketch of the mode profile of the 0^{th} order mode can be seen in the inset of (b).

values of M_s (210 kA/m, 450 kA/m), the onset of the quadratic behavior shifts towards lower values of k for reduced saturation, while the initial slope is decreased.

Fe_5GeTe_2, with a saturation magnetization of approximately 210 kA/m, represents such an intermediate case, with hardly any initial slope and an early quadratic onset. All curves were calculated for the 0^{th} order mode, with a mode profile that decreases in amplitude when going deeper into the film, as is illustrated in the inset of figure 5.14(b).

Figure 5.14(b) shows the FMR frequency of the 0^{th} order mode as a function of saturation magnetization, which exhibits an initial steep increase at very low values of M_s. When further increasing the saturation magnetization, the FMR frequency increases at an ever decreasing rate. This can be understood in terms of the Kittel formula found in equation (2.8) for a fixed field and changing saturation magnetization, which leads to this

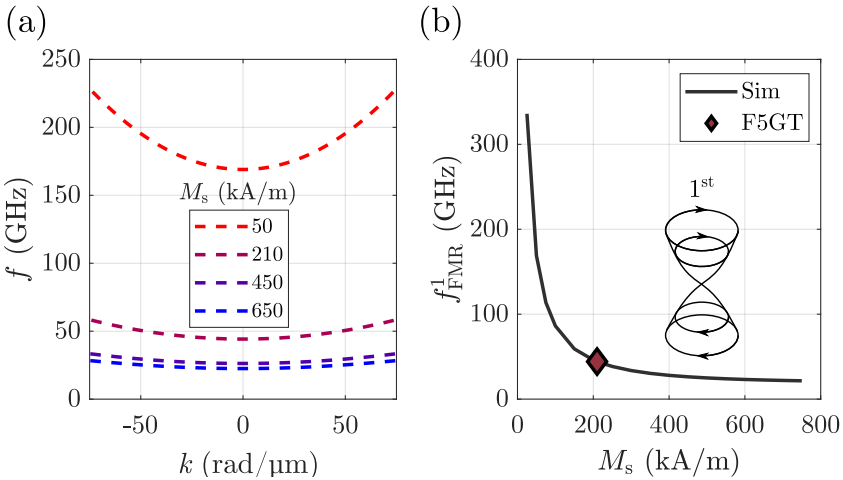

Figure 5.15: (a) Simulated dispersion relation of the 1st higher order mode for different values of the saturation magnetization M_s, (b) FMR frequency of the 1st higher order mode as a function of M_s. A sketch of the mode profile of the 1st higher order mode can be seen in the inset of (b).

kind of behavior.

5.4.3 Higher order modes

Higher order Damon-Eshbach spin waves, as introduced in section 1.2 and shown schematically in figure 1.4 can also be excited in magnetic thin films. An aspect unique to 2D magnetic materials is the anisotropic coupling of magnetic moments. While most common materials used throughout magnonics research exhibit more or less isotropic exchange, 2D magnetic materials can have very different coupling strengths for intra- and interlayer coupling, which is also shown in figure 5.1. The interlayer coupling strongly depends on the gap width and type of stacking, and can even be tuned in

vdW heterostructures[37]. To understand how these higher order modes behave in a vdW material, the multilayer model was employed to calculate the spin-wave dispersion relation for different values of M_s and J_{inter}. While these modes are usually not accessible in TR-STXM measurements due to their high frequencies of 60 GHz and above, they can be accessed in FMR experiments, which have been planned for the Fe_5GeTe_2 samples but were not carried out at the time of writing this thesis.

M_s dependence

Figure 5.15(a) shows the dispersion relation of the 1st higher order mode for different values of M_s. It can be seen again that the quadratic behavior is more pronounced for lower saturation magnetization, however, the typical Damon-Eshbach type trend is not observed for this mode. An additional sketch of how the mode profile looks is shown in the inset of figure 5.15(b).

Figure 5.15(b) again shows the FMR frequency as a function of the saturation magnetization, in this case for the 1st higher order mode. This time, an opposite trend is observed, with the FMR frequency decreasing for higher values of M_s. For very small saturation magnetization, the FMR frequency increases drastically and seems to diverge. This stems from the definition of the effective field caused by the interlayer coupling, which scales with $1/M_s$[55] and therefore diverges for very small values of the saturation magnetization.

With its Curie temperature at approximately 285 K in bulk, as was determined from SQUID measurements, Fe_5GeTe_2 will show significant changes of M_s at different temperatures[56]. This means that the dispersion relation will be sensitive to a change in temperature, and so precise control of the temperature in potential future devices is of great importance. On the other hand, this opens up the possibility of tuning the magnonic properties by means of temperature control. While other properties will also depend

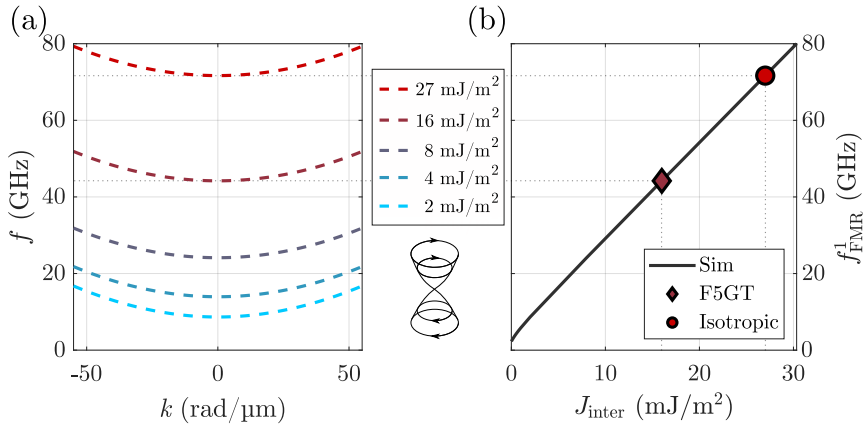

Figure 5.16: (a) Simulated dispersion relation of the 1$^{\mathrm{st}}$ order mode for different values of the interlayer coupling constant J_{inter}. (b) FMR frequency of the 1$^{\mathrm{st}}$ order mode as a function of J_{inter}. A sketch of the mode profile of the 1$^{\mathrm{st}}$ order mode is shown at the center.

on temperature, such as exchange stiffness and anisotropies, the main contribution to the dispersion relation will come from the change in M_{s} since dipolar interaction goes with M_{s}^2 [1]. A sketch of the mode profile of the 1$^{\mathrm{st}}$ higher order mode can be seen at the center.

J_{inter} dependence

While the 0$^{\mathrm{th}}$ order mode is not significantly influenced by the value of J_{inter}, the 1$^{\mathrm{st}}$ higher order mode is very sensitive to it. This can be seen in figure 5.16(a), where the dispersion relation for different values of J_{inter} are shown. The shape is not changed significantly, however, a higher interlayer coupling will result in a shift towards higher frequencies of the 1$^{\mathrm{st}}$ order mode. This can be understood by looking at the mode profile at the center of figure 5.16, or the one shown in figure 1.4(d). The interlayer coupling

wants to align the individual layers, however, it can be seen that the layers above and below the node have a 180° phase shift, which results in a slight misalignment. The energy associated with this misalignment depends on J_{inter} and results in higher energies and therefore higher frequencies when J_{inter} is increased.

Figure 5.16(b) shows the FMR frequency of the 1$^{\text{st}}$ higher order mode as a function of interlayer exchange constant J_{inter}, where a linear trend is observed. The two markers show a guess for Fe_5GeTe_2 (purple diamond), estimated using the results of ab initio calculations of exchange constants between all Fe sites across one layer in Fe_3GeTe_2 [183]. Additionally, the isotropic case is shown (red circle), where the interlayer is chosen so that its strength is equal to the intralayer exchange stiffness. Compared to the isotropic case, the estimate for Fe_5GeTe_2 shows a 43 % decrease in J_{inter}.

5.5 Conclusion

Overall, this study constitutes the first measurement of propagating spin waves in a 2D magnetic material, Fe_5GeTe_2, with both spatial and temporal resolution. First, the material was characterized using SQUID magnetometry and STXM imaging. The results were used to determine the materials Curie temperature and anisotropy, which was used to find suitable parameters for the TR-STXM measurements. These showed that both Damon-Eshbach and backward volume type spin waves can be excited in Fe_5GeTe_2 flakes by means of coupling of magnetic moments to the Oersted field of a microstrip antenna. Dynamic measurements were performed at different external fields and excitation frequencies resulting in spin-wave movies that show coherent spin waves propagating through the material. The observed decay length of 0.6 µm is very low compared to other materials used throughout magnonics, indicating that Fe_5GeTe_2, especially in the

form of exfoliated flakes, might not be a suitable material for magnonics research due to its high damping. The dynamic measurements were also used to determine the spin-wave wavelength as a function of frequency, which could be compared to a semi-analytical multilayer model in order to obtain information on the magnetic properties of Fe_5GeTe_2 and understand the dispersion relations peculiar shape. The model was also used to study the dependence of the dispersion relation on saturation magnetization and interlayer coupling strength, giving insight into how these properties affect the propagation of spin waves at different wavelengths. This opens up the possibility of tailoring the spin-wave dispersion relation to potential technological applications by means of temperature control and different material stacks in vdW heterostructures. Future work could experimentally investigate spin-wave propagation in these heterostructures, which introduces many more degrees of freedom to manipulate the systems magnonic properties.

Part IV

Summary & Outlook

Summary

This thesis contains the results of three different studies, all related to the analysis of magnonic systems with regards to their basic properties, but also potential technological applications. It covers the examination of structural and magnetic properties of $Ni_{80}Fe_{20}$ thin films exposed to high temperatures, an experimental demonstration of a magnonic analog adder, and the study of magnetization dynamics in the two dimensional (2D) van der Waals (vdW) magnet Fe_5GeTe_2 with the first visualization of spin waves. The main experimental methods used in these investigations are ferromagnetic resonance (FMR), transmission electron microscopy (TEM) with energy-dispersive x-ray spectroscopy (EDX), and magnetic scanning transmission x-ray microscopy (STXM).

The first study focused on 36 nm thick polycrystalline $Ni_{80}Fe_{20}$ films and how prolonged exposure to high temperatures up to 350 °C affects their magnonic properties due to structural changes. A $Ni_{80}Fe_{20}$ layer was deposited on a single Si substrate using magnetron sputtering, which was subsequently cut into smaller pieces. The pristine films were studied using vector network analyzer ferromagnetic resonance (VNA-FMR) with fixed magnetic fields and varying excitation frequency. Each of the pieces was then exposed to a different temperature up to 350 °C in a vacuum oven for one hour, after which the VNA-FMR analysis was repeated. These measurements yielded information on the effective saturation magnetization, Gilbert damping parameter, and gyromagnetic ratio. It was found that all magnetic properties are stable up to a temperature of 200 °C, for higher temperatures the samples underwent irreversible changes. At an annealing temperature of 300 °C, the saturation magnetization decreased by more than 15 %, while the g-factor and damping increased by 10 % and 350 %, respectively.

These effects were even more pronounced at an annealing temperature of 350 °C, for which a more than sixfold increase of the Gilbert damping parameter was found. The origin of this phenomenon was investigated by TEM measurements of thin lamellas cut out of the samples using a focused ion beam (FIB) setup. EDX gave additional insight into the change of elemental depth profiles. It was found that at an annealing temperature of 300 °C, the $Ni_{80}Fe_{20}$ layer shrinks due to Ni atoms migrating into the Si layer, forming non-magnetic nickel silicides. This process was accompanied by grain growth within the $Ni_{80}Fe_{20}$ layer, an effect that was most pronounced in the sample annealed at 350 °C. This provided a link between the changes in magnetic properties and the structural changes in the thin film system, demonstrating that high temperatures in spintronic devices could potentially lead to irreversible changes, even when the temperature is below the eutectic temperature of the system. However, these observations open an avenue for non-lithographic design of magnetization landscapes, e.g. by local laser heating.

The aim of the second study was the experimental realization of a magnonic analog adder, where spin-wave interference was used to perform analog addition operations. Two different kinds of devices were fabricated, consisting of polycrystalline $Ni_{80}Fe_{20}$ and the ferrimagnetic insulator yttrium iron garnet (YIG). Electron beam lithography, magnetron sputtering and thermal evaporation were used to pattern two microstrips for the excitation of coherent spin waves. The interference was then directly observed by means of time-resolved scanning transmission x-ray microscopy (TR-STXM), giving insight into the underlying working principle and functionality. After initial device characterizations, the relative phase between the excitation of the first and second microstrip was varied. This resulted in different interference patterns, from constructive to complete destructive interference. This was quantified and compared to theoretical predictions with excellent agreement in both devices. The performance of the analog

adder was tested by evaluating the resulting spin-wave amplitude for constructive interference of spin waves with different combination of excitation strengths. The commutative property, as well as the general functionality of the addition operation were shown by quantitatively analyzing the resulting spin-wave amplitude as a function of the sum of input powers. Due to the relatively high damping in $Ni_{80}Fe_{20}$, this was only possible in the YIG based device, where an agreement within an error margin of only 2 % was found. The multiplexing capabilities of the analog adder were demonstrated by excitation of multiple frequencies at once and subsequent decomposition of the resulting spin-wave signal into its frequency components. Overall, this demonstrates the feasibility of a magnonic analog adder device based on spin-wave interference.

The last study investigated magnetization dynamics in a 2D magnetic material. A 28 nm thick flake of Fe_5GeTe_2 was placed on a Si substrate with an x-ray transparent Si_3N_4 membrane window by mechanical exfoliation using a polydimethylsiloxane (PDMS) stamp. Spin dynamics were excited using a Cu microstrip antenna, prepared by electron beam lithography and thermal evaporation. The spin wave characteristics were directly visualized for the first time using TR-STXM, with a cryostate to allow for control of the sample temperature. Both Damon-Eshbach and backward volume type spin waves were detected at different externally applied fields and excitation frequencies. Extremely high damping and a short decay length of less than 1 µm was observed. Wavelengths of the Damon-Eshbach type spin waves were determined at one temperature to obtain information on the dispersion relation of Fe_5GeTe_2, which showed a linear trend in a frequency range between 2.5 GHz and 4 GHz. These results were then compared to a theoretical multilayer model based on a dynamic matrix approach, making it possible to calculate the system's dispersion relation much quicker compared to conventional micromagnetic simulations. This theoretical approach showed excellent agreement with the experimental

findings in the investigated frequency range. The shape of the dispersion relation of Fe_5GeTe_2 was found to show characteristics between a purely exchange dominated and a purely dipolar dominated state. The model was then used to study the dependence of the dispersion relation on the saturation magnetization and interlayer coupling strength, demonstrating their effect on spin-wave dynamics in this type of magnetic material. In principle, this could also be used to control and tailor the spin-wave properties of a 2D magnet by means of temperature control and stacking in vdW heterostructures.

Outlook

The presented results gave novel insights for a better understanding of magnonic systems and the obstacles encountered in this relatively young research field. The study on the annealing of $Ni_{80}Fe_{20}$ thin films showed how prolonged exposure to high temperatures can have detrimental effects on magnonic devices based on $Ni_{80}Fe_{20}$, one of the most common materials in magnonic research due to its low damping and straightforward fabrication. This presents a starting point to study the effect on other material combinations used throughout spintronics and magnonics. The comparison between different materials can give insight into the associated damping mechanisms, which are still poorly understood in real systems. Future experiments could also explore the possibility of introducing additional buffer layers to prevent the observed irreversible structural changes. Additionally, the seemingly unfavorable effects observed, namely the decrease of saturation magnetization and increase of damping, could be intentionally used to ones advantage. A laser can be used to locally heat up the sample, making it in principle possible to create intricate magnetic landscapes, which could be used for example in magnonic crystals or to create spin-wave waveguides

without the need for lithography.

The work on the magnonic analog adder showed the feasibility of a spin-wave interference based device to perform basic addition operations and the possibility of precise control of this interference in the linear regime. Future studies could try to investigate the nonlinear regime, which is necessary for neuromorphic computing and machine learning tasks such as pattern recognition. While YIG proved to be an optimal material for the analog adder prototype, solving the problems of YIG microstructuring and integration is still a long way off. Another major hurdle is finding a more efficient mechanism for spin-wave excitation to actually benefit from the dissipationless propagation of spin waves, especially in densely packed integrated circuits. Also, to allow for compatibility with other electronic circuits and CMOS technology in general, electrical readout of the spin-wave intensity using a third microstrip or a properly placed GMR/TMR sensor should be another goal to push this kind of device closer to technological applications.

The direct observation of propagating spin waves in Fe_5GeTe_2 demonstrated potential difficulties of using vdW magnetic materials for magnonic applications. One aspect of this is their Curie temperature, which is already relatively low and is easily exceeded in magnonic applications due to the involved high current densities. Strain and mechanical stress introduced by the exfoliation of thin flakes can impede spin-wave propagation, resulting in a high damping and low decay lengths. These effects could however be reduced by stacking of different vdW materials with suitable properties in vdW heterostructures. Calculations based on a multilayer model gave insight into the underlying physics and highlighted the possibility of tweaking the dispersion relation by means of changing the interlayer coupling strength. Based on this knowledge, future studies could try to explore the dynamics of higher order spin-wave modes in weakly coupled

magnetic vdW materials in order to exploit spin-wave dynamics in vdW heterostructures at higher frequencies up to 100 GHz, which may become technologically relevant in the future.

Bibliography

[1] J. Stöhr and H. C. Siegmann. *Magnetism: From fundamentals to nanoscale dynamics*, volume 152. Springer, 2006.

[2] W. Lowrie and A. Fichtner. *Fundamentals of geophysics*. Cambridge university press, 2020.

[3] J. C. Maxwell. VIII. A dynamical theory of the electromagnetic field. *Philosophical transactions of the Royal Society of London*, 155:459–512, 1865.

[4] I. Žutić, J. Fabian, and S. D. Sarma. Spintronics: Fundamentals and applications. *Reviews of modern physics*, 76(2):323, 2004.

[5] J. Fabian, A. Matos-Abiague, C. Ertler, P. Stano, and I. Žutić. Semiconductor spintronics. *Acta Physica Slovaca. Reviews and Tutorials*, 57(4-5), aug 2007.

[6] S. D. Bader and S. S. P. Parkin. Spintronics. *Annual Review of Condensed Matter Physics*, 1(1):71–88, 2010.

[7] T. Jungwirth, X. Marti, P. Wadley, and J. Wunderlich. Antiferromagnetic spintronics. *Nature Nanotechnology*, 11(3):231–241, 2016.

[8] S. Neusser and D. Grundler. Magnonics: Spin Waves on the Nanoscale. *Advanced Materials*, 21(28):2927–2932, 2009.

[9] V. V. Kruglyak, S. O. Demokritov, and D. Grundler. Magnonics. *Journal of Physics D: Applied Physics*, 43(26):264001, jun 2010.

[10] B. Lenk, H. Ulrichs, F. Garbs, and M. Münzenberg. The building blocks of magnonics. *Physics Reports*, 507(4):107–136, 2011.

[11] A. Barman, G. Gubbiotti, S. Ladak, A. O. Adeyeye, M. Krawczyk, J. Gräfe, C. Adelmann, S. Cotofana, A. Naeemi, V. I. Vasyuchka, and Others. The 2021 magnonics roadmap. *Journal of Physics: Condensed Matter*, 33(41):413001, 2021.

[12] M. P. Kostylev, A. A. Serga, T. Schneider, B. Leven, and B. Hillebrands. Spin-wave logical gates. *Applied Physics Letters*, 87(15):153501, 2005.

[13] A. Khitun and K. L. Wang. Non-volatile magnonic logic circuits engineering. *Journal of Applied Physics*, 110(3):34306, 2011.

[14] G. Talmelli, T. Devolder, N. Träger, J. Förster, S. Wintz, M. Weigand, H. Stoll, M. Heyns, G. Schütz, I. P. Radu, J. Gräfe, F. Ciubotaru, and C. Adelmann. Reconfigurable submicrometer spin-wave majority gate with electrical transducers. *Science Advances*, 6(51):eabb4042, 2020.

[15] A. V. Chumak, A. A. Serga, and B. Hillebrands. Magnon transistor for all-magnon data processing. *Nature Communications*, 5(1):4700, 2014.

[16] Q. Wang, M. Kewenig, M. Schneider, R. Verba, F. Kohl, B. Heinz, M. Geilen, M. Mohseni, B. Lägel, F. Ciubotaru, C. Adelmann, C. Dubs, S. D. Cotofana, O. V. Dobrovolskiy, T. Brächer, P. Pirro, and A. V. Chumak. A magnonic directional coupler for integrated magnonic half-adders. *Nature Electronics*, 3(12):765–774, 2020.

[17] P. Röschmann. YIG filters. *Philips Tech. Rev*, 32(9):322–327, 1971.

[18] H. Merbouche, M. Collet, M. Evelt, V. E. Demidov, J. L. Prieto, M. Muñoz, J. Ben Youssef, G. de Loubens, O. Klein, S. Xavier, O. D'Allivy Kelly, P. Bortolotti, V. Cros, A. Anane, and S. O. Demokritov. Frequency Filtering with a Magnonic Crystal Based on Nanometer-Thick Yttrium Iron Garnet Films. *ACS Applied Nano Materials*, 4(1):121–128, 2021.

[19] O. Dzyapko, I. Lisenkov, P. Nowik-Boltyk, V. E. Demidov, S. O. Demokritov, B. Koene, A. Kirilyuk, T. Rasing, V. Tiberkevich, and A. Slavin. Magnon-magnon interactions in a room-temperature magnonic Bose-Einstein condensate. *Phys. Rev. B*, 96(6):64438, aug 2017.

[20] B. Divinskiy, H. Merbouche, V. E. Demidov, K. O. Nikolaev, L. Soumah, D. Gouéré, R. Lebrun, V. Cros, J. B. Youssef, P. Bortolotti, A. Anane, and S. O. Demokritov. Evidence for spin current driven Bose-Einstein condensation of magnons. *Nature Communications*, 12(1):6541, 2021.

[21] N. Träger, P. Gruszecki, F. Lisiecki, F. Groß, J. Förster, M. Weigand, H. Glowinski, P. Kuswik, J. Dubowik, G. Schütz, M. Krawczyk, and J. Gräfe. Real-Space Observation of Magnon Interaction with Driven Space-Time Crystals. *Phys. Rev. Lett.*, 126(5):57201, feb 2021.

[22] S. O. Demokritov, A. A. Serga, A. André, V. E. Demidov, M. P. Kostylev, B. Hillebrands, and A. N. Slavin. Tunneling of Dipolar Spin Waves through a Region of Inhomogeneous Magnetic Field. *Phys. Rev. Lett.*, 93(4):47201, 2004.

[23] M. Krawczyk and H. Puszkarski. Plane-wave theory of three-dimensional magnonic crystals. *Phys. Rev. B*, 77(5):54437, feb 2008.

[24] A. V. Chumak, T. Neumann, A. A. Serga, B. Hillebrands, and M. P. Kostylev. A current-controlled, dynamic magnonic crystal. *Journal of Physics D: Applied Physics*, 42(20):205005, sep 2009.

[25] A. V. Chumak, A. A. Serga, and B. Hillebrands. Magnonic crystals for data processing. *Journal of Physics D: Applied Physics*, 50(24):244001, may 2017.

[26] J. Grollier, D. Querlioz, K. Y. Camsari, K. Everschor-Sitte, S. Fukami, and M. D. Stiles. Neuromorphic spintronics. *Nature Electronics*, 3(7):360–370, 2020.

[27] A. Kurenkov, S. Fukami, and H. Ohno. Neuromorphic computing with antiferromagnetic spintronics. *Journal of Applied Physics*, 128(1):10902, 2020.

[28] M. Zahedinejad, A. A. Awad, S. Muralidhar, R. Khymyn, H. Fulara, H. Mazraati, M. Dvornik, and J. Åkerman. Two-dimensional mutually synchronized spin Hall nano-oscillator arrays for neuromorphic computing. *Nature Nanotechnology*, 15(1):47–52, 2020.

[29] K. Roy, A. Jaiswal, and P. Panda. Towards spike-based machine intelligence with neuromorphic computing. *Nature*, 575(7784):607–617, 2019.

[30] V. Milo, G. Malavena, C. Monzio Compagnoni, and D. Ielmini. Memristive and CMOS Devices for Neuromorphic Computing. *Materials*, 13(1), 2020.

[31] G. W. Burr, R. M. Shelby, A. Sebastian, S. Kim, S. Kim, S. Sidler, K. Virwani, M. Ishii, P. Narayanan, A. Fumarola, L. L. Sanches, I. Boybat, M. L. Gallo, K. Moon, J. Woo, H. Hwang, and Y. Leblebici. Neuromorphic computing using non-volatile memory. *Advances in Physics: X*, 2(1):89–124, 2017.

[32] D. Marković, A. Mizrahi, D. Querlioz, and J. Grollier. Physics for neuromorphic computing. *Nature Reviews Physics*, 2(9):499–510, 2020.

[33] W. Haensch, T. Gokmen, and R. Puri. The Next Generation of Deep Learning Hardware: Analog Computing. *Proceedings of the IEEE*, 107(1):108–122, 2019.

[34] C. Mack. *Fundamental Principles of Optical Lithography*. John Wiley & Sons, Ltd, 2007.

[35] Y. Chen. Nanofabrication by electron beam lithography and its applications: A review. *Microelectronic Engineering*, 135:57–72, 2015.

[36] L. A. Ponomarenko, A. K. Geim, A. A. Zhukov, R. Jalil, S. V. Morozov, K. S. Novoselov, I. V. Grigorieva, E. H. Hill, V. V. Cheianov, V. I. Fal'ko, K. Watanabe, T. Taniguchi, and R. V. Gorbachev. Tunable metal–insulator transition in double-layer graphene heterostructures. *Nature Physics*, 7(12):958–961, 2011.

[37] A. K. Geim and I. V. Grigorieva. Van der Waals heterostructures. *Nature*, 499(7459):419–425, 2013.

[38] K. S. Novoselov, A. K. Geim, S. V. Morozov, D. Jiang, Y. Zhang, S. V. Dubonos, I. V. Grigorieva, and A. A. Firsov. Electric Field Effect in Atomically Thin Carbon Films. *Science*, 306(5696):666–669, 2004.

[39] A. H. Castro Neto, F. Guinea, N. M. Peres, K. S. Novoselov, and A. K. Geim. The electronic properties of graphene. *Reviews of Modern Physics*, 81(1):109–162, 2009.

[40] C. Gong, L. Li, Z. Li, H. Ji, A. Stern, Y. Xia, T. Cao, W. Bao, C. Wang, Y. Wang, Z. Q. Qiu, R. J. Cava, S. G. Louie, J. Xia, and

X. Zhang. Discovery of intrinsic ferromagnetism in two-dimensional van der Waals crystals. *Nature*, 546(7657):265–269, 2017.

[41] J.-U. Lee, S. Lee, J. H. Ryoo, S. Kang, T. Y. Kim, P. Kim, C.-H. Park, J.-G. Park, and H. Cheong. Ising-Type Magnetic Ordering in Atomically Thin FePS3. *Nano Letters*, 16(12):7433–7438, dec 2016.

[42] X. Wang, K. Du, Y. Y. F. Liu, P. Hu, J. Zhang, Q. Zhang, M. H. S. Owen, X. Lu, C. K. Gan, P. Sengupta, C. Kloc, and Q. Xiong. Raman spectroscopy of atomically thin two-dimensional magnetic iron phosphorus trisulfide (FePS3) crystals. *2D Materials*, 3(3):31009, sep 2016.

[43] K. S. Burch, D. Mandrus, and J.-G. Park. Magnetism in two-dimensional van der Waals materials. *Nature*, 563(7729):47–52, 2018.

[44] B. Huang, G. Clark, E. Navarro-Moratalla, D. R. Klein, R. Cheng, K. L. Seyler, D. Zhong, E. Schmidgall, M. A. McGuire, D. H. Cobden, W. Yao, D. Xiao, P. Jarillo-Herrero, and X. Xu. Layer-dependent ferromagnetism in a van der Waals crystal down to the monolayer limit. *Nature*, 546(7657):270–273, 2017.

[45] Z. Li, W. Xia, H. Su, Z. Yu, Y. Fu, L. Chen, X. Wang, N. Yu, Z. Zou, and Y. Guo. Magnetic critical behavior of the van der Waals Fe5GeTe2 crystal with near room temperature ferromagnetism. *Scientific Reports*, 10(1):15345, 2020.

[46] E. Lifshitz and E. Ruderman. On the magnetic structure of iron. In L. P. PITAEVSKI, editor, *Soviet Physics Uspekhi*, volume 8, page 337. Pergamon, Amsterdam, 1944.

[47] M. D. Kuz'min, K. P. Skokov, L. V. B. Diop, I. A. Radulov, and O. Gutfleisch. Exchange stiffness of ferromagnets. *The European Physical Journal Plus*, 135(3):301, 2020.

[48] C. Kittel. On the theory of ferromagnetic resonance absorption. *Physical review*, 73(2):155–161, 1948.

[49] J. Kerr. XLIII. On rotation of the plane of polarization by reflection from the pole of a magnet. *The London, Edinburgh, and Dublin Philosophical Magazine and Journal of Science*, 3(19):321–343, 1877.

[50] E. Beaurepaire, J.-C. Merle, A. Daunois, and J.-Y. Bigot. Ultrafast Spin Dynamics in Ferromagnetic Nickel. *Phys. Rev. Lett.*, 76(22):4250–4253, may 1996.

[51] T. Sebastian, K. Schultheiss, B. Obry, B. Hillebrands, and H. Schultheiss. Micro-focused Brillouin light scattering: imaging spin waves at the nanoscale. *Frontiers in Physics*, 3, 2015.

[52] G. Schütz, W. Wagner, W. Wilhelm, P. Kienle, R. Zeller, R. Frahm, and G. Materlik. Absorption of circularly polarized x rays in iron. *Physical review letters*, 58(7):737, 1987.

[53] P. Fischer, T. Eimüller, G. Schütz, P. Guttmann, G. Schmahl, K. Pruegl, and G. Bayreuther. Imaging of magnetic domains by transmission x-ray microscopy. *Journal of Physics D: Applied Physics*, 31(6):649, mar 1998.

[54] M. Weigand, S. Wintz, J. Gräfe, M. Noske, H. Stoll, B. Van Waeyenberge, and G. Schütz. TimeMaxyne: A Shot-Noise Limited, Time-Resolved Pump-and-Probe Acquisition System Capable of 50 GHz Frequencies for Synchrotron-Based X-ray Microscopy. *Crystals*, 12(8), 2022.

[55] R. A. Gallardo, P. Alvarado-Seguel, T. Schneider, C. Gonzalez-Fuentes, A. Roldán-Molina, K. Lenz, J. Lindner, and P. Landeros. Spin-wave non-reciprocity in magnetization-graded ferromagnetic films. *New Journal of Physics*, 21(3):33026, mar 2019.

[56] S. Blundell. *Magnetism in condensed matter*. Oxford University Press, 2001.

[57] H. Kronmüller and S. S. P. Parkin. *Handbook of Magnetism and Advanced Magnetic Materials*. Springer Cham, 2007.

[58] M. Getzlaff. *Fundamentals of magnetism*. Springer Science & Business Media, 2007.

[59] B. A. Kalinikos and A. N. Slavin. Theory of dipole-exchange spin wave spectrum for ferromagnetic films with mixed exchange boundary conditions. *Journal of Physics C: Solid State Physics*, 19(35):7013, 1986.

[60] J. A. Osborn. Demagnetizing Factors of the General Ellipsoid. *Phys. Rev.*, 67(11-12):351–357, jun 1945.

[61] M. Sato and Y. Ishii. Simple and approximate expressions of demagnetizing factors of uniformly magnetized rectangular rod and cylinder. *Journal of Applied Physics*, 66(2):983–985, 1989.

[62] C. N. Yang and C. P. Yang. One-Dimensional Chain of Anisotropic Spin-Spin Interactions. I. Proof of Bethe's Hypothesis for Ground State in a Finite System. *Phys. Rev.*, 150(1):321–327, oct 1966.

[63] J. E. Hirsch. Spin Hall Effect. *Physical Review Letters*, 83(9):1834, 1999.

[64] T. Moriya. Anisotropic Superexchange Interaction and Weak Ferromagnetism. *Phys. Rev.*, 120(1):91–98, oct 1960.

[65] A. Thiaville, S. Rohart, É. Jué, V. Cros, and A. Fert. Dynamics of Dzyaloshinskii domain walls in ultrathin magnetic films. *Europhysics Letters*, 100(5):57002, dec 2012.

[66] U. K. Rößler, A. N. Bogdanov, and C. Pfleiderer. Spontaneous skyrmion ground states in magnetic metals. *Nature*, 442(7104):797–801, 2006.

[67] M. Ziese and M. J. Thornton. *Spin electronics*, volume 569. Springer Berlin, Heidelberg, 1 edition, 2007.

[68] T. Trunk, M. Redjdal, A. Kákay, M. F. Ruane, and F. B. Humphrey. Domain wall structure in Permalloy films with decreasing thickness at the Bloch to Néel transition. *Journal of Applied Physics*, 89(11):7606–7608, jun 2001.

[69] J. Mendil, M. Trassin, Q. Bu, J. Schaab, M. Baumgartner, C. Murer, P. T. Dao, J. Vijayakumar, D. Bracher, C. Bouillet, C. A. F. Vaz, M. Fiebig, and P. Gambardella. Magnetic properties and domain structure of ultrathin yttrium iron garnet/Pt bilayers. *Phys. Rev. Mater.*, 3(3):34403, mar 2019.

[70] M. A. W. Schoen, D. Thonig, M. L. Schneider, T. J. Silva, H. T. Nembach, O. Eriksson, O. Karis, and J. M. Shaw. Ultra-low magnetic damping of a metallic ferromagnet. *Nature Physics*, 12(9):839–842, 2016.

[71] M. A. W. Schoen, J. Lucassen, H. T. Nembach, B. Koopmans, T. J. Silva, C. H. Back, and J. M. Shaw. Magnetic properties in ultrathin 3 d transition-metal binary alloys. II. Experimental verification of quantitative theories of damping and spin pumping. *Physical Review B*, 95(13):134411, 2017.

[72] H. Chang, P. Li, W. Zhang, T. Liu, A. Hoffmann, L. Deng, and M. Wu. Nanometer-Thick Yttrium Iron Garnet Films With Extremely Low Damping. *IEEE Magnetics Letters*, 5:1–4, 2014.

[73] M. C. Hickey and J. S. Moodera. Origin of Intrinsic Gilbert Damping. *Phys. Rev. Lett.*, 102(13):137601, mar 2009.

[74] S. Zhang and Z. Li. Roles of Nonequilibrium Conduction Electrons on the Magnetization Dynamics of Ferromagnets. *Phys. Rev. Lett.*, 93(12):127204, sep 2004.

[75] M. Fähnle, R. Singer, D. Steiauf, and V. P. Antropov. Role of nonequilibrium conduction electrons on the magnetization dynamics of ferromagnets in the *s-d* model. *Phys. Rev. B*, 73(17):172408, may 2006.

[76] V. Kamberský. On the Landau–Lifshitz relaxation in ferromagnetic metals. *Canadian Journal of Physics*, 48(24):2906–2911, 1970.

[77] J. Kuneš and V. Kamberský. First-principles investigation of the damping of fast magnetization precession in ferromagnetic 3*d* metals. *Phys. Rev. B*, 65(21):212411, jun 2002.

[78] Y. Tserkovnyak, A. Brataas, G. E. W. Bauer, and B. I. Halperin. Nonlocal magnetization dynamics in ferromagnetic heterostructures. *Rev. Mod. Phys.*, 77(4):1375–1421, dec 2005.

[79] B. K. Kuanr, R. E. Camley, and Z. Celinski. Extrinsic contribution to Gilbert damping in sputtered NiFe films by ferromagnetic resonance. *Journal of Magnetism and Magnetic Materials*, 286:276–281, 2005.

[80] R. H. Silsbee, A. Janossy, and P. Monod. Coupling between ferromagnetic and conduction-spin-resonance modes at a ferromagnetic—normal-metal interface. *Physical Review B*, 19(9):4382, 1979.

[81] F. Groß, N. Träger, J. Förster, M. Weigand, G. Schütz, and J. Gräfe. Nanoscale detection of spin wave deflection angles in permalloy. *Applied Physics Letters*, 114(1):012406, 2019.

[82] H. Qin, S. J. Hämäläinen, K. Arjas, J. Witteveen, and S. van Dijken. Propagating spin waves in nanometer-thick yttrium iron garnet films:

Dependence on wave vector, magnetic field strength, and angle. *Phys. Rev. B*, 98(22):224422, dec 2018.

[83] A. A. Serga, A. V. Chumak, and B. Hillebrands. YIG magnonics. *Journal of Physics D: Applied Physics*, 43(26):264002, jun 2010.

[84] D. D. Stancil and A. Prabhakar. *Spin Waves: Theory and Applications*, volume 5. Springer, 2009.

[85] T. Brächer, P. Pirro, and B. Hillebrands. Parallel pumping for magnon spintronics: Amplification and manipulation of magnon spin currents on the micron-scale. *Physics Reports*, 699:1–34, 2017.

[86] T. Schneider, A. A. Serga, T. Neumann, B. Hillebrands, and M. P. Kostylev. Phase reciprocity of spin-wave excitation by a microstrip antenna. *Phys. Rev. B*, 77(21):214411, jun 2008.

[87] J. Yano and V. K. Yachandra. X-ray absorption spectroscopy. *Photosynthesis Research*, 102(2):241, 2009.

[88] CXRO X-Ray Database, Transmission of Solids. `https://henke.lbl.gov/optical_constants/filter2.html` (accessed 13.01.2023).

[89] B. L. Henke, E. M. Gullikson, and J. C. Davis. X-Ray Interactions: Photoabsorption, Scattering, Transmission, and Reflection at E = 50-30,000 eV, Z = 1-92. *Atomic Data and Nuclear Data Tables*, 54(2):181–342, 1993.

[90] M. Weigand. *Realization of a new magnetic scanning X-ray microscope and investigation of Landau structures under pulsed field excitation.* PhD thesis, Universität Stuttgart, 2015.

[91] S. Mobilio, F. Boscherini, and C. Meneghini. *Synchrotron Radiation.* Springer, 2014.

[92] D. Nolle, M. Weigand, G. Schütz, and E. Goering. High contrast magnetic and nonmagnetic sample current microscopy for bulk and transparent samples using soft x-rays. *Microscopy and Microanalysis*, 17(5):834–842, 2011.

[93] BESSY II Homepage. `https://www.helmholtz-berlin.de/forschung/quellen/bessy/index_en.html` (accessed 17.01.2023).

[94] MAXYMUS Homepage. `https://www.helmholtz-berlin.de/pubbin/igama_output?modus=einzel&sprache=en&gid=1885` (accessed 17.01.2023).

[95] P. Audehm. *Gepinnte Bahnmomente in magnetischen Heterostrukturen*. PhD thesis, Universität Stuttgart, 2016.

[96] I. Bykova. *High-resolution X-ray ptychography for magnetic imaging*. PhD thesis, Universität Stuttgart, 2018.

[97] J. Kirz. Phase zone plates for x rays and the extreme uv. *J. Opt. Soc. Am.*, 64(3):301–309, mar 1974.

[98] U. T. Sanli, C. Jiao, M. Baluktsian, C. Grévent, K. Hahn, Y. Wang, V. Srot, G. Richter, I. Bykova, M. Weigand, G. Schütz, and K. Keskinbora. 3D Nanofabrication of High-Resolution Multilayer Fresnel Zone Plates. *Advanced Science*, 5(9):1800346, 2018.

[99] W. Demtröder. *Experimentalphysik 3 - Atome, Moleküle und Festkörper*. Springer Spektrum Berlin Heidelberg, 2016.

[100] M. Noske. *Ultraschnelles Vortexkernschalten*. PhD thesis, Universität Stuttgart, 2016.

[101] F. Groß, N. Träger, F. Schulz, M. Weigand, T. Dippon, and J. Gräfe. A high frequency builder software for arbitrary radio frequency signals. *Review of Scientific Instruments*, 93(3):034704, 2022.

[102] A. J. P. Meyer and G. Asch. Experimental g' and g Values of Fe, Co, Ni, and Their Alloys. *Journal of Applied Physics*, 32(3):S330–S333, 1961.

[103] C. Kittel. On the gyromagnetic ratio and spectroscopic splitting factor of ferromagnetic substances. *Physical Review*, 76(6):743, 1949.

[104] G. Woltersdorf. *Spin-pumping and two-magnon scattering in magnetic multilayers*. PhD thesis, Simon Fraser University, 2004.

[105] W. Barry. A broad-band, automated, stripline technique for the simultaneous measurement of complex permittivity and permeability. *IEEE Transactions on Microwave Theory and Techniques*, 34(1):80–84, 1986.

[106] I. S. Maksymov and M. Kostylev. Broadband stripline ferromagnetic resonance spectroscopy of ferromagnetic films, multilayers and nanostructures. *Physica E: Low-dimensional Systems and Nanostructures*, 69:253–293, 2015.

[107] Z. Celinski and B. Heinrich. Ferromagnetic resonance linewidth of Fe ultrathin films grown on a bcc Cu substrate. *Journal of Applied Physics*, 70(10):5935–5937, 1991.

[108] R. L. Fagaly. Superconducting quantum interference device instruments and applications. *Review of Scientific Instruments*, 77(10):101101, 2006.

[109] W. Sucksmith and J. E. Thompson. The magnetic anisotropy of cobalt. *Proc. R. Soc. Lond. A*, 225(1162):362–375, 1954.

[110] P. J. Goodhew, J. Humphreys, and R. Beanland. *Electron Microscopy and Analysis*. Taylor & Francis, 1975.

[111] R. A. Carlton, C. E. Lyman, and J. E. Roberts. Accuracy and precision of quantitative energy-dispersive x-ray spectrometry in the

environmental scanning electron microscope. *Scanning: The Journal of Scanning Microscopies*, 26(4):167–174, 2004.

[112] E. Kuphal. Liquid phase epitaxy. *Applied Physics A*, 52(6):380–409, 1991.

[113] C. Dubs, O. Surzhenko, R. Linke, A. Danilewsky, U. Brückner, and J. Dellith. Sub-micrometer yttrium iron garnet LPE films with low ferromagnetic resonance losses. *Journal of Physics D: Applied Physics*, 50(20):204005, 2017.

[114] J. Förster, S. Wintz, J. Bailey, S. Finizio, E. Josten, C. Dubs, D. A. Bozhko, H. Stoll, G. Dieterle, N. Träger, J. Raabe, A. N. Slavin, M. Weigand, J. Gräfe, and G. Schütz. Nanoscale X-ray imaging of spin dynamics in yttrium iron garnet. *Journal of Applied Physics*, 126(17):173909, 2019.

[115] Q. Jiang, N. Kurra, and H. N. Alshareef. Marker Pen Lithography for Flexible and Curvilinear On-Chip Energy Storage. *Advanced Functional Materials*, 25(31):4976–4984, 2015.

[116] L. Lechner, J. Biskupek, and U. Kaiser. Improved Focused Ion Beam Target Preparation of (S)TEM Specimen—A Method for Obtaining Ultrathin Lamellae. *Microscopy and Microanalysis*, 18(2):379–384, 2012.

[117] E. Gao, S.-Z. Lin, Z. Qin, M. J. Buehler, X.-Q. Feng, and Z. Xu. Mechanical exfoliation of two-dimensional materials. *Journal of the Mechanics and Physics of Solids*, 115:248–262, 2018.

[118] M. Donahue and D. Porter. OOMMF User's Guide, Version 1.0. *NIST Interagency Report*, 1999.

[119] A. Vansteenkiste, J. Leliaert, M. Dvornik, M. Helsen, F. Garcia-Sanchez, and B. Van Waeyenberge. The design and verification of MuMax3. *AIP Advances*, 4(10):107133, 2014.

[120] A. V. Chumak, V. I. Vasyuchka, A. A. Serga, and B. Hillebrands. Magnon spintronics. *Nature Physics*, 11(6):453–461, 2015.

[121] J. Torrejon, M. Riou, F. A. Araujo, S. Tsunegi, G. Khalsa, D. Querlioz, P. Bortolotti, V. Cros, K. Yakushiji, A. Fukushima, and Others. Neuromorphic computing with nanoscale spintronic oscillators. *Nature*, 547(7664):428–431, 2017.

[122] Y. Au, M. Dvornik, T. Davison, E. Ahmad, P. S. Keatley, A. Vansteenkiste, B. Van Waeyenberge, and V. V. Kruglyak. Direct excitation of propagating spin waves by focused ultrashort optical pulses. *Physical review letters*, 110(9):097201, 2013.

[123] F. Groß, M. Zelent, N. Träger, J. Förster, U. T. Sanli, R. Sauter, M. Decker, C. H. Back, M. Weigand, K. Keskinbora, and Others. Building Blocks for Magnon Optics: Emission and Conversion of Short Spin Waves. *ACS nano*, 14(12):17184–17193, 2020.

[124] H. Głowiński, K. Załkeski, J. Sprada, and J. Dubowik. Exchange Coupled NiFe/NiMn Bilayer Studied by a Vector Network Analyzer Ferromagnetic Resonance. *Acta Physica Polonica, A.*, 121(5-6):1145–1147, 2012.

[125] F. Lisiecki, J. Rychły, P. Kuświk, H. Głowiński, J. W. Kłos, F. Groß, I. Bykova, M. Weigand, M. Zelent, E. J. Goering, and Others. Reprogrammability and scalability of magnonic fibonacci quasicrystals. *Physical Review Applied*, 11(5):54003, 2019.

[126] B. A. Julies, D. Knoesen, R. Pretorius, and D. Adams. A study of the NiSi to NiSi2 transition in the Ni–Si binary system. *Thin Solid Films*, 347(1):201–207, 1999.

[127] S. S. Cohen, P. A. Piacente, G. Gildenblat, and D. M. Brown. Platinum silicide ohmic contacts to shallow junctions in silicon. *Journal of Applied Physics*, 53(12):8856–8862, 1982.

[128] M. A. W. Schoen, J. Lucassen, H. T. Nembach, T. J. Silva, B. Koopmans, C. H. Back, and J. M. Shaw. Magnetic properties of ultrathin 3 d transition-metal binary alloys. I. Spin and orbital moments, anisotropy, and confirmation of Slater-Pauling behavior. *Physical Review B*, 95(13):134410, 2017.

[129] F. Schulz, R. Lawitzki, H. Głowiński, F. Lisiecki, N. Träger, P. Kuświk, E. Goering, G. Schütz, and J. Gräfe. Increase of Gilbert damping in Permalloy thin films due to heat-induced structural changes. *Journal of Applied Physics*, 129(15):153903, 2021.

[130] R. D. McMichael, M. D. Stiles, P. J. Chen, and W. F. Egelhoff. Ferromagnetic resonance linewidth in thin films coupled to NiO. *Journal of Applied Physics*, 83(11):7037–7039, 1998.

[131] R. Arias and D. L. Mills. Extrinsic contributions to the ferromagnetic resonance response of ultrathin films. *Physical review B*, 60(10):7395, 1999.

[132] D. J. Twisselmann and R. D. McMichael. Intrinsic damping and intentional ferromagnetic resonance broadening in thin Permalloy films. *Journal of applied physics*, 93(10):6903–6905, 2003.

[133] R. D. McMichael and P. Krivosik. Classical Model of Extrinsic Ferromagnetic Resonance Linewidth in Ultrathin Films. *IEEE Transactions on Magnetics*, 40(1 I):2–11, 2004.

[134] A. Dahal, J. Gunasekera, L. Harringer, D. K. Singh, and D. J. Singh. Metallic nickel silicides: Experiments and theory for NiSi and first principles calculations for other phases. *Journal of Alloys and Compounds*, 672:110–116, 2016.

[135] C.-H.-T. Chang, P.-C. Jiang, Y.-T. Chow, H.-L. Hsiao, W.-B. Su, and J.-S. Tsay. Enhancing silicide formation in Ni/Si(111) by Ag-Si particles at the interface. *Scientific Reports*, 9(1):8835, 2019.

[136] R. D. McMichael, D. J. Twisselmann, and A. Kunz. Localized ferromagnetic resonance in inhomogeneous thin films. *Physical review letters*, 90(22):227601, 2003.

[137] F. Rosenblatt. The perceptron: A probabilistic model for information storage and organization in the brain. *Psychological Review*, 65(6):386–408, 1958.

[138] K. Berggren, Q. Xia, K. K. Likharev, D. B. Strukov, H. Jiang, T. Mikolajick, D. Querlioz, M. Salinga, J. R. Erickson, S. Pi, and Others. Roadmap on emerging hardware and technology for machine learning. *Nanotechnology*, 32(1):12002, 2020.

[139] M. Hu, Y. Chen, J. J. Yang, Y. Wang, and H. H. Li. A compact memristor-based dynamic synapse for spiking neural networks. *IEEE Transactions on Computer-Aided Design of Integrated Circuits and Systems*, 36(8):1353–1366, 2016.

[140] Q. Wan, M. T. Sharbati, J. R. Erickson, Y. Du, and F. Xiong. Emerging artificial synaptic devices for neuromorphic computing. *Advanced Materials Technologies*, 4(4):1900037, 2019.

[141] H. P. Graf. Analog electronic neural networks. *European Solid-State Circuits Conference*, 1992-Septe:57–60, 1992.

[142] I. B. Pyne. Linear programming on an electronic analogue computer. *Transactions of the American Institute of Electrical Engineers, Part I: Communication and Electronics*, 75(2):139–143, 1956.

[143] S. Zuo, Q. Wei, Y. Tian, Y. Cheng, and X. Liu. Acoustic analog computing system based on labyrinthine metasurfaces. *Scientific Reports*, 8(1):10103, 2018.

[144] D. R. Solli and B. Jalali. Analog optical computing. *Nature Photonics*, 9(11):704–706, 2015.

[145] Á. Papp, W. Porod, and G. Csaba. Nanoscale neural network using non-linear spin-wave interference. *Nature communications*, 12(1):1–8, 2021.

[146] A. Chumak, P. Kabos, M. Wu, C. Abert, C. Adelmann, A. Adeyeye, J. Åkerman, F. Aliev, A. Anane, A. Awad, and Others. Advances in Magnetics Roadmap on Spin-Wave Computing. *IEEE Transactions on Magnetics*, 58(6):1–72, 2022.

[147] J. Chen, H. Wang, T. Hula, C. Liu, S. Liu, T. Liu, H. Jia, Q. Song, C. Guo, Y. Zhang, J. Zhang, X. Han, D. Yu, M. Wu, H. Schultheiss, and H. Yu. Reconfigurable Spin-Wave Interferometer at the Nanoscale. *Nano Letters*, 21(14):6237–6244, 2021.

[148] T. Brächer and P. Pirro. An analog magnon adder for all-magnonic neurons. *Journal of Applied Physics*, 124(15):152119, 2018.

[149] F. Schulz, F. Groß, J. Förster, S. Mayr, M. Weigand, E. Goering, J. Gräfe, G. Schütz, and S. Wintz. Realization of a magnonic analog adder with frequency-division multiplexing. *AIP Advances*, 13(1):15115, 2023.

[150] H. B. Vasili, B. Casals, R. Cichelero, F. Macià, J. Geshev, P. Gargiani, M. Valvidares, J. Herrero-Martin, E. Pellegrin, J. Fontcuberta, and G. Herranz. Direct observation of multivalent states and $4f \rightarrow 3d$ charge transfer in Ce-doped yttrium iron garnet thin films. *Phys. Rev. B*, 96(1):14433, jul 2017.

[151] S. Weinstein and P. Ebert. Data Transmission by Frequency-Division Multiplexing Using the Discrete Fourier Transform. *IEEE Transactions on Communication Technology*, 19(5):628–634, 1971.

[152] N. Träger, P. Gruszecki, F. Lisiecki, J. Förster, M. Weigand, S. Wintz, H. Stoll, H. Głowiński, P. Kuświk, M. Krawczyk, and J. Gräfe. Direct Imaging of High-Frequency Multimode Spin Wave Propagation in

Cobalt-Iron Waveguides Using X-Ray Microscopy beyond 10 GHz. *physica status solidi (RRL) – Rapid Research Letters*, 14(12):2000373, 2020.

[153] J. M. Kosterlitz and D. J. Thouless. Ordering, metastability and phase transitions in two-dimensional systems. *Journal of Physics C: Solid State Physics*, 6(7):1181, apr 1973.

[154] A. K. Geim. Graphene: Status and Prospects. *Science*, 324(5934):1530–1534, 2009.

[155] G. G. Naumis, S. Barraza-Lopez, M. Oliva-Leyva, and H. Terrones. Electronic and optical properties of strained graphene and other strained 2D materials: A review. *Reports on Progress in Physics*, 80(9), 2017.

[156] F. Schwierz. Graphene transistors. *Nature Nanotechnology*, 5(7):487–496, 2010.

[157] P. Avouris and F. Xia. Graphene applications in electronics and photonics. *MRS Bulletin*, 37(12):1225–1234, 2012.

[158] C. Chung, Y.-K. Kim, D. Shin, S.-R. Ryoo, B. H. Hong, and D.-H. Min. Biomedical Applications of Graphene and Graphene Oxide. *Accounts of Chemical Research*, 46(10):2211–2224, oct 2013.

[159] A. L. Coughlin, D. Xie, Y. Yao, X. Zhan, Q. Chen, H. Hewa-Walpitage, X. Zhang, H. Guo, H. Zhou, J. Lou, J. Wang, Y. S. Li, H. A. Fertig, and S. Zhang. Near Degeneracy of Magnetic Phases in Two-Dimensional Chromium Telluride with Enhanced Perpendicular Magnetic Anisotropy. *ACS Nano*, 14(11):15256–15266, nov 2020.

[160] Y. Wen, Z. Liu, Y. Zhang, C. Xia, B. Zhai, X. Zhang, G. Zhai, C. Shen, P. He, R. Cheng, L. Yin, Y. Yao, M. Getaye Sendeku, Z. Wang, X. Ye, C. Liu, C. Jiang, C. Shan, Y. Long, and J. He.

Tunable Room-Temperature Ferromagnetism in Two-Dimensional Cr2Te3. *Nano Letters*, 20(5):3130–3139, 2020.

[161] N. León-Brito, E. D. Bauer, F. Ronning, J. D. Thompson, and R. Movshovich. Magnetic microstructure and magnetic properties of uniaxial itinerant ferromagnet Fe3GeTe2. *Journal of Applied Physics*, 120(8):83903, 2016.

[162] A. F. May, D. Ovchinnikov, Q. Zheng, R. Hermann, S. Calder, B. Huang, Z. Fei, Y. Liu, X. Xu, and M. A. McGuire. Ferromagnetism Near Room Temperature in the Cleavable van der Waals Crystal Fe5GeTe2. *ACS Nano*, 13(4):4436–4442, 2019.

[163] Z. Li, W. Xia, H. Su, Z. Yu, Y. Fu, L. Chen, X. Wang, N. Yu, Z. Zou, and Y. Guo. Magnetic critical behavior of the van der Waals Fe5GeTe2 crystal with near room temperature ferromagnetism. *Scientific Reports*, 10(1):1–10, 2020.

[164] L. Alahmed, B. Nepal, J. Macy, W. Zheng, B. Casas, A. Sapkota, N. Jones, A. R. Mazza, M. Brahlek, W. Jin, M. Mahjouri-Samani, S. S. Zhang, C. Mewes, L. Balicas, T. Mewes, and P. Li. Magnetism and spin dynamics in room-temperature van der Waals magnet Fe5GeTe2. *2D Materials*, 8(4):1–18, 2021.

[165] W. He, L. Kong, W. Zhao, and P. Yu. Atomically Thin 2D van der Waals Magnetic Materials: Fabrications, Structure, Magnetic Properties and Applications. *Coatings*, 12(2), 2022.

[166] J. W. Cable, M. K. Wilkinson, and E. O. Wollan. Neutron diffraction investigation of antiferromagnetism in CrCl3. *Journal of Physics and Chemistry of Solids*, 19(1):29–34, 1961.

[167] Z. Wang, M. Gibertini, D. Dumcenco, T. Taniguchi, K. Watanabe, E. Giannini, and A. F. Morpurgo. Determining the phase diagram of

atomically thin layered antiferromagnet CrCl3. *Nature Nanotechnology*, 14(12):1116–1122, 2019.

[168] C. Gong, L. Li, Z. Li, H. Ji, A. Stern, Y. Xia, T. Cao, W. Bao, C. Wang, Y. Wang, Z. Q. Qiu, R. J. Cava, S. G. Louie, J. Xia, and X. Zhang. Discovery of intrinsic ferromagnetism in two-dimensional van der Waals crystals. *Nature*, 546(7657):265–269, 2017.

[169] V Carteaux, D Brunet, G Ouvrard, and G Andre. Crystallographic, magnetic and electronic structures of a new layered ferromagnetic compound Cr2Ge2Te6. *Journal of Physics: Condensed Matter*, 7(1):69, 1995.

[170] M. Lohmann, T. Su, B. Niu, Y. Hou, M. Alghamdi, M. Aldosary, W. Xing, J. Zhong, S. Jia, W. Han, R. Wu, Y.-T. Cui, and J. Shi. Probing Magnetism in Insulating Cr2Ge2Te6 by Induced Anomalous Hall Effect in Pt. *Nano Letters*, 19(4):2397–2403, apr 2019.

[171] B. Huang, G. Clark, E. Navarro-Moratalla, D. R. Klein, R. Cheng, K. L. Seyler, D. Zhong, E. Schmidgall, M. A. McGuire, D. H. Cobden, W. Yao, D. Xiao, P. Jarillo-Herrero, and X. Xu. Layer-dependent ferromagnetism in a van der Waals crystal down to the monolayer limit. *Nature*, 546(7657):270–273, 2017.

[172] Z. Zhang, J. Shang, C. Jiang, A. Rasmita, W. Gao, and T. Yu. Direct Photoluminescence Probing of Ferromagnetism in Monolayer Two-Dimensional CrBr3. *Nano Letters*, 19(5):3138–3142, may 2019.

[173] W. Chen, Z. Sun, Z. Wang, L. Gu, X. Xu, S. Wu, and C. Gao. Direct observation of van der Waals stacking-dependent interlayer magnetism. *Science*, 366(6468):983–987, 2019.

[174] L. Meng, Z. Zhou, M. Xu, S. Yang, K. Si, L. Liu, X. Wang, H. Jiang, B. Li, P. Qin, P. Zhang, J. Wang, Z. Liu, P. Tang, Y. Ye, W. Zhou, L. Bao, H.-J. Gao, and Y. Gong. Anomalous thickness dependence

of Curie temperature in air-stable two-dimensional ferromagnetic 1T-CrTe2 grown by chemical vapor deposition. *Nature Communications*, 12(1):809, 2021.

[175] X. Zhang, Q. Lu, W. Liu, W. Niu, J. Sun, J. Cook, M. Vaninger, P. F. Miceli, D. J. Singh, S.-W. Lian, T.-R. Chang, X. He, J. Du, L. He, R. Zhang, G. Bian, and Y. Xu. Room-temperature intrinsic ferromagnetism in epitaxial CrTe2 ultrathin films. *Nature Communications*, 12(1):2492, 2021.

[176] C. Tan, J. Lee, S.-G. Jung, T. Park, S. Albarakati, J. Partridge, M. R. Field, D. G. McCulloch, L. Wang, and C. Lee. Hard magnetic properties in nanoflake van der Waals Fe3GeTe2. *Nature Communications*, 9(1):1554, 2018.

[177] Z. Fei, B. Huang, P. Malinowski, W. Wang, T. Song, J. Sanchez, W. Yao, D. Xiao, X. Zhu, A. F. May, W. Wu, D. H. Cobden, J.-H. Chu, and X. Xu. Two-dimensional itinerant ferromagnetism in atomically thin Fe3GeTe2. *Nature Materials*, 17(9):778–782, 2018.

[178] J. Cenker, B. Huang, N. Suri, P. Thijssen, A. Miller, T. Song, T. Taniguchi, K. Watanabe, M. A. McGuire, D. Xiao, and X. Xu. Direct observation of two-dimensional magnons in atomically thin CrI3. *Nature Physics*, 17(1):20–25, 2021.

[179] L. N. Kapoor, S. Mandal, P. C. Adak, M. Patankar, S. Manni, A. Thamizhavel, and M. M. Deshmukh. Observation of Standing Spin Waves in a van der Waals Magnetic Material. *Advanced Materials*, 33(2):2005105, 2021.

[180] A. F. May, M. H. Du, V. R. Cooper, and M. A. McGuire. Tuning magnetic order in the van der Waals metal Fe5GeTe2 by cobalt substitution. *Physical Review Materials*, 4(7):1–9, 2020.

[181] X. Hu, D.-X. Yao, and K. Cao. $(Fe_{1-x}Ni_x)_5GeTe_2$: An antiferromagnetic triangular Ising lattice with itinerant magnetism. *Phys. Rev. B*, 106(22):224423, dec 2022.

[182] N. Träger, F. Groß, J. Förster, K. Baumgaertl, H. Stoll, M. Weigand, G. Schütz, D. Grundler, and J. Gräfe. Single shot acquisition of spatially resolved spin wave dispersion relations using X-ray microscopy. *Scientific Reports*, 10(1):18146, 2020.

[183] I. K. Park, C. Gong, K. Kim, and G. Lee. Controlling interlayer magnetic coupling in the two-dimensional magnet Fe3GeTe2. *Physical Review B*, 105(1):1–8, 2022.

List of Publications

- **F. Schulz**, R. Lawitzki, H. Głowiński, F. Lisiecki, N. Träger, P. Kuświk, E. Goering, G. Schütz and J. Gräfe. Increase of Gilbert damping in Permalloy thin films due to heat-induced structural changes. *Journal of Applied Physics*, **129**, 153903 (2021).

- **F. Schulz**, F. Groß, J. Förster, S. Mayr, M. Weigand, E. Goering, J. Gräfe, G. Schütz and S. Wintz. Realization of a Magnonic Analog Adder with Frequency-Division Multiplexing. *AIP Advances*, **13**, 01511 (2023).

- **F. Schulz**, K. Litzius, L. Powalla, M. Birch, S. Satheesh, M. Weigand, K. Kern, G. Schütz, M. Burghard and S. Wintz. Direct Observation of Propagating Spin Waves in the 2D van-der-Waals Ferromagnet Fe_5GeTe_2. In preparation.

- M. Birch, D. Cortés-Ortuño, K. Litzius, S. Wintz, **F. Schulz**, M. Weigand, A. Štefančič, D. Mayoh, G. Balakrishnan, P. Hatton and G. Schütz. Toggle-like current-induced Bloch point dynamics of 3D skyrmion strings in a room-temperature nanowire. *Nature Communications* **13**, 3630 (2022)

- F. Groß, N. Träger, **F. Schulz**, M. Weigand, T. Dippon and J. Gräfe. A high frequency builder software for arbitrary radio frequency signals. *Review of Scientific Instruments* **93**, 034704 (2022).

- L. Powalla, M. Birch, K. Litzius, S. Wintz, **F. Schulz**, M. Weigand, T. Scholz, B.V. Lotsch, K. Kern, G. Schütz and M. Burghard. Single Skyrmion Generation via a Vertical Nanocontact in a 2D Magnet-Based Heterostructure. *Nano Letters*, **22**, 23, 9236-9243 (2022).

- L. Powalla, M.T. Birch, K. Litzius, S. Wintz, F.S. Yasin, L.A. Turnbull, **F. Schulz**, D.A. Mayoh, G. Balakrishnan, M. Weigand, X.Yu, K. Kern, G. Schütz, M. Burghard. Seeding and emergence of composite skyrmions in a van der Waals magnet. *Advanced Materials*, 2208930 (2023).

Acknowledgments

Finally, I would like to express my gratitude to the many people who have contributed in various different ways to this thesis or who have otherwise supported me over the course of my doctoral studies. In particular, I want to thank:

- Gisela Schütz for giving me the opportunity to do a PhD in her department and for her continued commitment and support.

- Peter Michler and Christian Holm for assuming the responsibility of second examiner and chairing my thesis defense.

- Sebastian Wintz for his extensive support and mentorship while planning the various projects, for numerous scientific and non-scientific discussions, and of course for his company during long night shifts in Berlin.

- Felix Groß and Sven Erik Ilse for their invaluable companionship in 4E4, including countless exciting discussions and diversions and for shaping the time of my PhD studies in various wonderful ways.

- Eberhard Goering for his infectious enthusiasm, which has also inspired me to start my PhD.

- Joachim Gräfe for the scientific guidance and impulses that have helped me finding my way during my doctoral studies.

- Johan Åkerman for giving me the opportunity to work in his department in Göteborg for a month, and his group for making this time so instructive and enjoyable.

- Johannes Förster and Sina Mayr for support during beamtime.

- Max Birch, Lukas Powalla, Sayooj Satheesh and Kai Litzius for their tireless work and the exciting collaboration on the Fe_5GeTe_2 project. Special thanks to Max for providing me with the static FGT data and helping with their interpretation.

- Rodolfo Gallardo for his help with the magnetic multilayer model over several insightful online meetings.

- Giacomo Talmelli for his advice on the design and fabrication of the $Ni_{80}Fe_{20}$ adder device.

- Michael Bechtel, Markus Weigand and Hermann Stoll for their support and expertise at the MAXYMUS beamline.

- Bernd Ludescher for the many samples he prepared for me, oftentimes on very short notice, and his invaluable advice.

- Thomas Meisner for preparing and thinning the YIG samples.

- Ulrike Eigenthaler for ion milling the YIG windows, and preparing TEM lamella of the $Ni_{80}Fe_{20}$ samples.

- Bettina Lotsch and Tanja Scholz for synthesizing the Fe_5GeTe_2 crystals.

- Thomas Reindl, Ulrike Waizmann, Marion Hagel and Bernhard Fenk for their extensive support in the clean room.

- Barbara Baum and Annette Zechmeister for cutting the YIG and $Ni_{80}Fe_{20}$ samples.

- Monika Kotz for taking care of administrative and personal concerns with unmatched kindness.

- The entire department Schütz, including former colleagues, for making this such a pleasant place to work.

- My friends, who have filled my life with joy and excitement, even in times of stress and doubt.

- My brother Bernd and my parents Gerlinde and Wolfgang for their unconditional love and support and for making me feel that I could always rely on them.

- Nora for being the best companion I could have ever asked for. I'm excited to see what our future holds.